

UC Irvine

UC Irvine Electronic Theses and Dissertations

Title

Single Molecule Studies with Scanning Tunneling Microscopy and Tip-Enhanced Raman Spectroscopy

Permalink

<https://escholarship.org/uc/item/8qc5q8dq>

Author

Tallarida, Nicholas Ryan

Publication Date

2017

Copyright Information

This work is made available under the terms of a Creative Commons Attribution-NonCommercial-NoDerivatives License, available at <https://creativecommons.org/licenses/by-nc-nd/4.0/>

Peer reviewed|Thesis/dissertation

UNIVERSITY OF CALIFORNIA, IRVINE

Single Molecule Studies with Scanning Tunneling Microscopy
and Tip-Enhanced Raman Spectroscopy

DISSERTATION

submitted in partial satisfaction of the requirements for the degree of

DOCTOR OF PHILOSOPHY

in Chemistry and Material Physics

by

Nicholas Tallarida

Dissertation Committee:

Professor V.A. Apkarian, Chair

Professor Nien-Hui Ge

Professor Eric Potma

2017

Portions of Chapter 1 © 2014 ACS Publications

Portions of Chapter 2 © 2015 ACS Publications

All other materials © Nicholas Tallarida

Contents

List of Figures	vii
List of Tables	viii
Acknowledgments	ix
Curriculum Vitae	x
Abstract of the Thesis	xi
Introduction	1
1 Single Electron Switch	7
1.1 Experiment and Discussion	7
1.2 Analysis and Correction of the Switching Traces	13
1.2.1 Laplace Transform	13
1.2.2 Implementation: On-Level Determination	18
1.2.3 On-Time Correction	19
2 Observing the Isomerization of a Single Molecule with TERS	21
2.1 Introduction	21
2.2 Experimental	23
2.2.1 Chemisorption Structure	24

2.2.2	The Failure of ABT to Photoisomerize	26
2.2.3	TERRS detection	27
2.2.4	Meandering trajectories	29
2.2.5	Isomerization of a single molecule	31
2.2.6	Assignment	34
2.2.7	PCA of TERS spectra	36
2.2.8	Heterogeneous chemistry	39
2.3	Conclusion	41
3	Fabrication and Demonstration of Silver Tips with Sub-nanometer Spatially-Resolved TERS	43
3.1	Introduction	43
3.2	Experimental and Results	44
3.3	Conclusion	54
4	Tip-enhanced Raman spectromicroscopy: cavity photons, electrons and a molecule	56
4.1	Introduction	56
4.2	Methods	58
4.3	TERS of BPE trapped at the STM junction	59
4.3.1	Nanocavity Resonances	60
4.4	Imaging stationary CoTPP molecules	61
4.5	Overtones and combination bands	62
4.6	Conclusion	64
5	Sub-molecular Spatially-Resolved TERS of CoTPP at High and Low Temperature	65
5.1	Introduction	65
5.2	Experimental	68

5.3	TER-sm	69
5.4	Conclusions	77
6	Imaging Potential Surfaces with 3-Å Resolution via Molecular-Probe Tip-Enhanced Raman Spectroscopy	79
6.1	Introduction	79
6.2	Methods	80
6.3	TERS spectrum of CO-Tip	82
6.4	Imaging Potential Surfaces	86
6.5	Conclusion	90
A	System Improvements	101
A.1	Parabolic Mirror Alignment	101
A.1.1	Ray Tracing Simulation	102
A.1.2	Impact of the source	104
A.1.3	Parabolic Alignment Tool	105
A.2	Load-Lock System	106
A.2.1	Pumping Station and Tip Preparation	110

List of Figures

1.1	Schematic of Single Electron Conductance Switch	8
1.2	Conductance Switching Analysis	10
1.3	STM Topography and Functional Images of the Single Electron Switch . . .	11
1.4	Residence-Time Error due to Step Pulse	16
1.5	Example Fitted Correction for a Short Conductance Switch	17
1.6	Uncertainty in On-Level for Up-Switches	18
1.7	Two-Level System Directly Observed at Low Sample Biases	19
2.1	TERS experimental setup	24
2.2	Self-assembled ABT layer and associated electronic and optical spectroscopic data.	26
2.3	Meandering Raman trajectories	30
2.4	Flip-flop of a single molecule	33
2.5	Two Anticorrelated Spectra	35
2.6	Applying PCA to Single Molecule Spectra	37
2.7	PC2 Analysis	38
2.8	PCA tracks the molecular state in large datasets	39
2.9	Waterfall plot of normalized Raman spectra and associated timeline of flip-flop	40
3.1	Simulated ion trajectory around sharp tip	45
3.2	Simulated ion trajectory around sharp tip	47

3.3	Setup for batch processing of tips	48
3.4	Effect of FDSS on silver tips	49
3.5	Raman spectra of processed Ag tips	50
3.6	TERS spectra of BPE and CO and their gap dependence	52
3.7	TERS mapping of CoTPP monolayer	53
4.1	TERS over BPE trapped in Junction	59
4.2	Spectra of Nanocavity Resonances and Molecules	60
4.3	TERS Map of Au(111) surface coated with CoTPP and BPE	61
4.4	Cavity-enhanced overtones and combination bands	62
5.1	Render of TERS imaging of a CoTPP monolayer on Au(111)	67
5.2	FDSS produces effective TERS antenna	70
5.3	CO Acts as a Cavity Spoiler	72
5.4	Submolecular Chemical Information Revealed by TER-sm	74
5.5	TERS by Picking up CoTPP at 5 K	76
6.1	Illustration of CO Stark Shift Mapping	81
6.2	Gap and Bias dependence of CO stretch frequency	84
6.3	Spatially dependent frequency shift	86
6.4	CO Stark Shift Mapping of CoTPP	87
6.5	CO Stark Shift Mapping of ZnEtio	88
6.6	CO Stark Shift Map of Ag adatom	89
A.1	Excitation Geometries	101
A.2	Sample Zemax Component Editor	103
A.3	Zemax Model of Parabolic Detection Line	103
A.4	Parabolic Mirror Image Dependence on Source Position in z	104
A.5	Parabolic Mirror Image Dependence on Source Size	105

A.6	Parabolic Mirror Image for Confocal Geometry	106
A.7	Parabolic Alignment Tool	107
A.8	Schematic of the Tip/Sample and Doser Loadlocks	108
A.9	Schematic of Pumping and Ion Sputtering Station	110

List of Tables

1.1	Summary of Switching Rate Analysis	10
6.1	Summary of Bias ramps on various structures	85

Acknowledgments

I would like to express my deepest appreciation to my advisor, Professor Ara Apkarian, who has provided me with the opportunity, guidance, and support to develop as a scientist. I would like to thank my committee members, Professor Nien-Hue Ge and Professor Eric Potma for their advice and support throughout my graduate career. Furthermore, I'd like to thank Dr. Joonhee Lee for his tireless support, unparalleled patience, and invaluable expertise, without whom this research would not have been possible. I'd also like to thank the rest of the Apkarian Lab, especially Laura Ríos, for their help and understanding.

I also thank ACS Publications for permission to include parts of Chapter 1 and 2 of my dissertation, which was originally published in the ACS Nano and Nano Letters.

Very generous financial support was provided by the Center for Chemistry at the Space-Time Limit funded through NSF (CHE-0802913). Such experiments are not possible without such patient and generous patrons.

Lastly, I'd like to thank my family for their unwavering love and support.

Some text in this dissertation is a reprint of the material as it appears in ACS Nano[1] and Nano Letters[2]. The co-authors listed in these publications directed, supervised, and/or aided the research which formed the basis of this dissertation. Furthermore, with the intention of publishing in an academic journal in the next year, chapters 3-6 contain sections of manuscripts produced with the help of Prof. Apkarian and Dr. Joonhee Lee.

Curriculum Vitae

Highlights

Extensive background in experimental research, instrument design, fabrication, control, operation, and maintenance, Scanning Tunneling Microscopy, Surface Science, Vacuum Science, Optics, Imaging, Physical Chemistry, NIR/Visible ultrafast pulsed and visible diode laser technologies, and Optical Spectroscopy.

Education

PhD (2017): Chemistry and Material Physics, University of California Irvine (UCI)

MS (2016): Chemistry and Material Physics, University of California Irvine (UCI)

BS (2011): Chemistry, University of Notre Dame

Publications

Hovering and Twirling of Tethered Molecules by Confinement between Surfaces. Laura Rios, Joonhee Lee, Nicholas Tallarida, V. Ara Apkarian. *J. Phys. Chem. Lett.*, **2016**, *7*, 2461-2464.

Isomerization of one molecule observed through tip-enhanced Raman spectroscopy: Azobenzene thiol on Au(111). Nicholas Tallarida, Laura Rios, V. Ara Apkarian, Joonhee Lee. *Nano Lett.*, **2015**, *15*, 6386-6394.

Intrinsically Conductive OrganoSilver Linear Chain Polymers [-S-Ag-S-Biphenyl]_n Assembled on Roughened Elemental Silver. Stephen S. Sasaki, Yan-Ning Zhang, Shirshendu Dey, Nicholas Tallarida, Patrick Z. El-Khoury, V. A. Apkarian, Ruqian Wu. *J. Phys. Chem. C*, **2014**, *118*, 29287-29293

Single Electron Bipolar Conductance Switch Driven by the Molecular Aharonov-Bohm Effect. Joonhee Lee, Nicholas Tallarida, Laura Rios, Shawn M. Perdue, V. Ara Apkarian. *ACS Nano*, **2014**, *8*, 6382-6389

Automated electrochemical etching and polishing of silver scanning tunneling microscope tips Stephen S. Sasaki, Shawn M. Perdue, Alejandro Rodriguez Perez, Nicholas Tallarida, Julia H. Majors, V. Ara Apkarian, and Joonhee Lee. *Rev. Sci. Instrum.*, **2013**, *84*, 096109.

Abstract of the Dissertation

Single Molecule Studies with Scanning Tunneling Microscopy and Tip-Enhanced Raman Scattering

By Nicholas Tallarida

Doctor of Philosophy in Chemistry and Material Physics

University of California, Irvine, 2017

Professor V.A. Apkarian, Chair

Experimental techniques with the sensitivity to measure properties of individual molecules present an opportunity to investigate and understand fundamental chemical and physical processes. One such technique, scanning tunneling microscopy (STM), has proven itself to be the best tool for probing the properties of single molecules, enabling researchers to measure a molecule's electronic and vibrational properties with angstrom-level precision. Combining STM with optical vibrational spectroscopy allows the technique to measure molecular properties, bonding dynamics, optical phenomena, and light-matter interactions that are invisible to bare STM. Developing and perfecting the coupling of lasers with the STM tunneling junction can lead to time-resolving the technique, enabling sub-molecular topographic imaging with femtosecond time resolution. In this work, I detail the results of single molecule investigations with STM. In particular, I highlight the progress I have made in improving ultra-high vacuum STM by combining it with tip-enhanced Raman spectroscopy (TERS). The improvements made to TERS-STM focus on a variety experimental considerations in-

cluding optimizing laser-tip beam alignment through ray-tracing simulations and drastically improving the performance and reliability of TERS tips through the introduction of new tip manufacturing and preparation techniques. The efficacy of these improvements are demonstrated by the many high-resolution STM measurements including (1) the discovery and characterization of a single-electron switch involving the spin flip of an unpaired electron in a single molecule, (2) the observation via TERS-STM of one molecule undergoing a single reaction as well as an analysis of intensity and spectral fluctuations common to TERS, and (3) the demonstration and analysis of angstrom-resolved TERS-STM and its significance to our understanding of single-molecule physics and the tip-enhanced Raman effect.

Introduction

For the past several decades, there has been a concerted push to miniaturize technologies. This trend is exemplified by industry's adherence to "Moore's Law" [3], or the doubling of a computer chip's transistor density every 2 years, for the past 50 years. The transistor density cannot be increased at such a rate without simultaneously shrinking its size. This has driven electronics from the macroscale ($> 1 \mu\text{m}$) to the nanoscale, with transistor gate lengths now reaching down below 10 nm. In order to continue this miniaturization, new technologies need to be developed. At these length scales, quantum effects, like that of electron tunneling, start becoming relevant. A fundamental rethinking of the design of such circuit elements will become required. Furthermore, tools capable of characterizing the nanoscale are becoming more important than ever.

The field of molecular electronics is working on this redesign of electrical circuits [4]. As opposed to building circuit elements in the conventional way, the properties of individual molecules are studied and exploited to create circuit elements only ~ 1 nm in size. This has spurred research into a variety of molecular components including single molecule transistors [5], rectifiers [6], and switches [7–9].

Given that changing the conductance through a circuit element is often its main purpose, controlling conductance at the nanoscale is highly desirable. Schirm et al. demonstrated a reliable and robust two-terminal atomic conductivity switch. The observed hysteretic behavior provides the ability to use the system as a single-atom memory element [10]. Kumagai et al. explored the intramolecular hydrogen transfer in a porphycene molecule, observing that this

tautomerization reaction is strongly dependent on the molecule's local environment[11]. The ultimate limit in miniaturization of electronics can be regarded as that of a single functional electron, as opposed to a molecule or atom. Moreover, to maximize utility of nanoscopic devices by very-large-scale integration, it is important to minimize the generation of heat due to various dissipation channels that may be associated with the operation of the circuit element[12]. The single-electron conductivity switch, discussed in Chapter 1, meets these requirements. It relies on the spin-flip of one electron in one molecule, with energy spacing between spin-vibronic states of 1 meV.

As technologies move towards the molecular scale, the sensitivity and spatial resolution of characterization techniques must follow. While many are used to explore nanoscale systems. One of the more widely used is electron microscopes, like the scanning electron microscopy (SEM) and transmission electron microscopy (TEM)[13]. While these tools offer a relatively easy to use method of characterizing samples with resolutions down below 1 nm, they typically require high-energy electrons that can easily damage single molecules. On the other hand, scanning probe microscopies, like atomic force microscopy (AFM) and scanning tunneling microscopy (STM) offer Å-resolution without the fear of damaging the sample. Furthermore, they have proved to be quite versatile, being used to nanoscale systems at a very wide range of temperatures and pressures, including in liquids[14, 15]. In this work, the STM is used because of its ability to probe the electronic structure of the small molecules and their conductive substrate.

In STM[16], an atomically sharp metallic probe or tip is brought 4 to 7 Å ($1 \text{ \AA} = 0.1 \text{ nm}$) above a conductive surface. A low bias (typically $|V_S| < 3 \text{ V}$) is applied between the sample and the tip, promoting the tunneling of electrons between the two at a rate proportional to the local density of states of the sample under the terminal atom of the tip, providing the technique its lateral sensitivity. STM's sensitivity perpendicular to the sample plane is even higher since the tunneling current changes by an order of magnitude with $\sim 1 \text{ \AA}$ change in the tip-sample gap distance. In the typical mode of operation, the tunneling current is

recorded and held constant by adjusting the gap distance via a feedback loop. As the tip is scanned over the surface using x,y piezos, the feedback voltage applied to the z (out of plane) piezo is recorded. Well-defined structures like step-edges and atomic lattices can be used to calibrate the piezo, allowing the applied voltages to be converted to distances. Changes in the tunneling current and other observables, as discussed in many of the upcoming chapters, can be measured with a step-size of $\sim 0.3 \text{ \AA}$. Given that the covalent diameter of a carbon atom is $\sim 1.4 \text{ \AA}$, the STM an excellent tool for exploring systems at the atomic level.

Investigations on the single electron switch, requiring the capability to measure sub-molecular electron dynamics with millisecond time resolution, demonstrate the power of scanning tunneling microscopy (STM) for single molecule studies. Despite having the necessary spatial resolution, the millisecond time resolution of STM and other electron probe microscopies, is not high enough to capture the ultrafast nuclear and electron dynamics within a single molecule. Lee et al. demonstrated a way of extracting ultra-fast time information by first measuring the emitted electroluminescence (EL) spectrum from a single molecule with sub-nanometer spatial resolution. Utilizing the phase information contained within the EL spectrum's Fano line profiles, femtosecond-time information was extracted[1]. Alternatively, the advent of femtosecond visible/NIR lasers[17] has enabled the study of ultrafast molecular dynamics albeit without the same degree of spatial resolution[18, 19]. Successfully coupling these techniques would allow for the study of atomic and electronic motions on their relevant time and space scales. An ultrafast laser-coupled STM offers one promising method for exploring this regime[20, 21]. Crocker et.al. introduced the ultrafast THz-STM with 2 nm spatial and $< 500 \text{ fs}$ temporal resolution[22]. Jahng et.al. introduced ultrafast pump-probe force microscopy as a method for measuring the material's nonlinear polarization with $< 5 \text{ nm}$ spatial and ps temporal resolutions [23, 24]. Kravtsov et.al. demonstrated enhanced four-wave mixing at the apex of a gold tip, using it to achieve $\leq 50 \text{ nm}$ spatial resolution with $< 16 \text{ fs}$ temporal resolution[25]. Four-wave mixing spectroscopies offers an opportunity to track molecular vibrations on femtosecond timescales[26]. Mapping

the time-dependence of vibrations within a single molecule would realize a true milestone in chemical imaging and analysis.

Before joint time-space vibrational imaging can be realized, spatially-resolved vibrational imaging must be understood and mastered. Optical vibrational spectroscopies like Raman and IR spectroscopy, then, become attractive tools for accomplishing this goal. While AFM-IR is promising, achieving resolutions $< 50\text{nm}$ [27], it is limited to IR frequencies and, unlike Raman, cannot use shorter wavelengths to excite electronic resonances, enhancing the signal levels. More importantly, Raman-type processes can be observed in the visible, simplifying the experimental design and allowing future experiments to be done with ultrafast visible/nir laser systems.

Unfortunately, Raman scattering is a feeble effect. Given a typical molecular Raman cross-section ($10^{28} \text{ cm}^2\text{sr}^{-1}$), laser intensity ($1 \text{ mW}/\mu\text{m}^2$), spot size ($5 \mu\text{m}^2$), collection solid angle (2.7 sr), and efficiency (10%), a typical Raman setup's detection limit is around 10^6 molecules. To obtain the required signal enhancements, the community has turned plasmonics. Visible radiation can excite surface plasmons, or the collective oscillation of electrons, in materials like silver and gold. When excited in nanostructures, such as nanoparticles or atomically sharp tips, plasmons greatly enhance ($> 100\text{x}$) and localize ($< 10 \text{ nm}$) optical fields. These so-called "hot spots" tremendously boost the sensitivity of optical spectroscopies toward the single molecule limit[28, 29]. Surface-enhanced Raman spectroscopy (SERS) and tip-enhanced Raman spectroscopy (TERS) are two techniques that make full use of enhanced local field produced by metallic nanostructures. By illuminating the tip-sample junction of a STM, TERS can provide chemical information to compliment the STM's spatial resolution[28, 30]. The high optical field enhancements produced at the apex of the STM tips enables optical spectroscopy below the diffraction limit.

For many years, successes with this approach have mainly been limited to relatively large but bright dye molecules like R6G[31] and BCB[32] through electronically-resonant Raman, with the highest spatial resolutions ranging from 3 to 15 nm. A notable exception is the

sub-nanometer spectroscopic resolution recently achieved on a single porphyrin molecule[33] and carbon nanotube[34]. Such high spatial resolution is attributed to spectrally matching the resonance of the nanocavity plasmon to the molecule's vibronic transitions. Numerous new theories have been brought forward in an effort to explain this unanticipated spatial resolution. In general, it is accepted that morphology on the atomic scale plays a fundamental role in both the localization of the field and spectrum of the associated resonance[35–37].

Chapter 1 introduces the power the STM through the detection and analysis of a single-electron switch. The remainder of thesis focuses on the development and realization of sub-nm spatially resolved TERS. Chapter 2 presents the initial TERS results, demonstrating the complexity of the observed signals but, more importantly, the ability of TERS to observe single-molecule chemistry. The lack of spatial resolution in those experiments were determined to be due to an ineffective TERS tip. Chapter 3 addresses this critical issue and presents a tip fabrication method proven to provide TERS signals with sub-nm spatial resolution. The final three chapters summarize and discuss the numerous observations made possible with the newly-processed tips. Chapter 4 presents our lab's first demonstration of sub-nm spectromicroscopy. For the first time, we were able to observe the plasmonic cavity, formed by the tip-sample junction, enhance the signal from individual molecules. These resonances are explored and discussed. The sample, however, is quite complicated, containing a combination of two polyatomic molecules. Chapter 5 avoids this issue, going on to present sub-molecular TERS maps of cobalt tetraphenylporphyrin (CoTPP). Given the multiplexed nature of the technique, by measuring the full spectrum at each point on the surface, it is termed tip-enhanced Raman spectromicroscopy (TER-sm). All of these initial chapters demonstrate the complexity of near-field spectra, which change dramatically depending upon the local field intensity and gradient as well as the molecule's orientation and electronic resonances, not to mention the coloring of this complex spectrum by the tip-sample cavity resonances. In an effort to simplify the analysis and aid in our understanding of this complex environment, Chapter 6 introduces a new scanning-probe spectromicroscopy

technique wherein a single CO molecule is used as a reporter of the local potential energy surface. CO Stark-shift imaging offers chemical and physical information seemingly limited only by the resolution of the STM itself. This new approach, coupled with the included tip fabrication method, has the potential to revolutionize surface chemical analysis.

Chapter 1

Single Electron Switch

1.1 Experiment and Discussion

A single Zn-etioophyrin radical anion (ZnEtio^-) isolated in a double barrier cryogenic UHV-STM junction at 5 K and 2×10^{-11} Torr, displays an interesting switching behavior[38]. To prepare the system, neutral ZnEtio is sublimed onto a thin aluminum oxide layer grown on an atomically flat NiAl(110) surface. The ZnEtio molecule is reduced to form ZnEtio^- by injecting electrons at a sample bias $V_S > 0.7$ V. Constant current topographic scan of the stable radical anion reveals the molecule's anisotropic clover-like appearance, composed of 4 distinct lobes (Fig. 1.1). As the junction bias is ramped, along with previously understood electroluminescence[1], bistable conductance switching is observed. The onset of switching, 1.8 V, corresponds to the access of both the dianion state of the molecule, ZnEtio^{2-} , and the conduction band of the oxide.

Although this switching behavior was known within the lab prior to my involvement, additional measurements with a higher temporal resolution were needed. To characterize the kinetics of the switching behavior, current-time traces (with the feedback turned off, at $V_S = 2.0$ V) were recorded at four different tip placements, T₁-T₄, within the molecule (Fig. 1.2a). The current dependence of the process was analyzed by recording 60 s-long traces

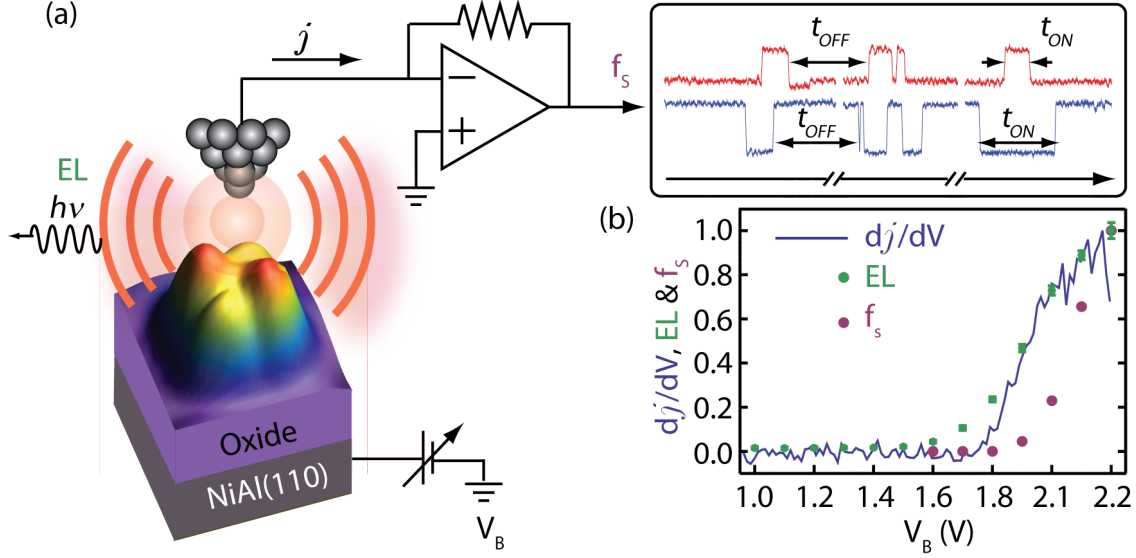


Figure 1.1: ZnEtio⁻ conductance switch. (a) Schematic of the setup with typical pre-resonant current-traces showing position dependent dichotomous positive (red) and negative (blue) switching. (b) The normalized dj/dV vs V_b curve, EL photon counts, and the switching rate (f_s) all follow the same resonant behavior associated with the onset of the dianion resonance at around 1.8 V. Reprinted with permission from reference [38], Copyright 2014 American Chemical Society.

with a 10- μ s resolution at setpoint currents ranging from 15 to 70 pA. Additionally, a bias ramp, from 1.6 to 2.2 V, was done at a setpoint current of 20 pA to obtain the frequency, f_s , curve shown in Figure 1.2b. Since switching events at lower biases are longer and less frequent, multiple 5 minute-long traces with a 1 ms resolution were recorded at biases < 1.9 V.

Figure 1.2 summarizes the data that characterizes the switching kinetics. The DC setpoint is defined as the “off” \equiv 0 state and the transient state is defined as the “on” \equiv 1 state. The switching rates for any of the single position measurements is modeled by first order kinetics:

$$0 \rightarrow 1; \quad r_+ = j_0\sigma_{01} + k_{01} \quad (1.1a)$$

$$1 \rightarrow 0; \quad r_- = j_1\sigma_{10} + k_{10}, \quad (1.1b)$$

where $j_{0/1}$ is the current level (electrons s⁻¹) of the off/on state, σ_{nm} is the probability

(transitions per electron) that a tunneling electron triggers the transition from state n to m , and k_{nm} is the spontaneous switching rate constant (s^{-1}) for transitions from state n to m . The amplitude of the switch is a function of tip placement,

$$\delta j(x, y) \equiv j_1(x, y) - j_0, \quad (1.2)$$

is readily seen by polarity differences between the four tip placements. T_1 and T_3 have a positive amplitude while T_2 and T_4 have a negative amplitude. Whenever switching frequencies are within the gain-bandwidth of the current preamplifier (800 Hz at 10^{10} gain), the measured pulse height distribution (Fig. 1.2c) is bimodal. However, if the on-time for the switch approaches the response time of the preamplifier, as it does at T_1 and T_3 , corrections need to be made to obtain the true height and on-time of the switch. A piecewise deconvolution of the pulse shapes accounts for the response function of the amplifier, allowing the original signal to be extracted (see Section 1.2).

With these corrections, the dichotomy of all switching events is confirmed. Additionally, reducing the bias lowers the switching frequency and increases on-times, producing bimodal pulse height distributions (PHDs) for all tip placements.

Discriminator levels are used to create the residence time histograms (Fig. 1.2e,f), showing an exponential probability density, $P_{0/1}$, characteristic of Markovian processes:[39]

$$P_{0/1} = \frac{1}{\tau_{0/1}} \exp(-t/\tau_{0/1}), \quad r_{+/-} \equiv 1/\tau_{0/1} \quad (1.3)$$

As shown in Eq. 1.1 and Fig. 1.2g,h, the rates obtained from fitting Eq. 1.3 to the resident time distributions are linearly dependent on the current, $j_{0/1}$, with intercepts and slopes giving k_{nm} and σ_{nm} , respectively. The extracted parameters are summarize in Table 1.1.

Even at 5 K, there remains a finite position-independent probability for the molecule to spontaneously switch “on” in the projected limit of $j = 0$: $k_{01} \approx 30 \text{ s}^{-1}$ (Table 1.1). In contrast, the spontaneous relaxation rate k_{10} is highly dependent on tip placement with

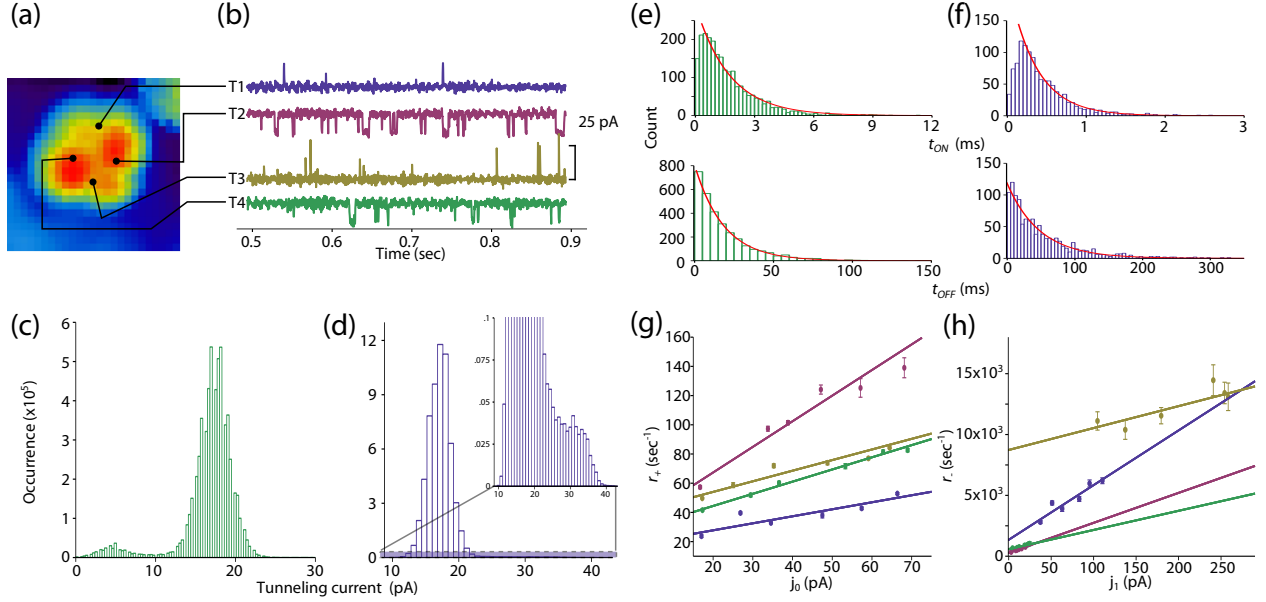


Figure 1.2: High-resolution switching analysis. Time traces recorded at $V_b = 2.0$ V and $j_0 = 20$ pA for 4 different tip placements (a) are vertically offset for clarity (b). (c) Pulse height distributions (PHD) at T4 is bimodal, indicating dichotomous negative switching. (d) PHD at T1 is broadly distributed due to the instruments response time. (e,f) Histograms for on/off-times have an exponential dependence, characteristic of a Markovian process. The peak seen at non-zero t_{ON} (f,top) is mostly due to under-counting short switches due to instrument limitations. (g,h) r_+ and r_- are linearly dependent on j_0 and j_1 , respectively. Reprinted with permission from reference [38], Copyright 2014 American Chemical Society.

T	k_{01}, s^{-1}	$\sigma_{01}, (\times 10^{-6}/e^-)$	k_{10}, s^{-1}	$\sigma_{10}, (\times 10^{-6}/e^-)$
1	18.1 ± 5	0.0769 ± 0.02	1570 ± 500	6.29 ± 1
2	32.3 ± 8	0.280 ± 0.03	283 ± 6	3.94 ± 0.1
3	39.5 ± 4	0.116 ± 0.02	4380 ± 3000	12.3 ± 3
4	27.8 ± 2	0.141 ± 0.006	585 ± 9	2.51 ± 0.3

Table 1.1: Stimulated transmission probabilities (σ_{nm}) and spontaneous rate constants (k_{nm}) for the 4 tip positions. The uncertainties are the standard errors from the linear fits. Reprinted with permission from reference [38], Copyright 2014 American Chemical Society.

rates that are 1 to 2 orders of magnitude larger than that of k_{10} . Since it is established that this is a two-level system, the observed variation of k_{10} is most likely due to perturbation by the tip. Higher currents equate to smaller tip-molecule distances, leading to perturbation effects. If such effects could be eliminated, a single excited state lifetime, $1/k_{10}$, would be expected across all tip positions. Through detailed balance, the energy difference between

the two levels is extracted,

$$\Delta E = k_B T \ln(k_{10}/k_{01}). \quad (1.4)$$

At negative switching locations, T_2 and T_4 , $\Delta E = 0.94$ and 1.3 meV, respectively, while at positive switching locations, T_1 and T_3 , $\Delta E = 1.9$ and 2.0 meV, respectively. Tip perturbation at positive switching positions are on the same order of magnitude as the energy level difference itself, ~ 1 meV. This small energy level difference, and the corresponding change in the topography, is observable with the STM and signifies a topography determined by vibronic density[40].

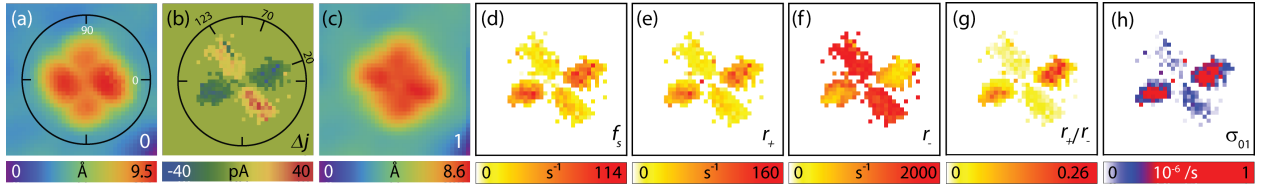


Figure 1.3: (a) Constant current topography of state 0 (42x42 Å). (b) Switch amplitude amp. (c) Extracted constant current topography of state 1. (d-h) Derived functional image maps of the frequency, “on”-rate, “off”-rate, duty cycle, and transition probability, respectively. Reprinted with permission from reference [38], Copyright 2014 American Chemical Society.

This same analyses were then carried out on each pixel of a 38x38 grid to determine the full spatial dependence of the switch, producing functional images (Fig. 1.3). Each pixel is the result of a 2 s trace with 500 μm resolution. As implied by T_1 - T_4 , the amplitude map has zones of positive and negative conductance switching (Fig. 1.3b). Interestingly, the polarity changes from positive to neutral to negative as the polar angle is changed from 123° to 70° to 20° , respectively, acting as three-throw bipolar rotary switch.

Understanding that the amplitude of each switch corresponds to the change in the topography between the two states, the δj map and the state 0 image (Fig. 1.3a) are used to calculate the transient state 1 constant current image (Fig. 1.3c). Since tunneling current

is given as[41]

$$j = j_0 \exp(-2\kappa(z - z_0)), \quad (1.5)$$

the topography of the “on” state at the setpoint j_0 , $Z_1(x, y)|_{j_0}$, is defined as

$$Z_1(x, y)|_{j_0} = Z_0(x, y)|_{j_0} - \frac{1}{2\kappa} \ln\left(\frac{j_0 + \delta(x, y)}{j_0}\right), \quad (1.6)$$

where j_0 is the current at the reference point z_0 and $\kappa = 1 \text{ \AA}^{-1}$. The resulting image, Figure 1.3c, shows that the vibronic density is rotated with respect to that of state 0, and is more evenly distributed across the four lobes. Thus, despite the fact that it takes our instrument ~ 2 minutes to record a topographic image (Fig 1.3a), the above transformation provides an estimated topography for a state with a millisecond lifetime.

Figures 1.3d-h show the functional images of the switching frequency, transition rates “on” and “off”, duty cycle r_+/r_- , and probability σ_{01} . Coupled with the δj map, these functional images provide the required information to predict and control the polarity, frequency, amplitude, and duty cycle of this conductance switch. Furthermore, Fig 1.3a and 1.3c provide the spatial distribution of the vibronic densities of the initial and final states.

It is surprising that the excited state has such a long lifetime, $1/k_{10} \approx 1 \text{ ms}$, despite being characterized by only a 1 meV energy difference. This suggests that the transition is a forbidden process, specifically the spin-flip of the odd electron in the ZnEtio^- radical. The spin-orbit coupling needed to break the spin degeneracy in ZnEtio^- has been estimated to create a splitting of 0.1 meV[42], an order of magnitude smaller than our observations. However, vibronic distortions[43] and conical intersections strengthen the coupling and increase the splitting, respectively, resulting in vibronic splittings of around 1 meV for aromatic molecules like benzene and butadiene[44], in line with the current observations.

1.2 Analysis and Correction of the Switching Traces

1.2.1 Laplace Transform

The residence time, $t_{ON/OFF}$, is defined as the time spent in a particular state, on (1) or off (0), before switching away from it (Fig. 1.4). On up-switching lobes, t_{ON} is often on the order of our preamplifier rise-time, $\tau_{rise} = 450 \mu s$, especially at resonant conditions. Here, τ_{rise} is the time it takes to rise from 10% to 90% of the input impulse signal. Since we assume that the switching behavior is impulsive, with instantaneous changes in conductivity (square pulse) relative to the response time of our electronics, the output signal is a convolution of our preamplifier's response function and this square pulse input.

Despite its complexities, the preamp can be viewed as a simple RC circuit. A RC circuit converts a square pulse input current, $I(t)$, into a time-dependent voltage signal, $V_0(t)$:

$$I(t) = \frac{v_0(t)}{R} + C \frac{dv_0(t)}{dt} = h[u(t-a) - u(t-b)] + m, \quad (1.7)$$

where h is the magnitude of the current step, m is the level of the “off” state, a and b are the start and stop times of the switch ($b > a$), $v_0(t)$ is the preamplifier's output voltage, R is the circuit's resistance (gain), C is the circuit's capacitance, and

$$u(t-a) = \begin{cases} 1 & \text{if } t > a \\ 0 & \text{if } t < a \end{cases} \quad (1.8)$$

This linear differential equation can be solved using Laplace transforms.

$$\mathcal{L}\{v_0(t)\} = V_0(s) \quad (1.9)$$

$$\mathcal{L}\{1\} = \frac{1}{s} \quad (1.10)$$

$$\mathcal{L}\{e^{at}\} = \frac{1}{s-a} \quad (1.11)$$

$$\mathcal{L}(f') = s\mathcal{L}(f) - f(0) \quad (1.12)$$

$$\mathcal{L}\{f(t-a)u(t-a)\} = e^{-as}F(s) \quad (1.13)$$

$$\mathcal{L}^{-1}\left\{\frac{1}{s}F(s)\right\} = \int_0^t f(\tau) d\tau \quad (1.14)$$

Take the Laplace transform of the middle and right hand side of Eq (1.7) using Eq (1.9-1.13).

$$\mathcal{L}\left\{\frac{v_0(t)}{R} + C\frac{dv_0(t)}{dt}\right\} = \mathcal{L}\{h[u(t-a) - u(t-b)] + m\} \quad (1.15)$$

$$\frac{1}{R}\mathcal{L}\{v_0(t)\} + C\mathcal{L}\left\{\frac{dv_0(t)}{dt}\right\} = h[\mathcal{L}\{u(t-a)\} - \mathcal{L}\{u(t-b)\}] + m\mathcal{L}\{1\} \quad (1.16)$$

$$\frac{V_0(s)}{R} + C\left[sV_0(s) - v_0(0)\right] = h\left[\frac{e^{-as}}{s} - \frac{e^{-bs}}{s}\right] + \frac{m}{s} \quad (1.17)$$

$$V_0(s)\left[\frac{1}{R} + Cs\right] = h\left[\frac{e^{-as}}{s} - \frac{e^{-bs}}{s}\right] + \frac{m}{s} \quad (1.18)$$

Here, it is assumed that $v_0(0) = 0$. After solving for $V_0(s)$, use Eq (1.13) and (1.14) to inverse Laplace Transform the equation back again.

$$V_0(s) = \left[\frac{1}{\frac{1}{RC} + s}\right] \frac{h}{Cs} \left[e^{-as} - e^{-bs} + \frac{m}{h}\right] \quad (1.19)$$

Remembering

$$\mathcal{L}^{-1}\left\{\frac{1}{s}F(s)\right\} = \int_0^t f(\tau) d\tau = \int_0^t \mathcal{L}^{-1}\{F(s)\} d\tau, \quad (1.20)$$

$$(1.21)$$

we can use it to show

$$\mathcal{L}^{-1}\{V_0(s)\} = \mathcal{L}^{-1}\left\{\frac{1}{s}\left[\frac{1}{\frac{1}{RC} + s}\right]\frac{h}{C}\left[e^{-as} - e^{-bs} + \frac{m}{h}\right]\right\} \quad (1.22)$$

$$v_0(t) = \int_0^t \mathcal{L}^{-1}\left\{\left[\frac{1}{\frac{1}{RC} + s}\right]\frac{h}{C}\left[e^{-as} - e^{-bs} + \frac{m}{h}\right]\right\} d\tau \quad (1.23)$$

Eq (1.13) can be rewritten as

$$\mathcal{L}\{F(s)\}_{\tau-a} u(t-a) = \mathcal{L}^{-1}\{e^{-as}F(s)\}, \text{ where} \quad (1.24)$$

$$F(s) = \frac{1}{\frac{1}{RC} + s} \quad (1.25)$$

The integrand in Eq (1.23) can then be simplified using Eq (1.11) and (1.24)

$$v_0(t) = u(t-a) \int_0^t \frac{h}{C} e^{-\frac{\tau-a}{RC}} d\tau - u(t-b) \int_0^t \frac{h}{C} e^{-\frac{\tau-b}{RC}} d\tau + \int_0^t \frac{h}{C} \frac{m}{h} e^{-\frac{\tau}{RC}} d\tau \quad (1.26)$$

$$v_0(t) = \int_a^t \frac{h}{C} e^{-\frac{\tau-a}{RC}} d\tau - \int_b^t \frac{h}{C} e^{-\frac{\tau-b}{RC}} d\tau + \int_0^t \frac{h}{C} \frac{m}{h} e^{-\frac{\tau}{RC}} d\tau \quad (1.27)$$

$$v_0(t) = \begin{cases} mR(1 - e^{-\frac{t}{RC}}) & \text{if } 0 < t < a \\ hR(-e^{-\frac{t-a}{RC}}) + mR(1 - e^{-\frac{t}{RC}}) & \text{if } a < t < b \\ hR(-e^{-\frac{t-a}{RC}} + e^{-\frac{t-b}{RC}}) + mR(1 - e^{-\frac{t}{RC}}) & \text{if } t > b \end{cases} \quad (1.28)$$

where RC , the time-constant of our preamplifier, is roughly $2.2/\tau_{rise} \approx 0.2$ ms. Here, R represents the amplifier's gain (10^{10} V/A).

This equation can be rewritten to better conform with previously defined variables. Here, j_1 is the ‘‘on’’ level, j_0 is the ‘‘off’’ level or setpoint current, and τ is the preamplifier's time-constant.

$$v_0(t) = \begin{cases} j_0(1 - e^{-\frac{t}{\tau}}) & \text{if } 0 < t < a \\ (j_1 - j_0)(-e^{-\frac{t-a}{\tau}}) + j_0(1 - e^{-\frac{t}{\tau}}) & \text{if } a < t < b \\ (j_1 - j_0)(-e^{-\frac{t-a}{\tau}} + e^{-\frac{t-b}{\tau}}) + j_0(1 - e^{-\frac{t}{\tau}}) & \text{if } t > b \end{cases} \quad (1.29)$$

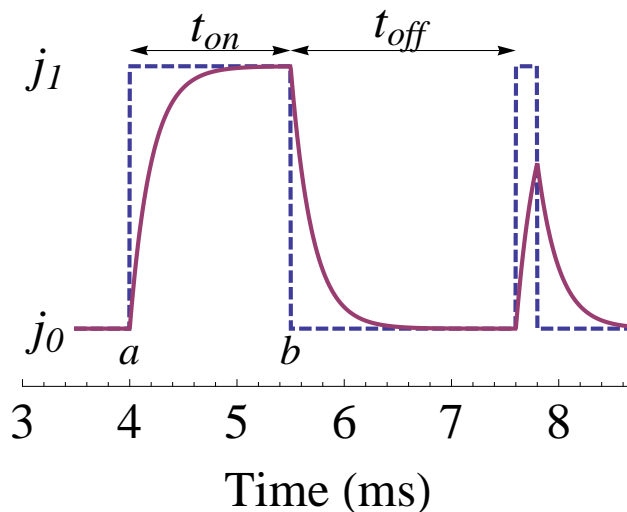


Figure 1.4: The simulated input step pulse signal (blue, dashed) is overlaid on the simulated output of our preamplifier, Eq. 1.29, (purple, solid). For this plot, $j_1 = 60\text{pA}$, $j_0 = 10\text{pA}$, and $\tau = 0.2\text{ms}$. The first pulse lasts $1.5\text{ms} = b - a$, while the second pulse lasts 0.2ms (equal to the time-constant of the preamplifier). Reprinted with permission from reference [38], Copyright 2014 American Chemical Society.

Figure 1.4 shows that as the length of the input step pulse approaches the time-constant of the preamplifier, the $v_0(t)$ fails to reach the true peak height. The preamplifier, not the system itself, is responsible for the ill-defined “on” state. By fitting individual peaks to equation 1.29, the true height of the step pulses can be extracted (Fig. 1.5).

The response of the preamplifier also affects the measured residence times. Typically, residence times are measured by calculating the time it took a step-function to pass above and then below a discriminator level. For a detector with an instantaneous response, this would be perfectly adequate. If, however, the detector has a finite response time, errors begin to develop. If the response time approaches the residence time, errors can approach and

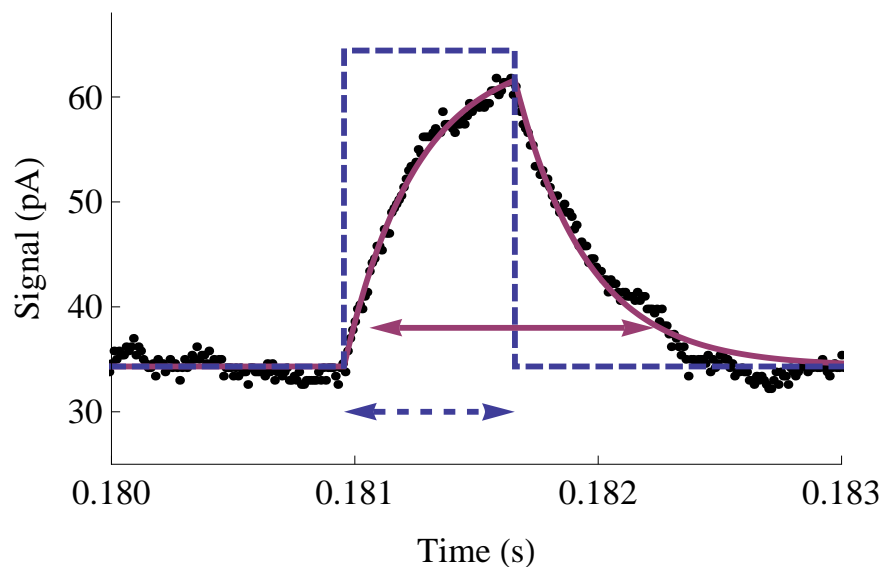


Figure 1.5: Equation 1.29 is used to create a fit (purple) of a single switching event (black) with fit parameters j_0 , j_1 , τ , a , and b . The value of j_1 from the fit is used to construct the step pulse (dashed blue). The arrows represent the residence time according to the discriminator level (purple arrow, at ~ 40 pA) versus its true magnitude (dashed blue arrow). The switching event comes from a high-resolution trace ($10 \mu\text{s}$ steps) from a point on L1 at a sample bias of 2 V and a setpoint current of ~ 35 pA. Reprinted with permission from reference [38], Copyright 2014 American Chemical Society.

exceed 100% whilst also becoming very dependent on the location of the discriminator level, as seen in Fig 1.5.

1.2.2 Implementation: On-Level Determination

Five peaks of varying heights were chosen from every trace on both up-switching lobes (L1 and L3). Each of these peaks were fit with Eq 1.29, producing 5 fit parameters: $j_0, j_1, \tau, a,$ and b . For each trace, the values of each parameter were compared across the 5 peak fits. Aside from a and b , which will vary from pulse to pulse, the parameters agreed very well with one another. Figure 1.6 shows the deviations seen in j_1 . This reaffirms the fact that (1) the setpoint current, j_0 , remained constant throughout the measurement and (2) that the system is governed by an instrumental rise-time, τ . More importantly, the fits demonstrate that up-switching is dichotomous with a singular “on” state level, j_1 . Traces taken at low, preresonant biases further demonstrate dichotomous up-switching (Fig 1.7).

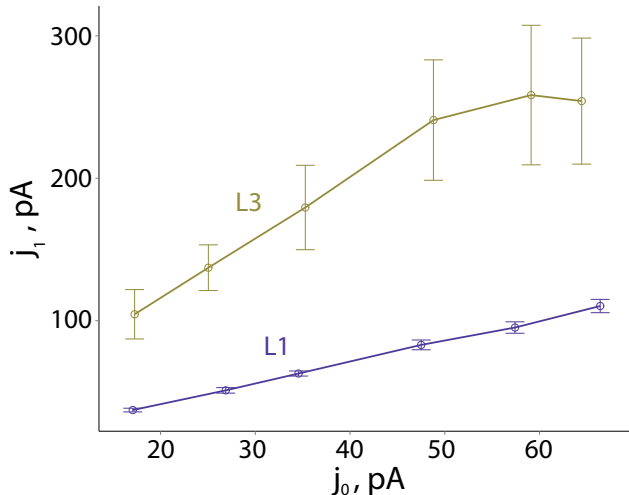


Figure 1.6: The correlations between corrected j_1 and j_0 for L1 and L3 for the high resolution traces are linear with a slope of 1.5 ± 0.02 and 3.4 ± 0.4 , respectively. The error bars are the standard deviations of j_1 . Note the small deviations in L1’s corrected j_1 distribution ($\sim 4\%$). The large deviations on L3 ($\sim 16\%$) are likely due to the high j_1 tunneling current. The tip perturbs the molecule more at higher current levels. Reprinted with permission from reference [38], Copyright 2014 American Chemical Society.

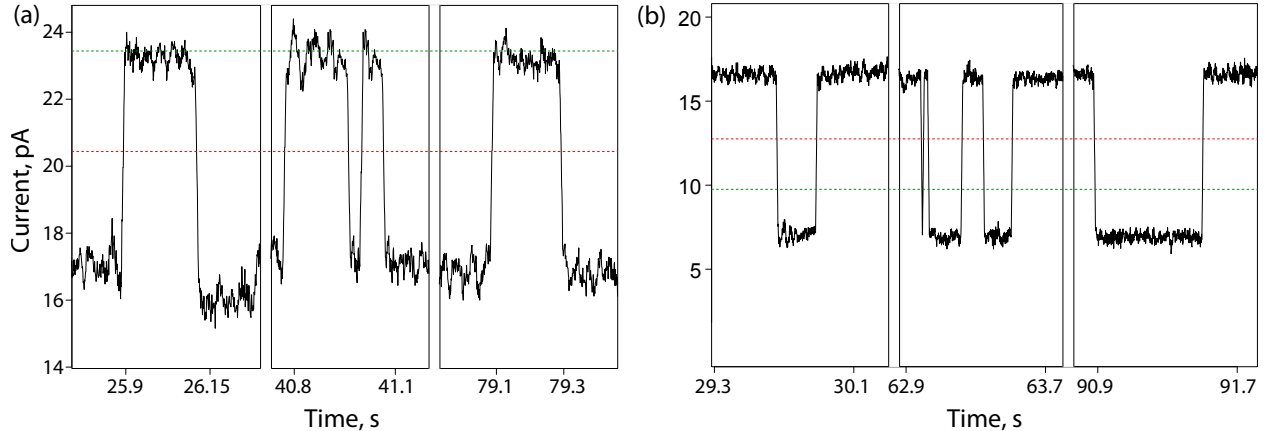


Figure 1.7: At lower biases, the on-time increases while the onrate decreases. (a) and (b) are typical low bias traces. Specifically, both are high-resolution traces taken at a sample bias of 1.7 V and a tunneling current of ~ 17 pA. (a) Positioning the tip over L1 shows dichotomous up-switching while the same over L2 (b) shows dichotomous down-switching. A 100- μ s moving average was applied to both traces to better show this switching. The red and green dashed lines signify the “on” and “off” discriminator levels. Reprinted with permission from reference [38], Copyright 2014 American Chemical Society.

1.2.3 On-Time Correction

Due to noise within the trace, switches were counted through the use of two discriminator levels. For a switch to be counted, the signal must first pass the “on” discriminator and then fall pasted the “off” discriminator (See Fig. 1.7). The “on” discriminator level, $V_{a'}$, was placed at a level 4σ above the setpoint PHD. The “off” discriminator level, $V_{b'}$, was placed 3 pA below the “on” discriminator (towards the setpoint PHD). For these traces, 3 pA was chosen as it was larger than the typical current noise in the trace. Had only one discriminator been used, the noise in the trace would have resulted in false counts.

The method used to count the number of switches produced a list of times, a' and b' , at which the trace passed above the “on” and then fell below the “off” discriminator, respectively. As shown earlier, the difference between these two values gives you t_{on} but with significant errors. However, like j_1 , these residence times can be corrected using Eq (1.29).

Eq (1.29) is simplified slightly by looking only during the rise and fall of the peak.

$$V_0(t) = \begin{cases} (j_1 - j_0)(-e^{-\frac{t-a}{\tau}}) + j_0 & \text{if } a < t < b \\ (j_1 - j_0)(-e^{-\frac{t-a}{\tau}} + e^{-\frac{t-b}{\tau}}) + j_0 & \text{if } t > b \end{cases} \quad (1.30)$$

Then, assuming values for j_0 , j_1 , and τ (taken from the average of the five fits of various peaks), one can plug $t=a'$ and $V_0(t)=V_{a'}$ into (1.30a) and solve for a . Using this solution, b is determined by plugging in $t=b'$ and $V_0(t)=V_{b'}$ into (1.30b). The corrected residence times are more accurate than just using the discriminator method. However, there is some uncertainty in the corrected residence time due to uncertainties in j_0 , j_1 , and τ .

Chapter 2

Observing the Isomerization of a Single Molecule with TERS

2.1 Introduction

With its capability for single-molecule sensitivity established[45–47], surface enhanced Raman scattering (SERS) is poised for observing single molecule chemistry. Distinct from single molecule spectroscopies that rely on fluorophores[48], since Raman probes vibrations of molecules in their ground electronic state, it provides the means to track the evolution of molecular bonds in time. While the pioneering demonstrations of single molecule SERS (SMSERS) relied on indirect evidence[49], a more compelling case for the ultimate sensitivity and power of the technique comes from the demonstration of submolecular spatial resolution in tip-enhanced Raman spectroscopy (TERS) carried out on a single molecule, in a scanning tunneling microscope (STM)[33]. The principles of SMSERS readily translate to the time domain, as recently demonstrated by tracking the vibration of single molecules in real-time[26]. The latter study underscores the requirement of repeated measurements to reconstruct the history of a dynamical process: to track chemistry in space and time, it is necessary to consider repeatable reactions. To this end, we have initiated joint TERS/STM investigations

of the prototypical molecular photoswitch: the reversible *cis-trans* photoisomerization of azobenzenes (AB). A diazine (HN=NH) derivative, where both hydrogens are replaced with benzenes, AB can exist in either planar *trans* form or in bent *cis* form. The isomerization can be induced optically, through either $S_1(\pi^* \leftarrow n)$ [50, 51] or $S_2(\pi^* \leftarrow \pi)$ [52] electronic transitions[53], thermally[54], mechanically[55], electrostatically[56], or through the application of voltage or current pulses[57]. This inherent flexibility, and the consistency of the optomechanical response of isomerization when AB is incorporated in solid matrices[58], polymers[59], and self-assembled monolayers[60], has translated into practical applications as diverse as molecular switches[61], nanomotors[62], and adaptive imaging devices[59]. The mechanisms of the homogeneous photoisomerization in gas phase and liquid phase is fairly well understood[63], with the benefit of ultrafast time-resolved studies[64], and in particular, of coherent resonant Raman scattering[65–67]. Both inversion and rotation about the N-N-C bond are implicated in the reaction coordinate, subject to substituent and solvent effects[68]. These effects may be magnified in the constrained environments provided by solid substrates used in practical applications. This is most clearly manifested in single molecule studies on metal surfaces, which we consider here.

With the demonstration that the structural change between planar *trans* AB and its bent *cis* isomer is distinguishable through STM imaging[57, 69], a significant body of work has emerged on their single-molecule isomerization reaction on metal surfaces[60]. Strong substrate effects are evident in the observation that current induced isomerization of AB occurs on Au(111)[56, 57, 69], but not on Au(100) or Cu(111)[70]. Unsubstituted AB does not photoisomerize on coinage metals; however, it readily and reversibly photoisomerizes on Au(111)[35,36] upon introduction of four bulky groups to form tetra-*tert*-butyl-azobenzene (TBA)[71, 72]. The contrast between AB and TBA on Au (111) had been taken to suggest that the *tert*butyl spacers serve to electronically decouple the molecule from the surface to allow photoisomerization. Careful structural analysis and the failure of TBA to photoisomerize on Ag(111) cast doubt on the decoupling concept[73]. Instead, photochemistry via

excitation of d-holes on gold was suggested based on two-photon photoemission (2PPE) spectroscopy and the excitation energy dependence of the photochemical steady state between *cis* and *trans* isomers[74]. This does not clarify the failure of bare AB to photoisomerize on Au(111)[71]. Indeed, explicit theoretical simulations of molecules directly excited on gold[75] even for the more tightly anchored dithiolated AB[76], show small substrate effects on nonadiabatic internal dynamics that control the photoreaction. Nevertheless, to date, TBA on Au(111) appears to be the only AB derivative that has been shown experimentally to undergo photoisomerization.

Here, through TERS trajectories, we capture the photoisomerization of an AB derivative on the silver tip of the STM. The outlier appears during the exploration of the photochemistry of [4-(phenylazo)phenoxy]hexane-1-thiol molecules (ABT) on Au(111). ABT and its vertically oriented self-assembled monolayers (SAM) have been previously investigated through resonance Raman[77], SERS[78, 79], STM[80], TERS[81], and tip-enhanced stimulated Raman spectroscopy[82]. We find that ABT lies flat on Au(111) at the given coverage, and while it undergoes current induced isomerization, it does not photoisomerize either at 405 nm, which is resonant with the $S_1(\pi^* \leftarrow n)$ transition of isolated AB, or at 532 nm, where hole-mediated isomerization is energetically accessible. Moreover, the self-assembled ABT molecules do not generate an observable TERS signal at either wavelength. However, TERS trajectories at 532 nm capture the flip-flop of an outlier that shows the characteristics of heterogeneously catalyzed chemistry of one molecule that we fail to image.

2.2 Experimental

The measurements are carried out under ultrahigh vacuum (3×10^{-11} torr), at 80 K, in an STM equipped with a parabolic mirror fitted with XYZ piezo motors for precise alignment in vacuum (see schematic in Fig. 2.1). The junction consists of an atomically flat Au(111) substrate and an electrochemically etched Ag tip[83], which is self-sputtered by

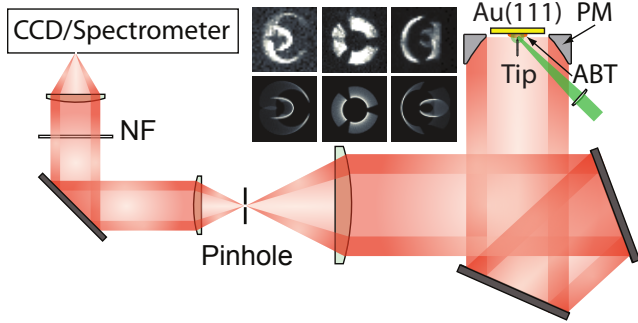


Figure 2.1: TERS setup. PM: parabolic mirror. Inset: PM images from electroluminescence (top) and their simulation (bottom, Zemax OpticStudio 14.2). In the simulation images, the PM is offset -35 , 0 , and $+30$ μm laterally and 14 μm vertically from the focus to demonstrate the alignment procedure.

neon ions and subsequently annealed. The excitation source is a 532 nm continuous wave single mode diode laser (Spectra Physics). The laser is introduced to the tip-sample junction at 45° incidence and is focused down to a spot size of ~ 10 μm using an aspheric lens. Scattered photons collected by the parabolic mirror are spatially filtered before detecting with an imaging spectrometer, equipped with a liquid nitrogen cooled CCD array (Spec-10, Princeton Instruments). The arrangement allows precise pre-alignment of the optical train by monitoring the image of electroluminescence from the silver tip apex, which is enhanced by the junction plasmon[1]. As illustrated in the inset to Fig. 2.1, by comparing to explicit simulations of the image of the sectored mirror formed at the CCD plane, the tip apex and the focus of the parabola can be overlapped with near-diffraction limited precision of < 3 micrometers (see Appendix A for additional details).

2.2.1 Chemisorption Structure

We sublime ABT molecules at 353 K for 2 seconds onto the Au(111) substrate held at room temperature, under ultrahigh vacuum. The ABT-covered gold sample is then transferred to the STM. Initially, the molecules appear in a mobile lattice-gas phase, which over the course of ~ 2 hrs transforms into the self-assembled striped phase shown in the large scale (300×300 nm^2) image of Fig. 2.2a. The assembly into a striped phase is characteristic to alkane

thiols grown on Au(111)[84], which sustains a herringbone reconstruction[85]. However, in contrast with alkane thiols, which stand up, driven by the AB-Au* binding motif[86], the ABT molecules lie flat (see Fig. 2.2b). The overlay in the close-up image of Fig. 2.2c gives the atomistic detail of the typical chemisorption structure. Pairs of ABT molecules dimerize through their thiolated tails by binding to a common gold adatom (Au*) and laterally stack into ribbons, with AB headgroups on the outside edge and alkane chains inside. While the increased spatial resolution at low bias (0.25 V) yields atomistic structural detail (Fig. 2.2b), the enhanced local density of states (LDOS) at 2.7 V identifies the S-Au*-S linkages midpoint between ABT dimers (bright spots in Fig. 2.2e). The adatom row, with interatomic spacing of 4.13 Å, is in registry with the $\langle 11\bar{2} \rangle$ direction, in excellent agreement with the model of Au*-induced self-assembly of thiolates on reconstructed Au(111)[87]. Note, each $22 \times \sqrt{3}$ unit cell of the herringbone contains an excess atom, which upon ejection to the adlayer lifts the reconstruction. In the present, on average, 0.5 atoms are expelled per unit cell. The resulting striped phase shows 18% expansion over the herringbone (see Fig. 2.2f) - an effect that we ascribe to crowding of the stacked headgroups, which forces the Au* array to deviate by 23.4° relative to $\langle 11\bar{2} \rangle$ -direction.

Beside the S-Au*-S bond that serves as anchor points, strong lateral intermolecular interactions and chemisorption of the AB head group is implied by the self-assembly of ABT into flat ribbons. The scanning tunneling spectra (dI/dV curves) of Figure 2.2g reinforce this picture. The surface state of Au(111) that appears at -0.45 V, projects through the molecule. Although attenuated relative to the bare metal, the somewhat damped profile of the surface state resonance recorded on the AB group makes it clear that the molecule is strongly coupled to the surface - it is immersed in the surface electrons of Au. A sense of the strength of the lateral intermolecular interactions is obtained from the hexagonal structure in the center of the image in Fig. 2.2b. Following the work of Cho et al.[88], this structure can be assigned to a rotating AB molecule detached from its alkyl chain. It appears to be attached to gold on one side (center of the hexagon), apparently through the O atom (Au-

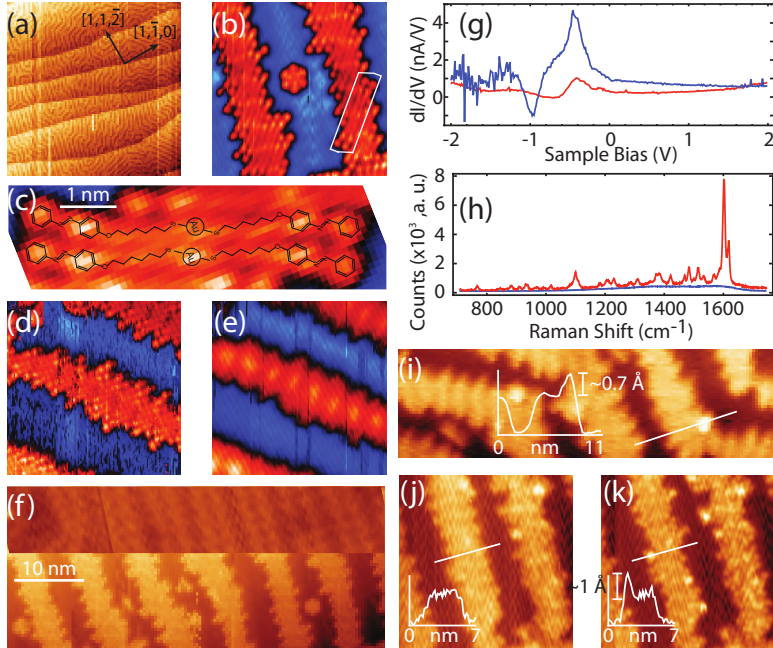


Figure 2.2: Self-assembled ABT layer and associated electronic and optical spectroscopic data. (a) Large scale topographic image of ABT covered surface. ($300 \times 300 \text{ nm}^2$) (b) $13 \times 13 \text{ nm}^2$ image of ordered ABT structure on Au(111). (c) Magnified view of the enclosed area in (b). $13 \times 13 \text{ nm}^2$ images of another area of ABT ribbons obtained at 100 pA, 49 mV (d) and 100 pA, 2.7 V (e). (f) Comparison between the Au(111) herringbone structure and ABT striped SAM. (g) STS spectra on the Au(111) surface (blue) and molecule (red). (h) Sudden emergence of intense Raman spectrum (red) after recording a silent background (blue). (i) Two photogenerated *cis*-ABTs and a line profile. (j-k) Two images taken from a voltage pulse (3 V, 3 s) sequence. Line profiles show the voltage-induced isomerization.

O-AB). While intact ABTs are permanently locked in place, the six-fold rotational barrier provided by the hexagonal mesh of the gold surface is accessible at 80 K to the isolated dissociated molecule.

2.2.2 The Failure of ABT to Photoisomerize

As previously demonstrated for AB[57] and TBA[70] on Au(111), isomerization can be induced by applying voltage pulses, and the resulting *cis* isomers appear as bright spots in the STM images (Figure 2.2i). We illustrate in Figures 2.2j,k that the voltage pulses (3 V, 3 s) are accompanied by a field effect that generates significant local disorder and leads to isomerization of multiple contiguous molecules. The contrast of the bright spots is due

to a 0.7-1Å protrusion in topography, which occurs over benzenes that bend out-of-plane upon isomerization of AB to the *cis* form (see line cut in Figure 2.2i)[57, 71]. Clearly, *cis* and *trans* isomers can be distinguished through their STM topography. Nevertheless, *cis* isomers could not be seen after extended irradiation of the ABT-packed Au(111) substrate, either at 405 nm or at 532 nm. Based on the photon flux (2.6×10^{24} photons cm^{-2} s^{-1}), exposure time of 5 h, and absorption cross section at 405 nm (2×10^{-19} cm^2), which we measure for the molecule dissolved in ethanol, we calculate a photoisomerization quantum yield less than 10^{-10} . In principle, we do not expect photochemistry in the isolated molecule since 532 nm is preresonant. However, since the d-s interband transition is accessible at 532 nm, hole-mediated chemistry, or metal-molecule charge transfer induced chemistry, can be expected[74]. Based on the net photon flux, the absence of any *cis* molecules among the 100 imaged molecules yields an upper limit for the photoisomerization cross section of 10^{-31} , which is 8-9 orders of magnitude smaller than what is seen for TBA on Au(111)[74, 89]. In effect, ABT does not photoisomerize on Au(111).

2.2.3 TERRS detection

The ordered striped SAM, which consists entirely of *trans* molecules that lie flat on the gold surface, does not produce an observable molecular TERS signal (blue trace in Figure 2.2h), which has a surface coverage of 3×10^5 μm^{-2} , therefore $\sim 10^6$ molecules in the focal volume. Through measurements of ABT dissolved in ethanol, we establish that 532 nm excitation is preresonant, with a cross section of $\delta\sigma/\delta\Omega \sim 5 \times 10^{-28}$ $\text{cm}^2\text{sr}^{-1}$, while 405 nm is resonant, with $\delta\sigma/\delta\Omega \sim 10^{-26}$ $\text{cm}^2\text{sr}^{-1}$. To reach a signal comparable to the background photon count rate of $R = 10^2$ s^{-1} , we require:

$$S = E_F n N \eta d \Omega \frac{\delta\sigma}{\delta\Omega} > 10^2 \tag{2.1}$$

in which E_F is the enhancement factor, n is the photon flux, N is the number of molecules,

η is the collection efficiency from a solid angle $d\Omega = 2.7$ sr in our setup. For an irradiation intensity of $1 \text{ mW}/\mu\text{m}^2$ ($n = 2.5 \times 10^{23}$ photons $\text{cm}^{-2} \text{ s}^{-1}$) and a conservative estimate of $\eta = 10^{-2}$, in the absence of enhancement, the signal from $N = 10^6$ molecules is near the limit of our detection sensitivity. Alternatively, an enhancement factor of $E_F \sim 10^7$ is required to see a single molecule. With the standard approximation of $E_F = (E_L/E_0)^4$, the required local field enhancement $E_L/E_0 \sim 50$ is readily reached on a silver tip of $r = 15$ nm cone radius*. If we consider the ~ 200 molecules that lie within πr^2 area of influence of the tip plasmon, then $E_L/E_0 \sim 10$ should lead to observable signal. Therefore the absence of an observable molecular line spectrum is significant. We ascribe it to surface selection rules. Since the transition dipole lies in the plane of the molecule, it is effectively cancelled by its image in the gold mirror, forbidding resonance enhancement. Also, since it is the E_z field component of the junction plasmon, along the tip z-axis that carries the required enhancement, TERS would only be expected on molecules that stand up (normal to the substrate). Even then, if the molecule is chemically coupled to the metal, molecular resonances may be quenched and broadened beyond recognition.

During extended searches, strong line spectra appear rather suddenly (red trace in Fig. 2.2h). During the several hours of irradiation preceding such an event, a population of photogenerated *cis* molecules emerges as a sprinkling of bright spots in STM images (see Fig. 2.2i). The contrast is due to a 0.7\AA protrusion in topography over terminal benzenes, due to their out-of-plane bending upon isomerization to the *cis* form (see line cut in Fig. 2.2i). The same direct observation has been previously made in the only other known case of trans-cis photoisomerization on metals, namely of TBA on Au(111)[71, 72]. And as in prior demonstrations of AB[57] and TBA[70] on Au(111), the isomerization can be induced by applying voltage pulses. This is illustrated in Figs. 2.2j,k, where we show the effect of applying 3 V pulses. In contrast with the localized and selective effect of photoisomerization, which switches spatially isolated individual ABT molecules, the voltage pulses generate significant local disorder and flip multiple contiguous molecules. The appearance of TERS

line spectra is unrelated to the *cis* molecules that we see on the gold substrate - the spectra are generally insensitive to lateral tip displacement. Spectral assignments, their assignment to TERS of single molecules located at the junction plasmon, are principally derived from Raman trajectories constructed of sequentially recorded spectra, which we describe next.

2.2.4 Meandering trajectories

From extensive recordings of Raman trajectories, either passively or during active manipulation of experimental parameters, we present selections that are particularly informative. In contrast with ensemble spectra, which measure invariants that survive orientational averaging, the TERS spectra show fluctuations in intensity and frequency. Intensity fluctuations are expected in the SM-TERS because of the tensorial nature of Raman scattering: line intensities depend on the orientation of a molecule relative to incident and scattered fields and its position in field gradients that may vary on molecular length scales[90]. In RR, the differential interaction of ground and excited states with the environment dominates spectral fluctuations[91]. Therefore, to the extent that molecules are not frozen, TERS intensities should fluctuate in the SM-limit. Frequencies, on the other hand, may fluctuate due to changes in binding structure, and due to Stark shifts induced by the junction potential[92]. We qualify as meanderers, spectral lines that undergo shifts larger than their linewidth. Examples of such meandering trajectories are shown in Figure 3. Each consists of 300 frames recorded with an acquisition time of 1 s/spectrum. Both are recorded under conditions where we see strong fluctuations, at a junction bias of 3 V and at high laser intensity of 1 mW/ μm^2 .

The trajectory in Figure 2.3a starts with a few weak vibrational peaks that persist in frames 1-37. The spectrum abruptly disappears in frame #37 to suddenly reappear in frame #71. Meandering, with mode specific spectral shifts as large as 20 cm^{-1} is seen in frames #71 through #126, along with the appearance of previously invisible lines. Example spectra at frames #87 and #92 are shown in Figure 3c. After several blinking events, whereby

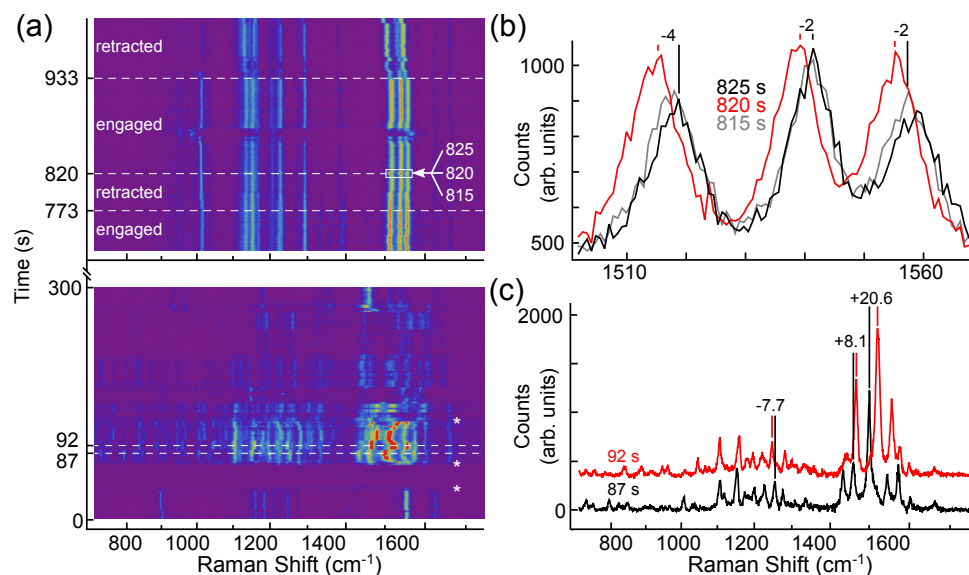


Figure 2.3: Meandering Raman trajectories (100 pA, 3 V, background subtracted). (a, bottom) Trajectory of strong fluctuations. Linecut spectra taken at 87 and 92 s are shown in (c) to highlight the blue and red spectral shifts. *37, 71, and 126 s (see main text). (a, top) More stable trajectory with a change in gap distance at 773, 820, and 933 s (dashed lines). The tip was retracted (170 nm), engaged, and retracted again in sequence. (d) Linecuts of a small region (white box in a, top) showing the transient red shift upon engaging of the tip at 820 s.

the entire spectrum disappears and reappears, a weaker meandering trajectory appears to persist for the duration of the record. The more stable trajectory is observed after 700 s (Fig. 2.3a, top panel), with the tip engaged in tunneling mode. The tip is then retracted by 170 nm at frame #773, with insignificant effect, suggesting that the observed molecule is now on the tip. The tip is engaged back to tunneling mode at #820, with a noticeable and transient red-shift of the main vibrational frequencies (Fig. 2.3b), which gives the sense of a molecule being mechanically squeezed under the closing junction. The retraction of the tip in frame #933 triggers spectral fluctuations, along with an isomerization event, which we address more thoroughly below. Here, we note tip induced perturbations that are local in nature, and concerted meandering and blinking, characteristic to spectroscopy in the single molecule limit. Spectral shifts comparable to what is seen in Fig. 2.3c have been observed previously in low temperature TERS[93], and have been ascribed to variations in adsorption sites. However, the correlation in meandering amplitude and junction bias that we see is

more consistent with vibrational shifts that occur in biased break-junctions. Nonconductive molecules that bridge the junction are subject to large potential drops of $\sim V/\text{nm}$, which is the more likely cause of the large spectral shifts at a junction bias of 3 V. Accordingly, the first trajectory in Fig. 2.3a appears to be that of a molecule(s) attempting and failing to cross the junction; while the second trajectory appears to be that of a molecule on the tip-side, after having crossed over. Ironically, we do not see the TERS active molecule via its STM image. This is perhaps not too surprising, since the area spanned by the tip plasmon is much larger than the atomically sharp apex used in imaging. Indeed, in the captured anecdote, the molecule appears to cross the junction by sidestepping the apex while the tip is engaged in tunneling mode.

2.2.5 Isomerization of a single molecule

A three-minute record of the Raman trajectory in which the isomerization of a single molecule is captured, in the form of bimodal switching between two spectra, is shown in Fig. 2.4. The two distinct color-coded spectra in Fig. 2.4a are sampled from the indicated lingering periods of the trajectory (Fig. 2.4c). The time course of a representative pair of anti-correlated vibrational lines, at Raman shifts of 1160 cm^{-1} and 1524 cm^{-1} is shown in Fig. 2.4d and histograms of their intensity fluctuations are shown in Fig. 2.4b. The bimodal histograms establish that each spectrum arises from a two level system, with discrete on- and off-levels given by the means x_{on} and x_{off} of the respective Gaussian distributions, and contrast between levels $n = (x_{on} - x_{off})/(\sigma_{off} + \sigma_{on})$ given by the respective standard deviations σ_{on} and σ_{off} . The flip-flop of the system between two states is recognizable by the anti-correlated on/off switching of the two vibrations. Nearly all observed vibrational lines switch in synchrony, as illustrated by the posterized trajectory in Fig. 2.4e. This discretized three-color map (clear = off, red = *trans* on, blue = *cis* on) is created using the discriminator levels shown in Fig. 2.4b,d, which, which serve as a gauge of the certainty of the state assignment. The smallest value of 1.4 corresponds to 88% certainty in state

assignment. Two peculiar instances of the anticorrelated switching are the lines at 1484 and 1539 cm^{-1} . The line at 1484 cm^{-1} is shared by the *cis* and *trans* spectra. However, the histogram remains bimodal because the line is stronger in the *cis* state. The vibration at 1539 cm^{-1} , unlike other modes, is activated just prior to the rapid switching events and turns off once the switching ceases. The nature of this vibration is intriguing, since it appears to be connected to the trigger that drives the switching activity. We conclude that: a) save for the two exceptions, all spectral features above the noise floor belong to one of two anti-correlated states, b) the off-level in both spectra corresponds to the zero baseline, with greater than 95% certainty in nine of thirteen observed lines. With statistical certainty, only one of two observed spectra is present at any given time; and this holds for trajectories recorded over the period of a day (see below). The two spectra must belong to one molecule in two different states; and given the observed state lifetimes of seconds to hours, we are forced to assign the two spectra to two structural isomers of the same molecule.

An alternate method to quantify that the trajectory consists entirely of two anti-correlated spectra is through the zero time delay cross correlation map shown in Fig. 2.5. The map is constructed by treating the Raman trajectory as a 2D array of intensities, $I(i, t)$, of i spectral elements and t time steps; then the cross correlation[91, 94] between two spectral elements is obtained:

$$X_{ij} = \frac{\alpha_{ij}}{\sqrt{\alpha_{ii}}\sqrt{\alpha_{jj}}} \quad (2.2)$$

where σ_{ij} are the elements of the computed covariance matrix

$$\alpha_{ij} = \sum_{t=0} [I(i, t) - \bar{I}(i)] \times [I(j, t) - \bar{I}(j)] \quad (2.3)$$

and $I(i)$ is the time-averaged intensity of a spectral element i . In the 2D correlation map of Figure 2.5a, the values range from the autocorrelation $X_{ii} = 1$, seen on the diagonal, to strong anti-correlation $X_{ij} = -0.81$. By setting correlations that have less than 1% statistical significance[95] to zero (white), the 2D graph appears as a three-color map, similar

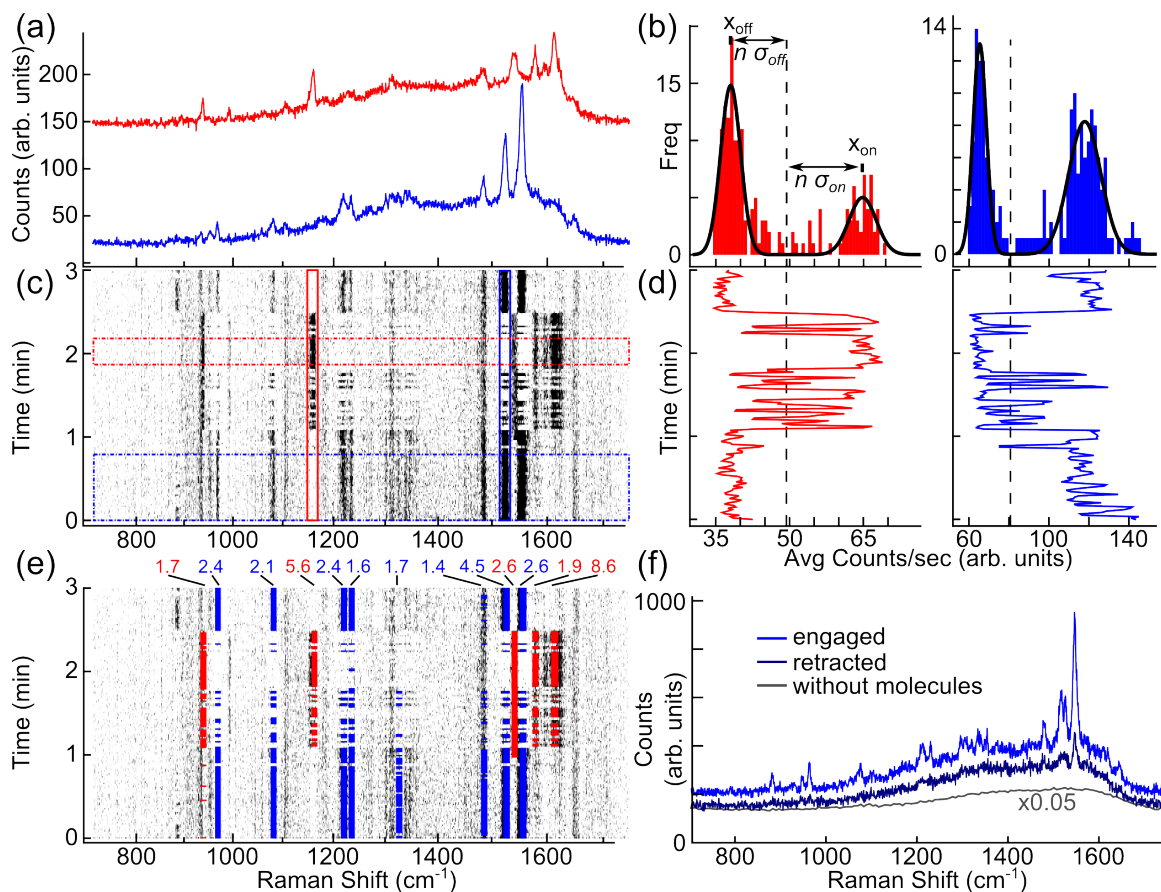


Figure 2.4: Flip-flop of a single molecule. 532 nm CW laser, 5 mW, 1 second integrations. (c) Raman trajectory (background subtracted) flip-flops between two distinct spectra. The raw time-averaged characteristic spectra from the dashed boxed regions are shown above (a). The average intensity for a 9 cm^{-1} window around 1160 cm^{-1} (red box, c) and 1524 cm^{-1} (blue box, c) switches between two intensity levels (d). The pulse-height-distribution (b) of each trace is bimodal. Solid curve = sum-of-two-gaussians fit. Dashed line = discriminator level. (e) Discriminators are used to define the two states, creating a posterized trajectory (e) where *cis* = blue, *trans* = red. The numbers above the plot = n (see main text). (f) Raman background from the clean tip-sample junction before exposure to ABT (gray) and spectra with retracted tip at 170 nm gap distance (dark blue) and tunneling condition of 10 pA, 0.25 V (light blue). The molecular spectra are offset and the Raman background is rescaled for clarity.

to the posterized trajectory in Fig. 2.4e. With >99% certainty the correlations can be discretized to $X_{ij} = 1, -1, 0$, i.e. at all time, all spectral features that are outside the noise ($X_{ij} = 0$) belong to one of two anti-correlated spectra. Accordingly, the two spectra are determined by the signed covariance, α_{ij} , which is plotted for $i = 1160 \text{ cm}^{-1}$ in Fig. 2.5b. Remarkably, the difference between two consecutively recorded spectra (Fig. 2.5c) is nearly identical to the covariance based on the full statistics of the trajectory. This underscores the strict dichotomous nature of the process, which in the present, is only compatible with the isomerization of one molecule.

2.2.6 Assignment

We tentatively assign the red and blue spectra to *trans* and *cis* isomers of the AB group, respectively. The red spectrum contains a strong peak at 1160 cm^{-1} and a triplet at 1536, 1574, and 1608 cm^{-1} . The pattern parallels the bulk *trans*-ABT spectrum (Figure 2.5d), which contains a strong peak at 1144 cm^{-1} and a triplet at 1416, 1442, 1465 cm^{-1} , except for the $\sim 100 \text{ cm}^{-1}$ shift of the triplet in the chemisorbed state. The vibration at 1160 cm^{-1} in the *trans* spectrum is an in-phase C-N stretching mode. In agreement with a prior resonance Raman analysis of AB[77], this line loses intensity upon *trans-cis* isomerization. The triplet invariably involve N=N stretching modes[79]. Their dramatic shift suggests that the chemisorption involves charge transfer between the AB headgroup and the metal substrate, directly modifying the charge density localized on the -N=N- azo-bond, which is the principal anchor of AB on coinage metals[96].

To test the general effect of charge transfer, we carry out DFT calculations of AB and its positive and negative ions (AB^+ and AB^-) using the B3LYP/6-31G* basis set, as implemented within Spartan[97]. The vibrational blue shift of the N-N stretch is incompatible with reduction. The N-N bond order shifts from its value of 1.57 in neutral AB, down to 1.2 in AB^- . Along with this, the N-N stretch shifts down in AB^- by as much as 300 cm^{-1} . In contrast, the N-N bond order remains nearly unchanged in AB^+ in its lowest energy config-

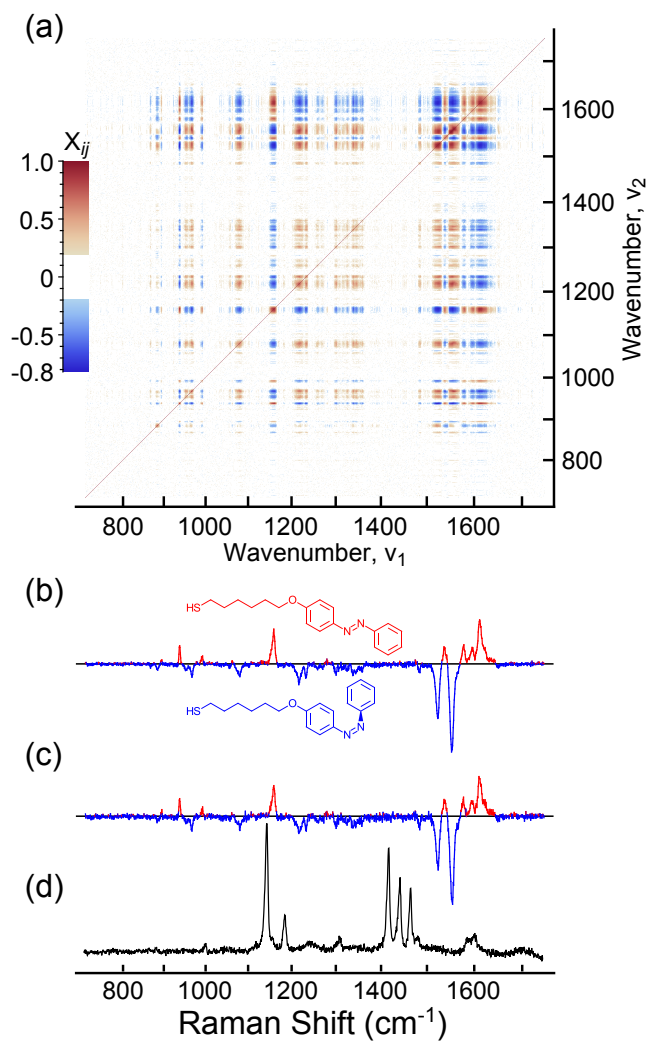


Figure 2.5: Two Anticorrelated Spectra. (a) The zero time delay 2D cross-correlation (X_{ij}) of the trajectory in Figure 2.4 shows the correlation between all the wavenumber shifts. (b) The zero time delay covariance, σ_{ij} , where $i = 1160 \text{ cm}^{-1}$ and j runs along the x-axis, and the (c) simple *trans*-ABT - *cis*-ABT difference spectrum. *trans*-ABT peaks and *cis*-ABT peaks are shown in red and blue, respectively. (d) Reference powder spectrum (black).

uration, which is nonplanar. Forcing planarity on AB^+ blue shifts the N-N frequencies by as much as 100 cm^{-1} . Also, while the first excited state in AB appears at 3.9 eV, both AB^+ and AB^- contain bright electronic transitions below 2 eV; therefore, they are resonant at 532 nm. This would explain the contrast in detectivity of the single outlier versus the ensemble of ABT molecules. Moreover, the electronic resonances in the charge transfer states provide the requisite states for there to be photoisomerization. Our analysis suggests that the outlier is an AB derivative, which is at least partially oxidized upon chemisorption on silver. Charge transfer from AB into silver, in turn, suggests the involvement of surface states. In contrast with the surface state on Au(111), which is seen at -0.45 eV in Figure 2.2d, the surface state on Ag(111) appears near the Fermi energy (-0.065 eV)[98, 99] and continues above the Fermi level[100]. Charge transfer induced by interaction with surface states leads to formation of interface states, which must undoubtedly contain strongly perturbed vibrations[101].

2.2.7 PCA of TERS spectra

Despite its success at extracting and characterizing large variations seen in two-state systems, the 2D correlation matrix method is less successful at teasing out smaller, less noticeable variations. Principal Component Analysis (PCA), on the other hand, has proven itself to be excellent at extracting variations, both large and small, within all a large variety of datasets[102]. It has been used in a variety of spectroscopies including SERS[103] and TERS[104]. This technique transforms a dataset's numerous variables into a set of new orthogonal variables, or principal components, wherein as much variation as possible is contained in as few variables as possible. It has the capability of reducing the number of variables required to summarize the variation in a dataset, with each successive principal component potentially describing different kinds of variation. Its wide-spread use across many areas of science demonstrates the technique's power.

Applying PCA to our single-molecular Raman trajectory converts 180 Raman spectra into 180 points on a 2D scatterplot of the first principal component (PC1) versus the second

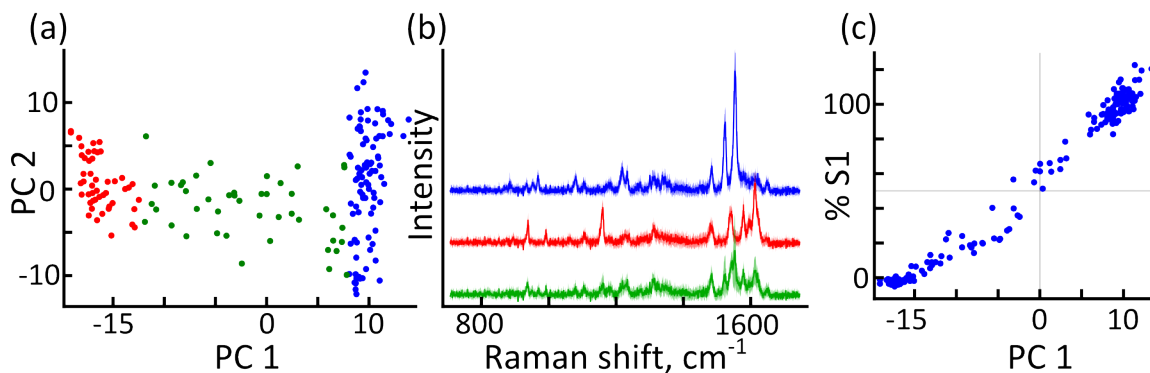


Figure 2.6: Applying PCA to Single Molecule Spectra. (a) Score plot for the first and second principal components of a single molecule Raman trajectory shows clustering at either side of the PC1 axis. (b) The spectra from the clusters chosen in (a). (c) Correlation is seen between PC1 and the percent composition of state 1 (S1, blue spectrum from (b)).

principal component (PC2) (Fig 2.6a). The points appear to separate greatly along the PC1, with slightly clustering occurring at the either extreme of the axis. The points on this plot have been colored to highlight potential clusters of points. Since each point represents an individual spectrum, the spectra contained in each cluster of points can be grouped and averaged. These PCA separated spectra, shown in Fig 2.6b, include the two spectra extracted from the 2D correlation matrix technique. Since PCA involves this very matrix, this is not surprising. However, in this case, PCA also determines the extent to which each spectrum uniquely belongs to either state. Figure 2.6c plots the extracted percent contribution of the blue state (S1) for each spectrum. These contributions were determined by fitting each individual spectrum with a linear combination of the blue (1) and red (2) spectra shown in Figure 2.6b. Values larger than 100% or less than 0% are due to the signal's intensity fluctuations. The linear transition from one state to the other demonstrates that PC1 describes the ratio of state 1 and 2 for that moment in time. This mixing likely due to switching within the observation window ($<1s$). The second principal component, PC2, gives insight into smaller variations, particularly when taking PC1 into account. At large and positive values of PC1, negative values of PC2 is correlated with the intensity of the 884 cm^{-1} peak (Fig. 2.7a) while positive values of PC1 is correlated with the ratio of the intensity of the 1555 cm^{-1} to the 1525 cm^{-1} mode (Fig. 2.7b). These small variations are

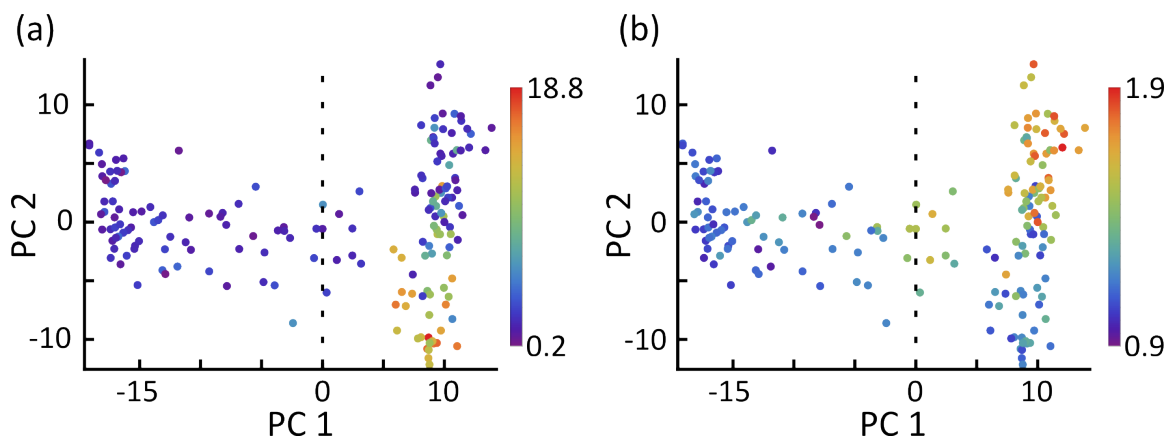


Figure 2.7: PC2 Analysis. (a) Score plot colored with the intensity of the 884^{-1} mode. (b) Score plot colored with the ratio of the 1555 cm^{-1} : 1525 cm^{-1} intensity.

harder to capture and quantify without PCA.

The real utility of this analysis is demonstrated by its ability to characterize much larger sets of fluctuating spectra, allowing the molecular state to be readily determined. Furthermore, changes between states and subtle intensity variations within a state can be quantified from an analysis of 1560 spectra taken over the course of 25 hours (Fig. 2.8). The spectra were grouped via a clustering algorithm based on their first 10 principal components. Several of these clusters are very similar and could be combined into larger groups (such as the black and gray clusters). However, doing so from other groups, like the black and purple spectra, would mask the subtle intensity differences seen in the $1500\text{-}1650\text{ cm}^{-1}$ region. As with the previous example, the sign of PC1 indicates the state of the molecule. Two distinct populations exist in the PC1 distribution, highlighting the two-state nature of this system. The proposed goal of using PCA on TERS spectra is to track the evolution of the tip-molecule system. Changes in molecular orientation, conformation, and/or charge will necessarily change the observed TERS spectrum. These changes could potentially be compared to those observed theoretically, allowing the state of the molecule to be tracked in real time.

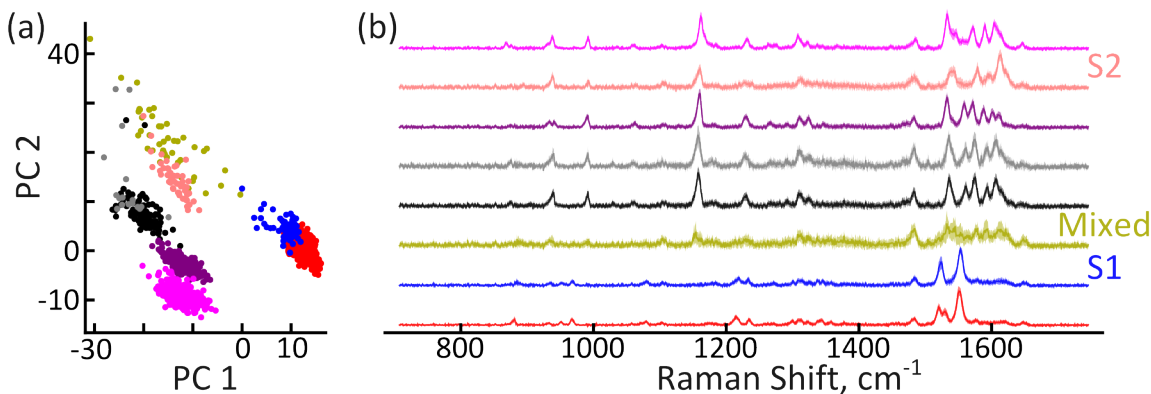


Figure 2.8: PCA tracks the molecular state in large datasets. (a) Score plot generated from 1560 spectra show the development of distinct groups. A clustering algorithm defines these groups, which are separately colored. Using $PC1 = 0$ as a delimitator, state 1 and can separated from state 2. (b) The spectra from each group are averaged to produce PCA separated spectra, colored by their group.

2.2.8 Heterogeneous chemistry

With its 12 countable flip-flops in 1.5 minutes, the Raman trajectory of Fig. 2.4 captures an unusual burst in photoisomerization activity. The trajectory is one of 13 segments recorded over the course of 25 hrs. The sequential set in which isomerization events are captured is shown in Fig. 2.9. The history line is the normalized amplitude of the pair of vibrations that exclusively belong to either *cis* or *trans* isomers. The anti-correlated switches in amplitude, identify the isomerization events. The event rate is generally correlated with the irradiation intensity, verifying that the isomerization is photocatalyzed through the (p^*n) transition accessed at 532 nm. The frequency of flip-flops of 10^{-1} s^{-1} seen in Fig. 2.4 corresponds to a photoisomerization cross section of 10^{-24} cm^2 . This is comparable to UV driven cross sections of $10^{-22} - 10^{-23} \text{ cm}^2$ seen for TBA on Au(111)[89, 105], when adjusted for the difference in absorption cross sections[106]. Note, however, that the flip-flop rate seen in the active trajectory of Fig. 2.4 is well outside the event frequency of $\sim 10^{-3} \text{ s}^{-1}$ extracted from the set of trajectories recorded over the period of 25 hrs. The burst in activity, which was heralded by the vibrational mode at 1539 cm^{-1} , appears to be triggered. Although the rarity of events limits the statistical significance of extracted rates, the observed variation in rates cannot

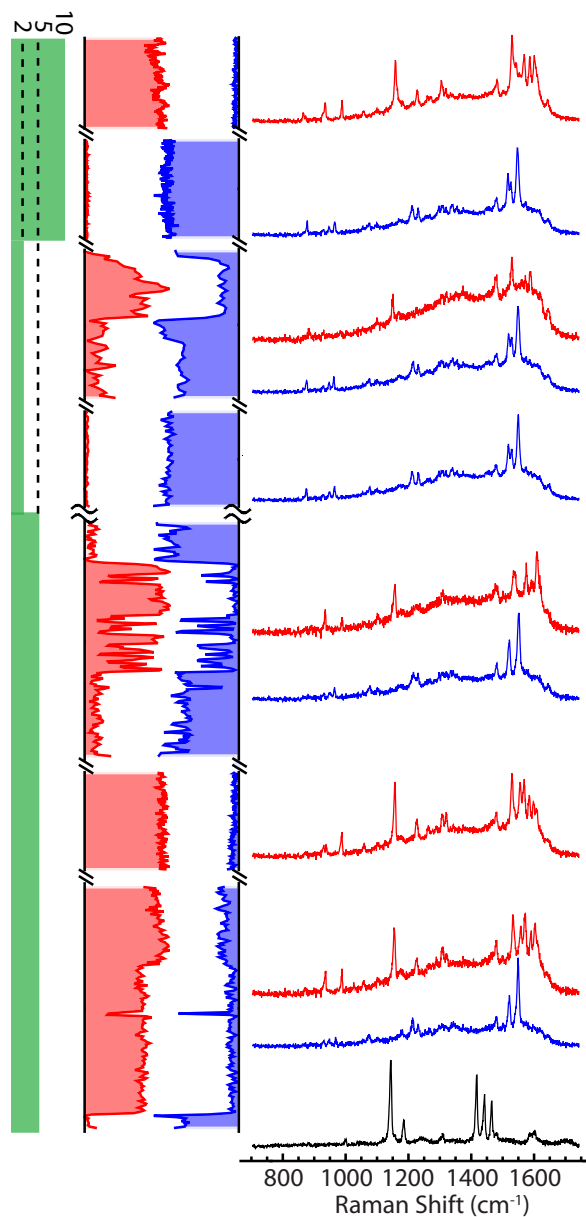


Figure 2.9: Waterfall plot of normalized Raman spectra and associated timeline of flip-flop. 7 out of 13 trajectories are sampled to show the extended trace of flip-flop. The common tunneling condition for the entire spectra is 10 pA, 0.25 V. For comparison, the *trans* powder spectrum is given at the bottom. The *trans* and *cis* spectra extracted from trajectories are color-coded in red and blue respectively, and are vertically offset for clarity. The associated laser power variation (green, in mW) is illustrated on the left. The vertical time scale is dilated to show switching events clearly when eventful trajectories are presented. Trajectories below the tilde axis breaks are 3 min-long, and the ones above are 5 min long. The *trans* and *cis* time profiles are extracted at the 1160 cm^{-1} and 1520 cm^{-1} peaks with integration window widths of 14 cm^{-1} and 8 cm^{-1} respectively. The third trajectory recorded is identical with the bimodal switching set presented in Figure 4.

be ascribed to a stochastic process with a mean value - the time course of the flip-flops of the molecule identifies heterogeneous photocatalysis. A gauge of the effective heterogeneity in its local environment is contained in the spectral variations seen in the waterfall plot of Fig. 2.9, where splittings in the triplets and appearance of new low lying modes fluctuate in time. However, we cannot pinpoint the molecule through its STM image. The TERS signal decays by 80% upon retracting the tip (see Fig. 2.4f), but it shows no dependence on lateral displacement. Once again, the molecule appears to be attached to the silver tip, in the field of the junction plasmon, the field strength of which varies with junction gap. Yet, it cannot be located under the apex where it could be imaged. In contrast with the atomically flat gold substrate, the electrochemically prepared silver tip on which the molecule appears to be, is rough. Beside a heterogeneity of adsorption sites, it provides a source of mobile Ag adatoms, which we have previously shown to catalyze chemistry[107]. And although we are left to speculate on details, the captured trajectory of the *cis-trans* isomerization has all the characteristics of heterogeneous chemistry in the single molecule limit.

2.3 Conclusion

To capture chemistry in the act, one-bond-at-a-time, it will be necessary to track structural changes atomistically, along with the evolution of bonds through their frequencies. The presented combined STM/TERS measurements set the stage for such an eventuality in real-time. While through STM we extract atomistic detail of the structure of single ABT molecules, along with clear distinction of its *cis* and *trans* isomers, it is the vibrational spectra of the molecule that identify the chemical nature of the binding, as seen by the stiffening of the normal modes that contain the N=N stretching mode. And although recorded on laboratory time scales of one frame per second, the Raman trajectories are most informative. Be it in the observation of a transient meanderer or the rare event of a molecule flip-flopping between its structural isomers, the time course of the spectra visualize details

beyond spatial microscopy. It is the observed telegraph process that rigorously establishes the single molecule nature of the observed dynamics. It is also remarkable that despite the presence of an ensemble of molecules in our field of view, it is a single molecule that leads to sharp molecular spectra. Since in the present we rely on resonant Raman scattering through the same electronic transition that leads to photoisomerization, the observable molecule is also the outlier with regard to its photoreactivity. To capture the same heterogeneous photocatalytic reaction of one molecule in real-time, on the time scale of vibrational periods of motion, the immediate challenge is to trigger the isomerization reversibly on an STM designated molecule.

Chapter 3

Fabrication and Demonstration of Silver Tips with Sub-nanometer Spatially-Resolved TERS

3.1 Introduction

Silver remains the material of choice for fashioning plasmonic tips suitable for TER-sm. Beside its superior dielectric properties, silver is less malleable than gold, therefore preferable as a scan probe; and its 4eV energy gap between d- and sp-bands ensures the absence of luminescent transitions in the visible. And although electrochemically etched silver tips serve well for STM purposes, in contrast to gold and tungsten, silver surfaces are roughened during the etching process. Both electrochemically etched and deposited silver tips are plagued by nanoscopic asperities, nanocrystalline facets, and surface irregularities due to redeposition of silver oxides during the etching process or corrosion[83, 108]. To simplify, standardize and optimize the manufacture of silver tips, we have previously developed an automated two-stage electro-chemical etching and polishing procedure[83]. The technique produces sharp Ag tips ($r < 100$ nm) with improved macroscopic smoothness, however the surface finish remains

rough, decorated with nanoscopic asperities that scatter light. As in the original discovery of the surface-enhanced Raman scattering (SERS) effect[109], hot spots on the roughened silver surface can be sufficiently bright to produce single molecule SERS[2], overwhelming the targeted TERS from the tip-substrate nanojunction. While focused ion milling can be used to superficially smoothen and sharpen silver tips, the process is time-consuming and expensive; moreover, the implanted ions degrade the surface conductivity of silver and scatter surface plasmons[110]. Through adaptations of field-directed sputter sharpening (FDSS)[111], we are able to batch process silver tips to produce optically smooth, spectroscopically silent, and nanoscopically sharp ($r < 20$ nm) tips that are suitable for TER-sm, which reliably focus visible light down to a subnanometer focal waist.

3.2 Experimental and Results

Schmucker et.al.[111] introduced and demonstrated the power of FDSS on platinum-iridium, tungsten, and hafnium diboride tips, achieving nanometric radii of curvature. Beside self-sharpening, the method produces uniformly smooth surfaces by ion polishing. In contrast to the decapitation method[112], which relies on ionization by field-emitted electrons from a negatively biased tip under processing, a positively-biased (100 - 500 V) tip is sputtered with ~ 2 keV Ar^+ ions provided by an ion gun (RBD Instruments, model 04-165). The concept of FDSS is illustrated in Figure 1. The ions are fired along the long axis of the tip, leading to a shallow angle of incidence. The surface charge induced by the positively biased tip provides a retardation field, with a strong field gradient due to the lightning rod effect. The lateral components (E_x) of the counter field deflect the incoming ions such that sputtering of the apex is reduced and asperities on the taper of the tip are polished off by grazing ions[111]. This method proves to be superior to decapitation by self-sputtering, which requires a fairly sharp apex to initiate field-emission. Furthermore, self-sputtering of soft materials such as Ag often leads to explosion of the tip apex as the negative bias is

ramped to initiate field-emission.

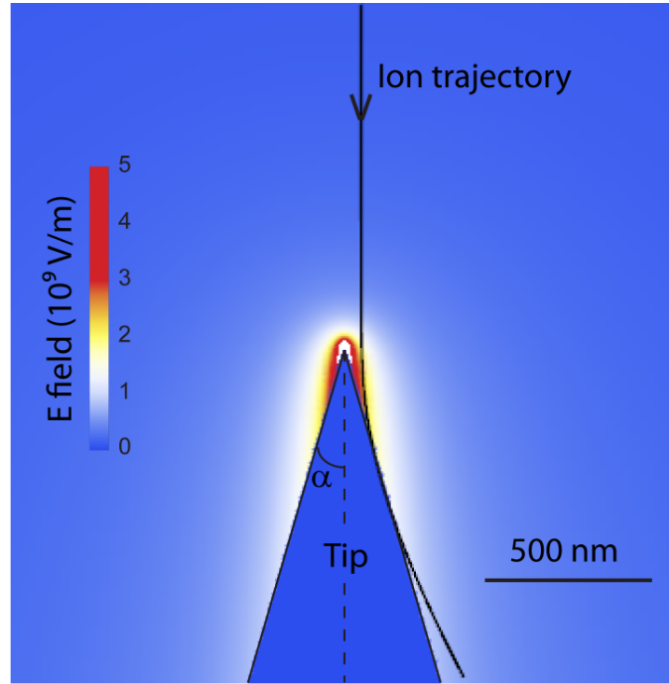


Figure 3.1: Ion trajectory overlaid on the electric field map of a positively biased tip. The tip is modeled as an infinitely sharp cone, which leads to the infinite electric field at the apex point due to the infinite charge density (lightning rod effect). The parameters used in this simulated trajectory are: incident ion energy = 2000 eV, counter bias = 500 V, cone semi angle α : 16.2 degree, initial lateral displacement of the incoming ion from the axis: 50 nm.

In Figure 3.1, the tip is modeled as a cone, and the electrical potential in the spherical coordinate system is obtained by solving the Laplace equation with the boundary condition of a potential fixed at zero on the metallic tip surface. The potential near the apex is approximated as a fractional-order Legendre polynomial[113]:

$$\phi(r, \theta) = Ar^\nu P_\nu(\cos(\theta)) \quad (3.1)$$

where, $\nu = 0.247$, and the coefficient A can be determined by the boundary condition at

large r . The electric field is calculated from the gradient of the potential:

$$E_r = -\frac{d\phi}{dr} \approx -\nu Ar^{\nu-1} P_\nu(\cos(\theta)), \quad (3.2a)$$

$$E_\theta = -\frac{1}{r} \frac{d\phi}{d\theta} \approx -Ar^{\nu-1} \sin(\theta) P'_\nu(\cos(\theta)) \quad (3.2b)$$

and the equation of motion of the ions subject to $F = qE$ is solved to calculate the ion trajectory. The electric field peaks at the apex ($r \rightarrow 0$), and its distribution is geometrically determined by the cone angle. At a given cone angle and incoming ion energy, the counter bias may be optimized to deflect the energetic ions, to optimize the polishing and sharpening processes. In practice, the ion flux is a function of the intricate shape of the equipotential determined by the receding surface of the tip(s). However, the simulation establishes an initial guess for the optimal counter bias ratio, $V_c/V_{gun} = 0.1\sim 0.3$, for the idealized individual tip.

For batch processing of tips via FDSS, it is essential that the symmetry of streamlines on individual tips be maintained. This is accomplished by providing a grounding structure separating the tips. The effect is illustrated by the finite-element simulations presented in Figure 3.2(a-b). Multiple tips held in close proximity are subject to an equipotential volume that distorts field lines (Fig. 3.2a) and the symmetry of the ion streams (Fig. 3.2b), which are restored upon their separation with a grounding plate (Fig. 3.2c,d). Our design of the grounding structure and tip holder for the simultaneous FDSS processing of 7 tips is shown in Figure 3.3a,b. The grounding (GND) structure is an aluminum disk with 7 through-holes that accept tips held in the lower aluminum holder. The GND structure is electrically connected to the grounded flange via three conductive standoffs. The tip holder is electrically insulated from the flange by a teflon spacer. The acceptable number of tips is limited by the overall size of the ion beam (diameter = 0.5"), which is expanded using an Einzel lens to cover the multiple tips. The size of the ion beam is visualized by imaging it on a phosphor screen. The arrangement yields satisfactory results under typical operating conditions of:

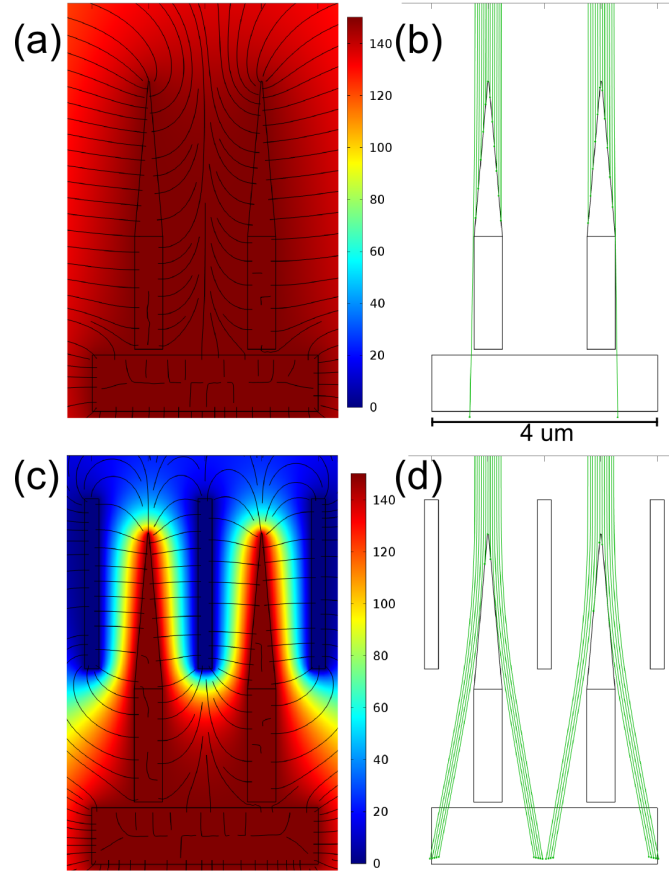


Figure 3.2: Effect of grounding structure simulated by finite element analysis. (a) Potential map of two reverse-biased adjacent tips with overlaid electric field lines in the absence of grounding structure. The space between adjacent tips becomes equipotential, which does not generate electric fields required for deflecting ions. (b) Asymmetric deflection (green) and polishing of the tips. (c) Regained symmetry of electric field lines between adjacent tips in the presence of grounding structure. (d) Cylindrically symmetric deflection of incident ions allowing batch FDSS of tips. Parameters for the simulations: tip bias = +150 V, ion beam energy = 2 keV, cone half angle = 5° , and tip radius of curvature = 50 nm.

tip bias = 100-150 V, 2 KeV Ar^+ beam under continuous Ar flow, at a steady state pressure of 5×10^{-5} Torr, in a high vacuum chamber with base pressure $< 5 \times 10^{-8}$ Torr. At a typical ion flux of $\leq 5 \mu\text{A cm}^{-2}$, the process is stopped once an overall ion dose of 30-100 mC/cm^2 is reached ($2 \times 10^{17} - 7 \times 10^{17}$ ions/ cm^2). The processing time varies from 1 to 4 hrs. This constitutes the ex-situ FDSS set-up. After transferring the tips to the UHV STM chamber, in-situ FDSS processing of individual tips prior to usage is necessary to remove adventitious carbon, which generates Raman scattering on bright tips (see below). The set-up for in situ

sputtering is shown in Fig. 3.3c.

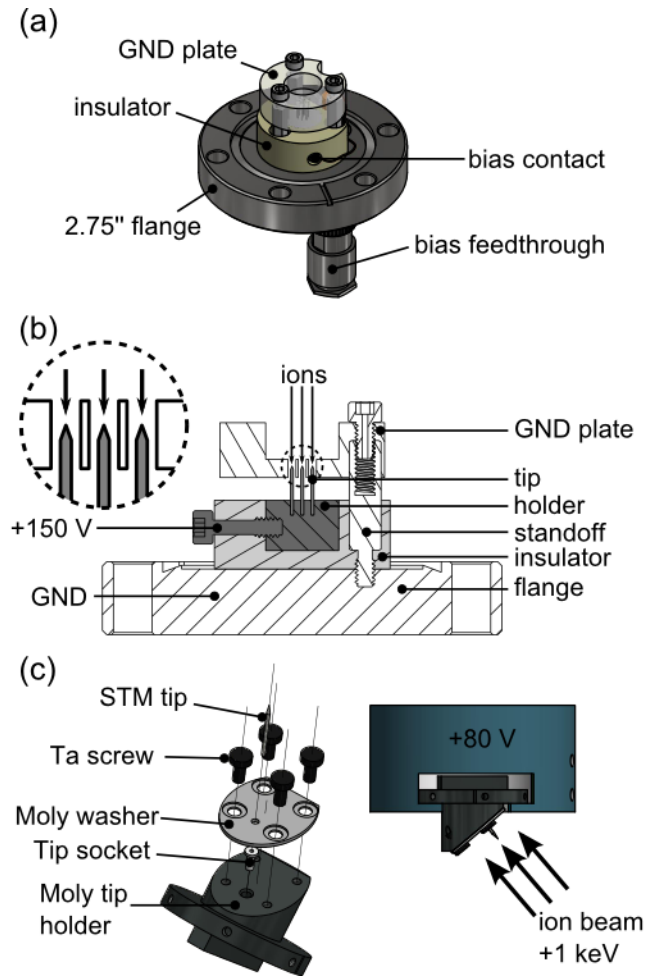


Figure 3.3: Setup for batch processing of tips. (a) A 3-dimensional view of the assembly used to perform batch FDSS on up to 7 tips. (b) A sectional view of the setup. Grounded sections are shown in white while biased sections are shown in dark grey. The GND structure is connected to the grounded vacuum chamber (flange) via the metallic standoffs. The tips are biased through their contact with the holder, which, in turn, is connected to a setscrew and a bias feedthrough (shown in (a)). Ions are shot through narrow holes in the GND plate to sputter the tips. Inset: the GND structure with holes providing individual tips with separate ground surfaces and ion channels. (c) The assembly, made of molybdenum and tantalum, used to perform FDSS in the UHV TERS-STM chamber using existing sputtering housing (blue).

The effect of ex-situ batch FDSS processing is illustrated in Figure 3.4 with the scanning electron micrographs of electrochemically etched tips before and after processing. The tips are sharpened and dramatically smoothed. The sharpest Ag tip has a radius of ~ 16 nm (Fig. 3.4d), with surface asperities removed in the final 1 μm of the tip. The treatment produces

similar results for W, Au and Al tips. Since this self-sharpening scheme retains memory of the initial tip morphology, the process greatly benefits from the electrochemical polishing scheme that we have previously introduced[83]. For instance, tips with many asperities develop undesirable multiple sharp local apices. Clearly, the final radius of curvature of the tip cone obtained by the fixed dose of ion bombardment varies, as illustrated by the examples in Figure 3.4. Additional sputtering will reduce the radius of curvature of the larger tips (Fig. 3.4f). We note that FDSS shortens the tips, by 400 to 800 nm (see Fig. 3.4g), due to the extent of undeflected, head-on sputtering.

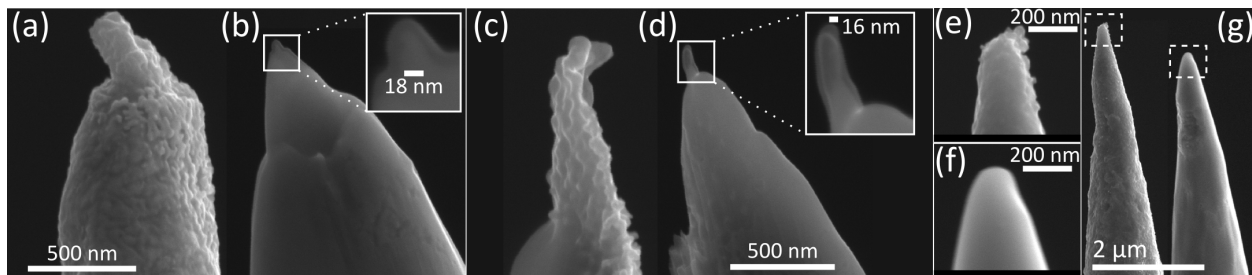


Figure 3.4: Effect of FDSS on silver tips. SEM images of the three Ag tips before (a, c, e) and after (b, d, f) a FDSS treatment show the elimination of the surface roughness and large radius of curvature common to untreated electrochemically etched tips. (g) The FDSS process reduces the length of the tip by roughly 400-800 nm.

Remarkably, highly polished surfaces of silver are highly reactive. They tarnish during the short exposure to air while transferring the tips from the ex-situ sputtering chamber to the UHV STM chamber. The formation of an adventitious diamond-like carbon (DLC) film[114] is recognized by the broad Raman band in the important range from 1200 to 1700 cm^{-1} seen in Figure 3.5a (red trace). As illustrated in Fig. 3.5a, the surface contamination can be completely removed by the in-situ FDSS treatment, for which the special holder of Fig. 3.3c is used. In this second FDSS treatment, the tip is biased at +80 V while sputtered for 10 minutes using 1 keV Ne^+ ions, with the UHV chamber backfilled to 4×10^{-5} Torr Ne gas. To ensure removal of all contaminants, 5 cycles of FDSS are used, with a net ion dose of $\sim 4 \times 10^{17}$ ions/ cm^2 (ion flux of $\sim 20 \mu\text{A cm}^{-2}$ at the tip).

Despite their disparate gross shapes, all of the tips shown in Figure 3.4 were successfully

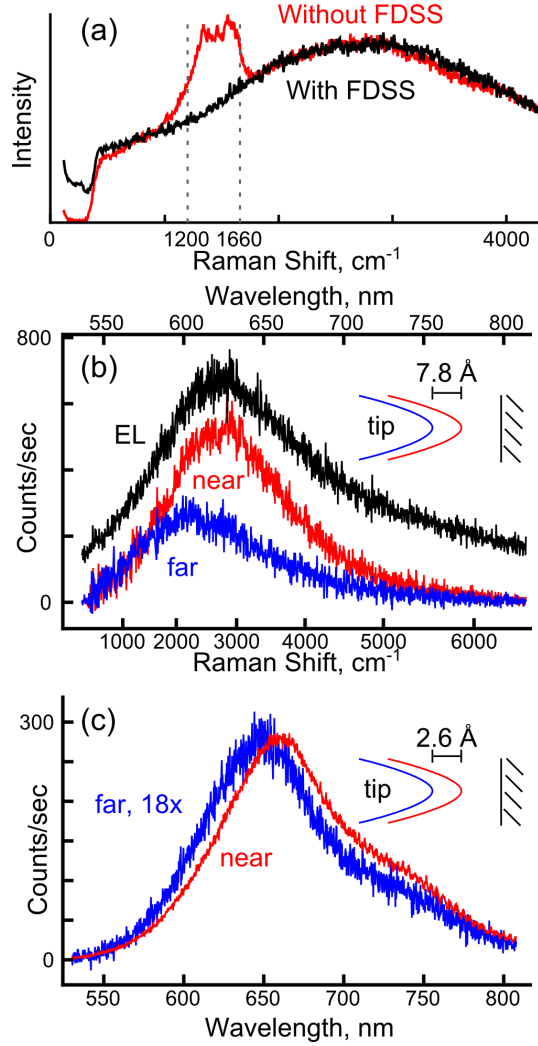


Figure 3.5: Raman spectra of processed Ag tips. (a) Comparison between an unprocessed and processed tip by in-situ FDSS. Without undergoing in-situ FDSS (red), a very important region of the tip's Raman spectrum is occupied by a broad band, a result of a mixture of sp^2 and sp^3 carbon species adsorbed onto tip's surface. After in-situ FDSS (black), these contaminants are removed, resulting in a clean background. (b) Plasmonic cavity mode formation by reshaping the tip apex through voltage pulses in tunneling regime. The resonance blue-shifts by 16 nm (419 cm^{-1} red-shift in Raman) and intensity halves upon retracting the tip by 7.8 Å (blue) from the tunneling set point (red, 0.1 nA, +0.1 V, gap 6 Å). The surface is Au(111) covered by bipyridyl ethylene (BPE) molecules. The junction is excited by 532 nm laser with the power $< 5 \mu W/\mu m^2$, and the spectra are obtained with the accumulation time of 10 s. The electroluminescence spectrum from this junction is shown as a reference (black, +2.8 V, 0.1 nA). (c) Gap-dependence of electroluminescence. The plasmon resonance blue-shifts 11 nm as the gap is increased by lowering the set point current from 2.0 nA (red) to 0.01 nA (blue) at a sample bias of +2.91 V, which is equivalent to 2.6 Å retraction.

used in TER-sm with submolecular spatial resolution. Their optical response is most directly interrogated through either electroluminescence (EL) spectra, or through electronic Raman scattering spectra of the bare junction. Since EL is generated by tunneling electrons at the protruding atom of the tip apex [115–117], the close agreement between EL and Raman spectra seen in Figure 3.5b is a good indication that the junction cavity mode is interrogated optically. This is further confirmed by the gap dependence of the observed plasmonic resonance[33, 118]. The Raman spectrum of the cavity mode recorded with the tip in Figure 3.4f is shown in Figure 3.5b; it shifts by 16 nm upon 7.8 Å retraction of the tip. Similarly, the EL spectrum shown in Figure 3.5c shifts by 11 nm upon a 2.6 Å retraction. The red shift of the spectrum as the gap is closed is consistent with the coupling of the tip plasmon with its mirror image in the metallic substrate, as generally expected for binding dipolar plasmons[119]. The sensitivity of the optically probed plasmonic resonances to atomic scale variation in the junction gap validates the utility of a tip for TER-sm, since it establishes that the nanocavity mode is coupled to the far-field and is the sole source of the observed Raman scattering. Out of the three tips processed through the FDSS method, all three produce the signature of field confinement in the nanocavity, while no such signature could be found in the prior 40+ untreated electrochemically etched silver tips.

While the plasmonic resonances of different tips vary, they can be fine-tuned by reshaping the tip apex. This is accomplished by applying high-voltage pulses (100 ms, 10 V) while the tip is positioned in the tunneling regime (junction bias = 2.2 - 3.0 V, setpoint current = 0.1 nA). Since the resulting structure of the apex is unknown beyond its atomic protrusion, which is verified by the sharpness of STM topographic images, the intensity of EL is used to gauge a tip’s brightness (enhancement property). In other instances, and in particular during room temperature measurements, the cavity modes can be seen to evolve while scanning the surface. Indeed, tips may completely deteriorate over time, however, their TERS performance can be restored by reshaping the apex, through voltage pulsing. This was accomplished on the tips shown in Figure 3.4b and 3.4f, despite the large difference

between their initial cone radii of 18 nm and 80 nm. Indeed, the radii of curvature under operating conditions is not known, since additional sharpening cycles are done in situ, after the SEM images were taken. Nevertheless, it can be established that the prerequisite for reliably useful TER-sm tips is the surface finish achieved through ion-beam polishing.

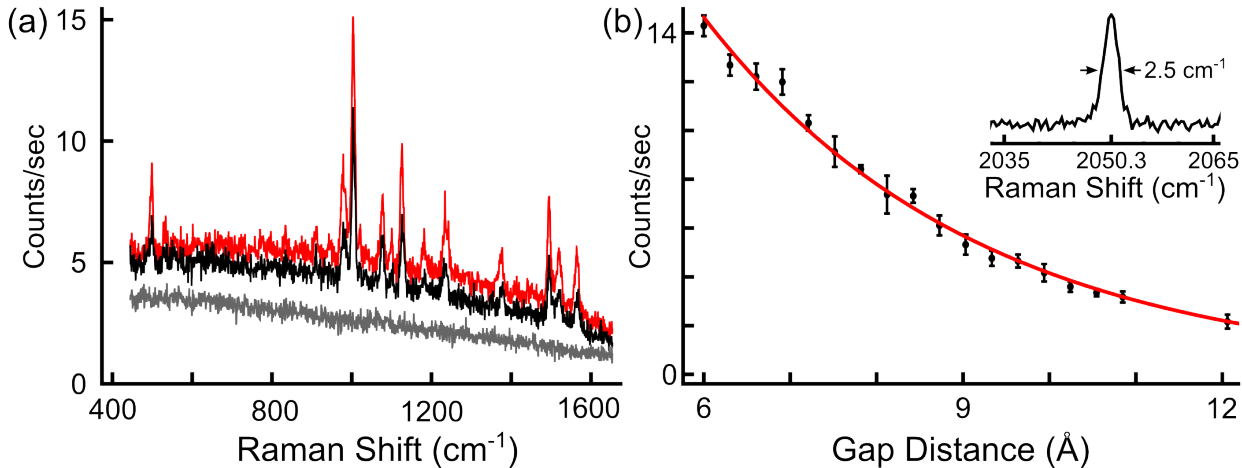


Figure 3.6: TERS spectra of BPE and CO and their gap dependence. (a) Evolution of Raman spectra upon gap distance change. Tunneling distance at 0.8 nA, 0.1 V, (60 s accumulation) gives rise to strong and sharp molecular peaks (red). The intensity decays as the tip is retracted by 1 Å (black, setpoint 0.1 nA, 0.1 V) and 17 nm (gray). (b) Exponential decay of Raman intensity of a single CO molecule terminating the tip apex. The decay length is 3.2 Å. Error bars are the standard deviation of the fitted intensity of six consecutively acquired spectra (10 s accumulation). Inset: Raman spectrum of a single CO molecule with an instrument-limited linewidth.

The operational performance of these tips is exemplified through the measurements highlighted in Figures 6 and 7. In Figure 3.6a, we show TERS of single 1,2-di(4-pyridyl)ethylene (BPE) molecules adsorbed on an atomically flat Au(111) surface, at 80 K. The excitation is at 634 nm, near the peak of the cavity mode (Fig. 3.5b) with an incident intensity of $< 5 \mu\text{W}/\mu\text{m}^2$. The sub-nanometric confinement of the local field is established by noting that the observed vibrational line intensities fall by $\sim 50\%$ upon 1 Å retraction of the tip; and the spectrum and the broad cavity mode disappears when the tip is retracted by 17 nm. BPE is a common nonresonant SERS reporter[29], which we have previously used in time-resolved and polarization selected Raman studies on nanodumbbells[26, 90, 120]. Although the observed lines in Figure 3.6a can be assigned to BPE, the line intensities are entirely different from

those of the ensemble and the commonly reported stationary SERS spectra. Consistent with the atomistic scale confinement of the field, the spectra are dominated by multipolar Raman driven by field gradients. In the second example, in Figure 3.6b, we show the spectrum of carbon monoxide attached to the tip apex, and the junction gap dependence of the TERS intensity. The measurements are carried out at 5 K, on Au(111), and the tip is terminated by a single CO molecule using established techniques[121]. The junction gap dependence of the TERS signal is exponential, with a decay length of 3.2 Å, as can be seen by the fit to the data in Figure 3.6b. CO is a poor Raman scatterer, with a gas phase differential scattering cross section of $d\sigma/d\omega = 3.3 \times 10^{-31} \text{ cm}^2/\text{sr}$. As such, if we assume the same cross section for the tip adsorbed CO, the observation of a single CO molecule implies a very large field enhancement, as previously pointed out[90]. Here, scattering rates as large as 10^3 s^{-1} is observed, which translates into an overall enhancement factor of 10^{13} , for a molecule aligned along the z-axis of the tip. The implied local field intensity is 0.1 V/nm.

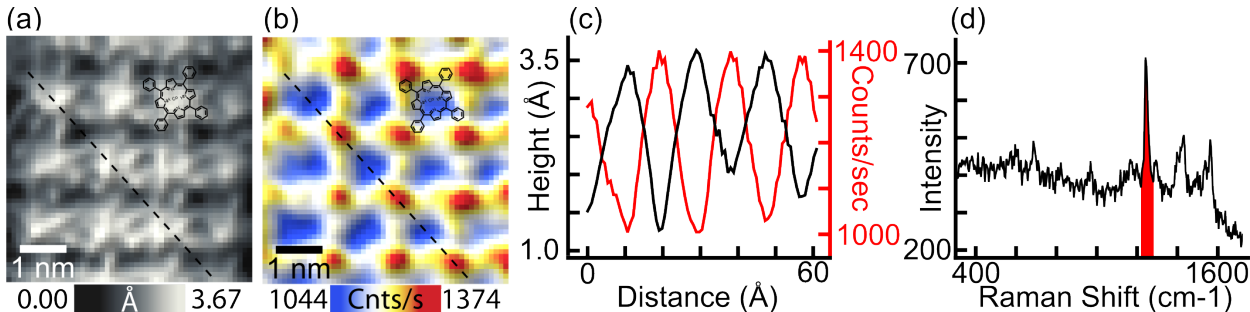


Figure 3.7: TERS mapping of CoTPP monolayer. (a) Constant current STM topography showing the CoTPP molecular lattice, with a structure of CoTPP overlaid as a reference (setpoint = 0.1 nA, 9.8 mV). (b) The simultaneously acquired TERS image integrated over the main vibrational peak at 1270 cm^{-1} (1244 to 1304 cm^{-1} , 1 s acquisition per pixel, $< 5 \mu\text{W}/\mu\text{m}^2$, 634 nm excitation). (c) The line profiles (dashed line in (a) and (b)) through the topography (black) and TERS map (red) showing the anticorrelation. (d) The integration window (red fill) and an example spectrum used to create the TERS image of CoTPP lattice on the Au(111) surface. The images have been lowpass filtered for clarity.

The lateral confinement of the cavity mode is illustrated through spectromicroscopy, by recording hyperspectral images on a 2D array of Co(II)-tetraphenylporphyrine (CoTPP) molecules prepared on Au(111). The constant current STM topography of the array is

presented in Figure 3.7a and the simultaneously recorded TER-sm image is presented in Figure 3.7b. The Raman spectrum of these flat molecules is strongly degraded, as illustrated in Figure 3.7d. The dominant line at 1280 cm^{-1} is a field gradient driven mode, localized on the phenyl groups. The hyperspectral images consist of recording complete Raman spectra on each 1 \AA by 1 \AA pixel, with an acquisition time of 1 s (incident intensity of $\sim 5\text{ }\mu\text{W}/\mu\text{m}^2$, at 634 nm). The TER-sm image in Figure 3.7b is a mode specific map of the integrated intensity from 1244 to 1304 cm^{-1} (Fig. 3.7d). The TER-sm resolution is nearly identical to that of the STM, as clarified by the line cuts taken from the two images in Figure 3.7c. Note that the Raman intensity is anticorrelated with the STM topography. As we have reported previously, the in-plane vibrational spectra of molecules that lie flat on the gold surface are completely quenched, while the field gradient driven modes of the phenyl groups are observed, and are brightest when the tip is placed between molecules. This, in part, can be attributed to lift-off and tilting of the molecules as the tip approaches, recently demonstrated in a related system. A more detailed analysis of the selection rules in this near field spectroscopy is deferred. Here, we suffice by noting the salient features of TER-sm governed by extreme confinement of light, and note that in this case the confinement volume of $3.2^3 \approx 30\text{ \AA}^3$ is more characteristic of tunneling electrons, rather than photons, as evidenced by the comparable spatial resolution of the STM and TER-sm maps.

3.3 Conclusion

TER-sm opens up a new vista in spectromicroscopy. However, its implementation rests upon the fabrication of tips with reliable performance. FDSS processing of electrochemically etched and electropolished silver tips fulfills this requirement. The process self-sharpens, smooths and cleans silver tips, and demonstrably limits the far field scattering to the sole nanocavity mode of the atomically terminated tip and substrate. Reliably generated tips greatly accelerate discovery of the relevant TERS science, as illustrated by the implemen-

tations used to validate the performance of the processed tips. We show that finely tuned tips can lead to dramatic field enhancement by confining optical fields to picocavities, with volume as small as $\sim 30 \text{ \AA}^3$. A direct outcome of this extreme confinement is that TERS is a near-field effect, where multipolar Raman scattering driven by field gradients sculpted by the atomic morphology of the nanojunction dictates the observable spectra. The contrast inversion between the STM and TER-sm images seen in Figure 3.7 illustrates one aspect of this consideration. Another important consideration is that at the length scales of relevance are in the quantum limit of plasmonics, and consistent with this, in all presented examples the TERS intensity scales exponentially with the junction gap, implying that the scattering is governed by the tunneling junction plasmons. The confinement of the optical field can be equally well regarded as the confinement of the photo-tunneling electrons.

Chapter 4

Tip-enhanced Raman spectromicroscopy: cavity photons, electrons and a molecule

4.1 Introduction

By now, it is well established that plasmonic nanojunctions allow vibrational spectroscopy with single molecule sensitivity through the surface enhanced Raman scattering (SERS) effect discovered by Van Duyne[109]. In the four decades intervening the discovery, there has been an explosion of developments and diverse applications of SERS[122]. Nevertheless, the fundamentals of the effect remain an active area of research. While enhanced local fields through confinement of light at nanojunctions is an established essential ingredient, there is now mounting evidence that atomistic detail in junction morphology matter in defining the local fields that determine the signal ultimately broadcast by the nantenna. This was clearly demonstrated by the observation of multipolar Raman scattering at the fusing junction of the prototypical nanodumbbell antenna, consisting of a silver nanosphere dimer[90]. That study also underscored the inherent experimental challenge that the several atom-wide

gaps required to reach single molecule sensitivity evolve under irradiation. Transitioning to measurements in the more controllable junction of a scanning tunneling microscope via tip-enhanced Raman scattering (TERS) has been an important development[123] with significant advances made toward Raman spectromicroscopy[30]. A most visible contribution in this field was the demonstration of TERS with submolecular spatial resolution[33] - an effect that was not quite anticipated by the standard models of SERS. The challenge has been addressed by advancing theories to treat quantum and atomistic plasmonics[124], and the recognition of the role nano- or pico-cavities may play[35] by borrowing from the field of cavity quantum electrodynamics[125]. Here we demonstrate that like STM, the Å-scale spatial resolution of TERS is derived from its exponential dependence on tip-molecule separation. Consistent with our prior suggestion that in this limit TERS may be regarded as coherent photo-electro-luminescence,[1] we identify phototunneling as an inseparable part of the inelastic light scattering process. Rather than purely optical, the cavities act as resonators of tunneling charge transfer plasmons, which in effect trap photons. The strong coupling between cavity modes and molecular states is manifested by the appearance of vibrational overtones and combination bands despite the absence of molecular electronic resonances. The observations presented are ingredients that a complete theory of TERS must be able to address. Experimentally, the art of tip design with control and maintenance of atomistic detail in morphology must be mastered (see Chapter 3) to develop TERS into a reliable tool of spectro-microscopy with submolecular spatial resolution. This is underscored by the transient nature of the bright cavities that we report.

The experiments are carried out at the STM junction of a silver tip and an atomically flat Au(111) substrate, principally using bipyridyl ethylene (BPE) as the Raman reporter. The molecule is selected since its surface enhanced Raman and hyper-Raman[126–128], stimulated Raman[129], and coherent anti-Stokes Raman spectra[130] have been previously characterized with CW and short pulse lasers. The bulk of the measurements is carried out at 80 K, at a temperature where BPE remains mobile in a 2D gas state over the gold surface. Although,

individual BPE molecules trap at the illuminated STM junction, and allow recording of their TERS spectra, they cannot be imaged due to their mobility. For imaging purposes, be it through TERS or STM, an attempt is made to anchor BPE by ligating it to co-adsorbed, flat cobalt(II)-tetraphenylporphyrin (CoTPP) molecules. Ligation projects the molecule along the surface normal, along the required z-field of the plasmonic antenna formed by the silver tip and its image in the atomically flat gold mirror. Anchored molecules are used to demonstrate vibrational spectroscopy with submolecular spatial resolution. Although CoTPP is intended as a passive pedestal, it can be optically imaged through cavity enhanced electronic luminescence, as previously reported in a closely related study[131]. The silence of vibrational TERS from cold CoTPP pedestals, with otherwise reported TERS activity at room temperature[132], and the multipolar vibrational Raman spectra of BPE illustrate the strong near-field selection rules.

4.2 Methods

The instrumentation used in the current TERS studies has been described previously (see Chapter 2). It consists of a cryogenic, ultrahigh vacuum scanning tunneling microscope equipped with a parabolic collector mounted on piezoelectric stages. The focus of the parabola can be precisely centered on the tip apex by imaging electroluminescence and modeling the image obtained through the train of optical elements (see Appendix A). The principle advance that allows us to obtain reproducible TERS results with high S:N is the processing of the silver tips. After electrochemical etching with an automated setup that has been described, we use in-situ Ar-ion bombardment to further self-sharpen and polish the tip. A detailed description of the procedure can be found in Chapter 3.

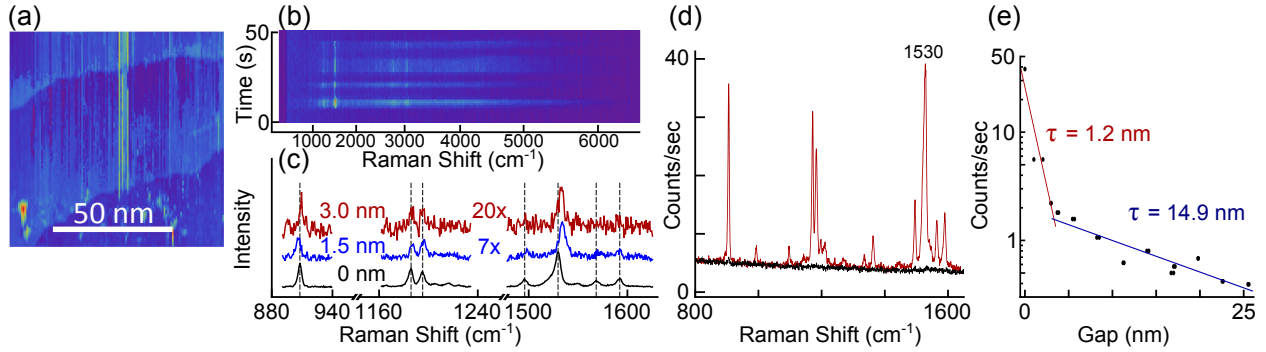


Figure 4.1: TERS over BPE trapped in Junction. (a) STM topographic image of BPE on CoTPP coated Au(111) surface. Streaks are indicative of the tip trapping a molecule. (b) Fluctuations in the TERS intensity. (c) The molecular lines shift slightly as the tip-sample gap is increased (Black = engaged, Blue = retracted 1.5 ± 0.5 nm, Red = retracted 3 nm). (d) Full spectrum with tip engaged (red) and retracted 17 nm (black). (e) Retraction curve with Log-Linear axes showing bi-exponential decay of the Raman signal (monitoring the 1530 cm^{-1} line).

4.3 TERS of BPE trapped at the STM junction

A typical STM area scan of Au(111) dosed with BPE is shown in Figure 4.1a. The streaky image is characteristic of a surface covered with a physisorbed, low-density 2D gas. The occasional bright stripes are due to molecules dragged by the tip. Raman scattering monitored with a stationary tip shows fluctuations, as in Fig. 4.1b, with transient bright vibrational spectra that appear over the broad continuum when diffusing molecules pass through the junction. Occasionally, molecules trap at the junction, or they can be coerced to trap by manipulating the junction gap and bias. The spectrum of such a molecule is shown in Fig. 4.1d. The line profiles are Gaussian, near the instrument resolution limit of $\text{FWHM} \sim 4\text{--}6 \text{ cm}^{-1}$. A stack plot of the spectra recorded as the tip is retracted is shown in Fig. 4.1c. The spectra remain stationary during the measurement, with minor variations in relative line intensities, and small line shifts of order 2 cm^{-1} that are consistent with Stark tuning under the applied DC bias. Remarkably, the intensity of the vibrational lines decay exponentially with the junction gap. As shown in Fig. 4.1e, the gap dependence of the 1530 cm^{-1} peak fits a double exponential, with decay constants of 1.2 nm and 14.9 nm respectively. The slow decay is observable because of the large dynamical range; otherwise, the initial decay

constitutes 4% of the total signal. Attempts at imaging the molecule on bare gold fail. Upon lateral translation of the tip by ~ 1 nm, the molecule is usually lost.

4.3.1 Nanocavity Resonances

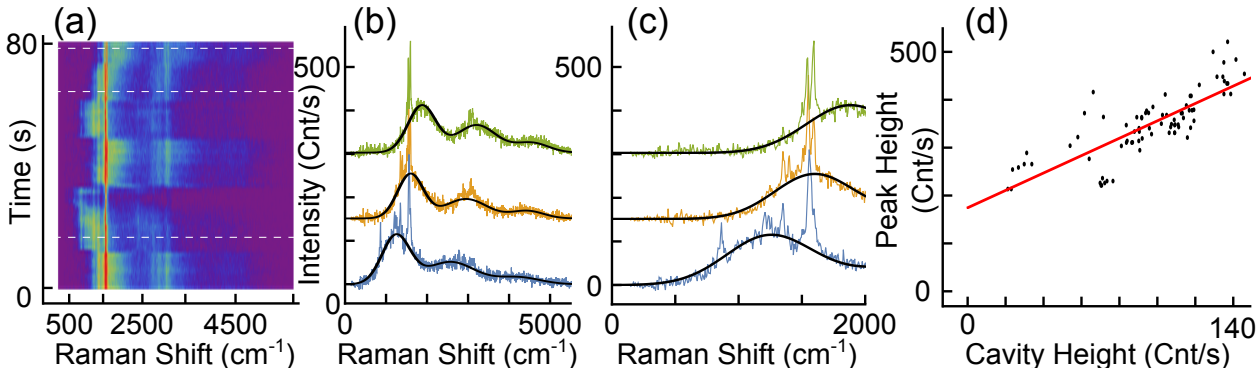


Figure 4.2: Spectra of Nanocavity Resonances and Molecules. (a) Image plot of spectra over the course of 80 s showing the shifting cavity resonance. (b) Stack of 3 spectra from the image plot (white dashed cuts) show the progression of resonances. (c) Zoom-in on the molecular features of (b) shows the cavity resonance seemingly enhancing the molecular lines. (d) The 1553 cm^{-1} molecular peak intensity is correlated with the cavity intensity at 1553 cm^{-1} .

TERS spectra are invariably accompanied by a continuum that can be assigned to (1) electronic Raman scattering on the metal and (2) a modulated background due to scattering on the local junction plasmon. The latter can be readily assigned to junction cavity resonances by inspection of a time series of fluctuating spectra (Raman trajectories) as molecules move through the illuminated junction. A representative trajectory, captured at a frame rate of 1 s^{-1} , is presented in Fig. 4.2 as a 2D image plot (Fig. 4.2a) and as a stack plot of selected spectra (Fig. 4.2b). The intensities of the vibrational lines fluctuate along with the broad cavity resonances. Previously invisible vibrational lines appear when the cavity resonance tunes into its vicinity (Figure 4.2c, blue spectrum). The two signals are directly correlated as illustrated in Fig. 4.2c, in which we plot the line intensity at 1553 cm^{-1} versus the background intensity at the same frequency. Future DFT simulations could help understand the state and/or orientation of the molecule that produces these spectra and the extent to

which local fields, specifically field gradients, impact the spectrum. Cavity resonances can be expected to be determined by geometry and dispersion of the confined dielectric. It is clear that in these nanometric cavities, the resonances are determined by atomic scale variation in geometry, be it of the tip apex or the motion of the confined molecule.

4.4 Imaging stationary CoTPP molecules

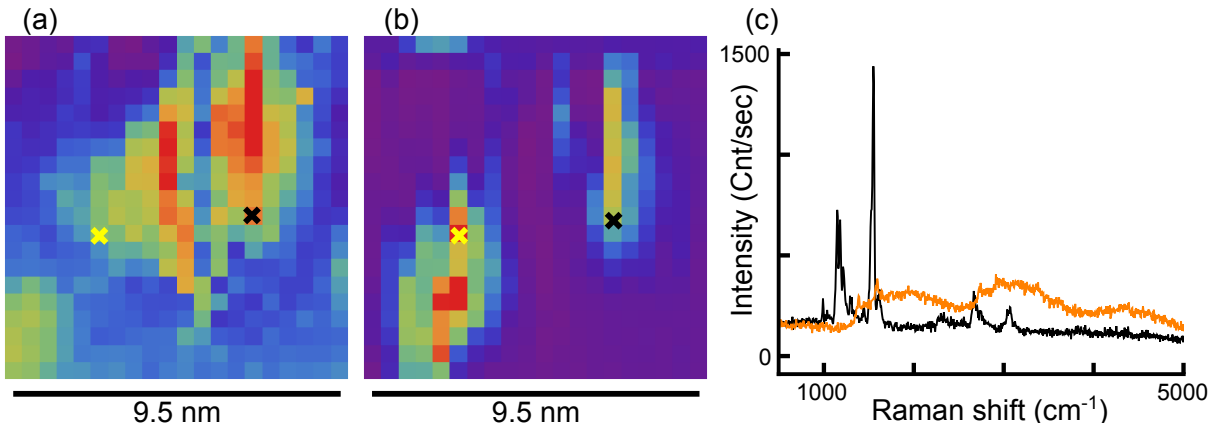


Figure 4.3: TERS Map of Au(111) surface coated with CoTPP and BPE. (a) Topography image (setpoint = +1.0 V, 20 pA) of the surface. (b) Simultaneously acquired TERS map with $5 \mu\text{W}/\mu\text{m}^2$ 532 nm excitation, 1 s accumulation per pixel. (c) Surface spectra taken from the positions marked with X, showing the ability to distinguish surface structures by their Raman spectrum.

Consistent with the picture of bright cavities, the co-adsorbed CoTPP molecules can be imaged through the broad sequence of resonances shown in Fig. 4.3b and c, which can be assigned to Q-band transitions as previously recognized in the closely related measurements on Ag(111)[133]. The simultaneously recorded STM and optical image of such a molecule is shown in Figure 4.2a and b, respectively. The broad signal in the lower left side of the image (yellow X in Fig. 4.3b and orange spectrum in Fig. 4.3c) is that of enhanced luminescence after vibrational relaxation composed of a vibronic sequence Q_{00}, Q_{01}, Q_{02} , separated by $\sim 1200 \text{ cm}^{-1}$, over a formally forbidden transition. To be visible, the radiation rate must be dramatically enhanced through the Purcell effect to overcome coupling and quenching via e-h pair creation in the metal, on a time scale of 10^{-12} s. Based on the radiative rate of

the transition (10^6 s^{-1}) extracted from its absorption spectrum and from the enhancement through the Purcell factor:

$$F = \frac{3}{4\pi^2} \left(\frac{\lambda}{n} \right)^3 \frac{Q}{V} = 10^6 \quad (4.1)$$

where $Q = \omega/\text{FWHM}=15$ is the quality factor of the cavity, a cavity volume V of 500 nm^3 can be estimated. This implies a cavity volume six orders of magnitude smaller than that of vacuum (λ^3). For a cylindrical volume ($V = \pi r^2 h$) and assuming a height for the junction gap ($h = 1 \text{ nm}$), a cavity radius of $r = 12 \text{ nm}$ can be deduced. This can be associated with the lateral confinement length of photons trapped in junction cavity. While an estimate, the effect allows the appreciation of the role cavities play in modifying the density of the vacuum and contributing to the enhancement effect in TERS.

4.5 Overtones and combination bands

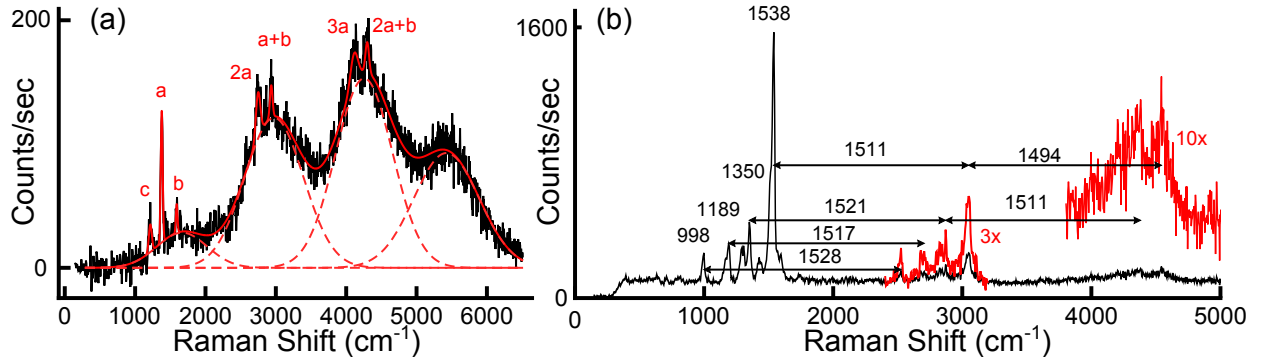


Figure 4.4: Cavity-enhanced overtones and combination bands. (a) Two orders of overtones and combinations of the main mode a (1378 cm^{-1}) with a secondary mode b (1591 cm^{-1}) appear to be enhanced by the broad cavity resonances (red dashes). Combinations of mode c (1216 cm^{-1}) fall outside the cavity's spectral enhancement range. The spectrum is fit with a sum of 11 Gaussians (red solid). (b) Another spectrum showing two orders of overtones and combinations. This time, the 1538 cm^{-1} mode drives the process. The spacings between the overtones/combinations and their fundamental are shown to highlight the anharmonicity in the potentials.

Remarkably, overtones and combination bands are observed to track the appearance of a progression in cavity resonances. Examples are shown in Figure 4.4. In Figure 4.4a,

combination lines of two of the observed fundamentals appear above the rolling background. All of the overtones and combinations involve the strongest line at 1378 cm^{-1} , marked *a*. Combinations and overtones that lack this mode are too weak to be observed. And interestingly, despite *c* and *b* being of equivalent intensity, the *a* + *c* combination is absent (or too weak to assign with certainty) while *a* + *b* and even $2a + b$ are quite prominent. This missing combination would indeed fall further out of the “window” of the 4 observed cavity resonances (red dashes) than that of the observed combinations. This is, again, evidence that the tip-sample geometry-induced cavity resonances play a fundamental role in enhancing the excitation and/or scattering of specific vibrations. In Figure 4.4b three copies of the fundamental spectrum can be seen to arise as combinations of the intense line at 1538 cm^{-1} with all other modes. The anharmonicity of the fundamental’s potential as well as that of the combination potentials vary, providing a solid spectroscopic measurement of the molecule’s potential surfaces. Neither overtones nor combinations among the weaker lines are apparent in the first overtone region, where the S:N is sufficient to make such assignments. The appearance of overtones and combination bands is rare. They are associated with bright but delicate junction cavities, which do not survive tip reshaping through field emission. The observation of overtones of BPE is remarkable in view of the fact that the free molecule does not have an electronic resonance low enough in energy to be excited by 532 nm excitation. Otherwise, real evolution on an excited electronic state could generate overtones. Because of this, the observed lines might likely originate from CoTPP, with the motion and interaction of BPE potentially playing a role. A similar kind of “activation” of the silent surface CoTPP molecules is observed with the addition of mobile carbon monoxide molecules (see Chapter 5). Whether through electronic or mechanical anharmonicity, the observable overtone and combination bands would be determined by the molecular vibronic Hamiltonian. In Fig. 4.4, we see variations in the observable bands, driven by cavity resonances. The data suggests that the spectra belong to the dressed states of coupled molecule cavity modes, where overtones would be associated with the ladder of the Jaynes Cummings Hamiltonian.[134]

4.6 Conclusion

The intriguing near-field spectra observed through TERS, admittedly, contains more information about the molecule and its local environment than has been discussed in this chapter and that is currently understood. The molecular spectrum's sharp spatial-sensitivity and correlation with resonances of the tip-sample cavity characterizes an experimental system that demands further investigation. The ability to control the cavity resonance seems to be the key to enhancing and localizing the TERS signal. The complex spectra, in part, is due to the multi-component (BPE and CoTPP) sample. In the next chapter, this complication will be reduced slightly but investigating a surface composed of just one polyatomic molecule, CoTPP.

Chapter 5

Sub-molecular Spatially-Resolved TERS of CoTPP at High and Low Temperature

5.1 Introduction

To the extent that molecules can be regarded as networks of balls (atoms) and springs (bonds), they can be characterized by the frequencies of their internal motions. This is the realm of vibrational spectroscopy, which remains one of chemists' sharpest tools for fingerprinting molecules and characterizing their inner workings. As such, the ability to record vibrational spectra of individual molecules, by sounding off individual atoms within molecules, can be regarded as the chemists' ultimate microscope - the chemiscope for short. The task is challenging for several reasons. The universally applicable method for recording vibrational spectra is based on the Raman effect, which involves the excitation of molecules with light and recording the spectrum of re-radiation by the vibrating molecule. However, the effect is feeble. To obtain a useful level of signal of 10^3 photons/s, it is necessary to irradiate a molecule at intensities of terrawatt/cm². Moreover, photons are much larger

than atoms. The Abbe principle recognizes that the size of the photon limits the focusing capability of the optical microscope to a spot of $\lambda/2 \approx 250$ nm, where λ is the wavelength of light. To reach the 0.1 nm size scale of the atom, photons must be squeezed down to a thousandth of their size.

These challenges are met by resorting to plasmonic nanoantennas[135]. The prototypical nanoantenna consisted of a pair of nanospheres separated by ~ 1 nm gap, a nanoscale analog of the antenna used by Hertz[136]. By coupling light to surface charge oscillations (plasmons) of the dipolar nanoantenna, electromagnetic fields are effectively focused at the nanojunction. The large field enhancement due to confinement is sufficient to record Raman spectra of individual molecules[49, 137, 45], through the surface enhanced Raman scattering (SERS) effect[109], Although there has been an explosion of developments and applications of SERS[138], the fundamentals of the effect remain the subject of active research. It is now recognized that the local fields and plasmonic optical response that drive the SERS effect are governed by the atomistic detail of the nanoscale junction[139, 35]. To image the internal motions of individual molecules, the junction morphology must be tuned at the atomic level. However, the characterization and control of nanojunctions with atomistic precision remains a challenge. Resorting to the more controllable junction of a scanning tunneling microscope (STM), under the rubric of Tip-enhanced Raman spectroscopy (TERS)[140], has accelerated discovery and applications in TER-spectromicroscopy (TER-sm)[141, 142]. Noteworthy among these was the realization of TERS with submolecular spatial resolution[33] - an effect that was not anticipated by the then standard classical models of tip plasmons[143]. In the sub-nanometer junction gaps necessary to reach single molecule sensitivity, quantum effects cannot be dismissed[144, 145]. The dynamics of optically driven electron densities, which can tunnel across junctions, must be explicitly treated to describe the relevant local fields[146]. Atomistic electrodynamic simulation[37], coupled with quantum chemical treatments of the molecule and the scattering process[36], are necessary for reliable descriptions. And given the strong fields, field and matter states can become entangled[147, 125]. The

quantum electrodynamics of plasmonic cavities, which confine photons, electrons and the molecule under study, provides a frontier in science that must be conquered along the way to develop the chemiscope.

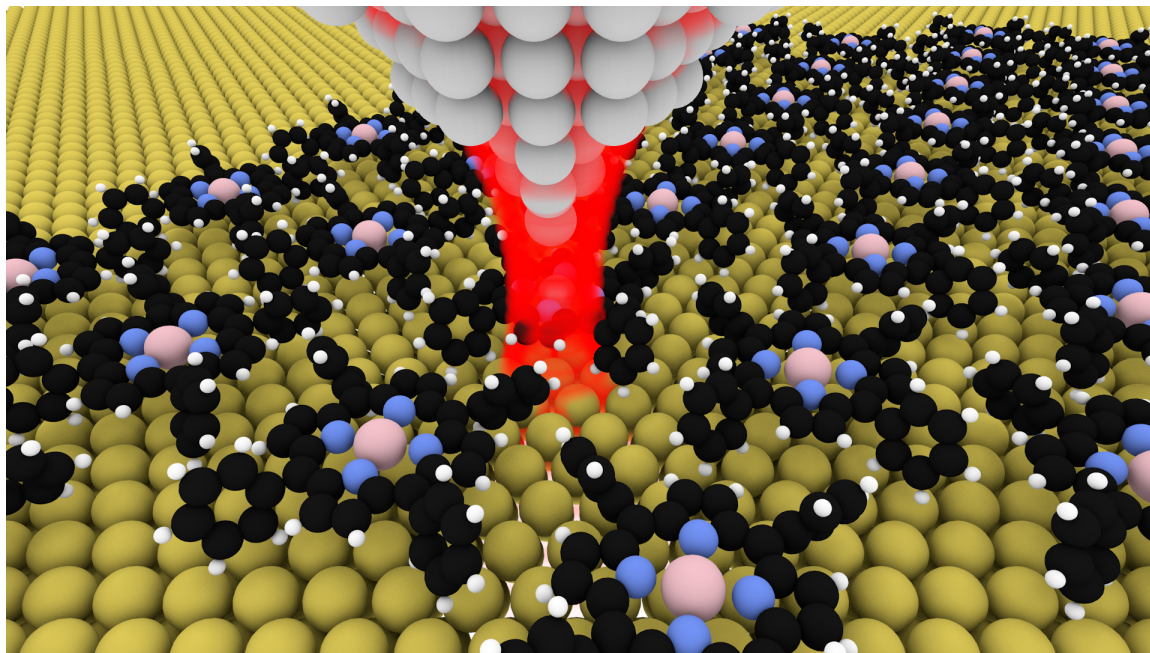


Figure 5.1: Render of TERS imaging of a CoTPP monolayer on Au(111) . The tip-sample junction is irradiated with 634 nm light, exciting a cavity mode (red) with a sub-nm effective focal waist. With the signal localized to this small volume, sub-molecular structural information is obtained by rastering the tip over the sample surface.

Here, as a significant milestone, TER-sm is presented with submolecular spatial resolution at room temperature. By mapping fits to spectral lines at 80 K, super-resolved TER-sm reveals rich molecular information content and higher spatial detail than STM. The spectra are thermally activated and the molecule is intimately involved in defining the junction cavity, with an effective focal waist $< 5 \text{ \AA}$ and an exponentially steep, temperature dependent focal length of $< 5 \text{ \AA}$ at 5 K. The cavity mode intensity directly follows the exponential gap dependence of the STM tunneling current, as such appears to be determined by tunneling plasmons. Single molecules are used to probe the cavity sculpted field and its gradients. The measurements are carried out at the STM junction of a silver tip and an atomically flat Au(111) substrate, using cobalt(II)-tetraphenylporphyrin (CoTPP) as the Raman reporter.

The nearly planar high symmetry (D_{4h}) molecule has been previously investigated through both STM[148] and TERS[149]. It allows the outlining of the salient features and promise of TER-sm along with previously overlooked mechanistic details of the process.

5.2 Experimental

The instrumentation used in the current studies has been described previously[2]. As used in the previous chapters, a cryogenic, ultrahigh vacuum scanning tunneling microscope equipped with a parabolic collector mounted on a piezoelectric stack is used in these investigations. The focus of the parabola can be precisely centered on the tip apex by imaging electroluminescence (EL) and modeling the image obtained through the train of optical elements (see Appendix A). The excitation is at 45° incidence, focused with an F.L. = 7.9 cm lens to an estimated spot size of ~ 10 μm . The Raman spectra are recorded using continuous wave diode lasers, at 532 nm or 634 nm, with a typical intensity of 5 $\mu\text{W}/\mu\text{m}^2$ delivered at the sample. The tip preparation described in Chapter 3 has enabled reproducible TERS results. The tip shape matters on two scales: the gross geometry associated with the roles of the tip as an antenna that couples far field radiation into the apex, and the sub-nm detail in the morphology of the apex, which acts as the cavity for confining photons. The desirable gross structure is a silver needle with $\sim 30^\circ$ cone angle, which is known to lead to superfocusing[150, 151]. It is nevertheless essential that the surface of the cone be smooth on the nm-scale, to eliminate asperities that lead to radiation damping or to hot spots that generate SERS outside the junction[138]. To this end, after electrochemical etching with an automated setup that has been described[83], ex-situ Ar-ion bombardment is used to sharpen and polish the tip. A good indicator of the formation of junction cavities is the observation of significant gap dependent shift in the EL spectra[119]. This criterion is used to establish the TERS utility of a tip when reshaped through field emission. The fine tuning of the cavity is less direct. While monitoring the electronic Raman scattering continuum of the junction,

the bias is raised to 3 V and the current is increased to 10 nA. Evolution of the background spectrum under these conditions is accompanied by broad flashes, indicative of structural changes at the apex. Either the broad resonance of the cavity window is moved toward the Stokes window or the color of the laser is chosen to match it. In the measurements reported here, the excitation wavelength was changed from the initial 532 nm to 634 nm to approach the observed cavity window. Despite the Q-band electronic resonance of CoTPP at 530 nm, the vibrational TERS appears upon matching the Stokes window with the cavity resonance by excitation at 634 nm.

5.3 TER-sm

At room temperature, CoTPP forms 2D islands on gold, as seen in the simultaneously recorded STM and hyperspectral TERS images of Figure 5.2. The latter consists of recording complete spectra on each x,y-grid point with a pixel size of $1 \times 1 \text{ \AA}$ and spectral acquisition time of 1 s/pixel. The TERS spectrum is shown in Figure 5.2d. It completely disappears upon 1 nm retraction of the tip, and shows exponential gap dependence with a decay constant of 10 \AA . The scatter in the data is real. It can be ascribed to motion of the molecule, both thermal and due to the Hamaker force between tip and molecule. The spectrum consists of three distinct components: the exponentially decaying background of electronic Raman scattering on the metal, a flattop cavity window with cut-off at 1600 cm^{-1} , and a set of molecular vibrational lines within the window. The spatial maps of the individual vibrational lines, and the cavity window void of lines, are presented in Figure 5.2c. Inspection of the images is sufficient to infer that the spatial resolution in the TERS images is on the same scale as in the STM. However, TER-sm contains a hyper-spectral component that can be decomposed into a set of eight mode specific vibrational images. The observed vibrations are normal modes that are principally localized in the phenyl rings.[152] Nevertheless, there is clear variation in their spatial maps. The map of the C-C stretching mode at 1606 cm^{-1}

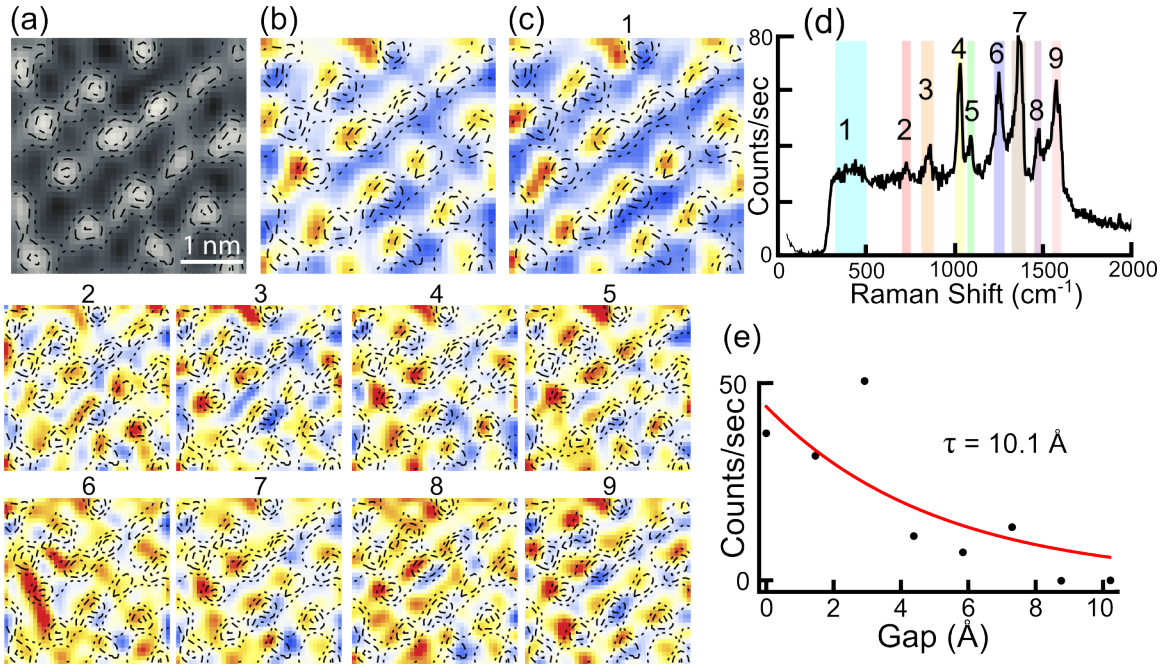


Figure 5.2: Vibrational mode maps at 300 K. (a) Topographic image ($39 \times 39 \text{ \AA}$) taken at 10 pA, +0.15 V. (b) Simultaneously taken Raman imaging integrated over a full vibrational window ($300\text{-}1700 \text{ cm}^{-1}$). (c) Raman mapping of the cavity mode window ($320\text{-}500 \text{ cm}^{-1}$). (d) Raman spectrum of the CoTPP monolayer dissected into normal mode windows. The labeled windows are used to make the numbered Raman maps in the lower left panel. (e) Exponential decay of Raman intensity integrated over a window ($700\text{-}1650 \text{ cm}^{-1}$). 8 vibrational maps at the bottom panel are produced by subtracting the cavity-background and integrating individual vibrational peaks. Out of 9 mode-specific Raman images, mode 6 and 9 images are anti-correlated with the topography represented by contours. This figure is adapted from a figure produced by Dr. Joonhee Lee.

is generally anti-correlated with the location of the molecules, while the mainly phenyl C-H rocking vibration at 1496 cm^{-1} is closely correlated, as is the C-H wagging motion at 877 cm^{-1} . The latter is mainly an IR active mode, which gains Raman intensity through field-gradients in near field scattering[153]. There clearly is greater molecule-to-molecule variation in the TERS maps than in the STM topography, information that could potentially be unraveled. Remarkably, the cavity mode maps out the molecules with contrast that tracks the STM topography with high fidelity (Fig. 5.2a,c).

The cavity images of the molecules are diagonally displaced by $\sim 5 \text{ \AA}$ relative to that of the STM. The latter is formed by electron tunneling from the terminal Ag atom of the

tip with an exponential gap dependent probability, $\langle \phi(z) | \phi(z_0) \rangle = \exp[-2\kappa(z - z_0)]$ where $\kappa = 1.2 \text{ \AA}^{-1}$. It appears that the cavity responsible for the optical imaging is displaced by ~ 1 Ag atom from the terminal tip atom, along the direction of incidence of the laser. The displacement provides a direct measure of the lateral confinement of the optical focal plane, to an area of $< 25 \text{ \AA}^2$. Taking the exponential decay length of the TERS signal intensity as the cavity length, a confinement volume of 250 \AA^3 can be extracted. It is tempting, though not sensible to assign this volume to confinement of a photon, since the local field that would arise from one such photon, $E = \sqrt{\hbar\omega/2\epsilon_0V} = 0.85 \text{ V/\AA}$, would ionize any molecule. The local field can be estimated from the observed scattered intensity and the Raman cross section of the molecule to be hundred times smaller, $\sim 5 \times 10^{-3} \text{ V/\AA}$. Thus, the associated photons that define the local field are extended over the tip cone and its image in the gold mirror. The exponential gap dependence of the cavity mode intensity and its 10 \AA range, characteristic to electron tunneling through the molecule, suggests a cavity determined by the confinement of tunneling plasmons.

Cooling the tip and sample down to 80 K greatly improves the imaging ability of the STM thanks to the stronger anchoring of the molecules to the surface (Figure 5.3a). Unfortunately, the TERS signal from these molecules is completely absent. If the Raman scattering was electronically resonant via the Q-band of CoTPP then cancellation of the in-plane transition dipole via its image in the gold mirror could explain the total silence. However, the excitation wavelength at 634 nm is removed from the Q \leftarrow X transition of CoTPP, which occurs at 530 nm. Given that TPP has 34 out-of-plane vibrations, 8 of which are Raman active, the disappearance of the vibrational spectrum upon cooling cannot be trivially rationalized. The silent flat surface molecules appear to be at a nodal plane of the tunneling plasmon cavity. This cavity is very delicate. The introduction of a disrupting agent, in the form of a 2D molecular lattice gas, can spoil the cavity, eliminating the silencing nodal plane. The vibrational spectrum of an individual molecule can be activated by tilting or lifting it with the tip (see below); yet the cold molecule on the substrate-side remains silent. The molecule

appears to be at the nodal plane of the tunneling plasmon, in a perfect cavity. This picture is supported by the activation of vibrational spectra upon introducing a 2D lattice gas of mobile molecules, ostensibly, by spoiling the cavity.

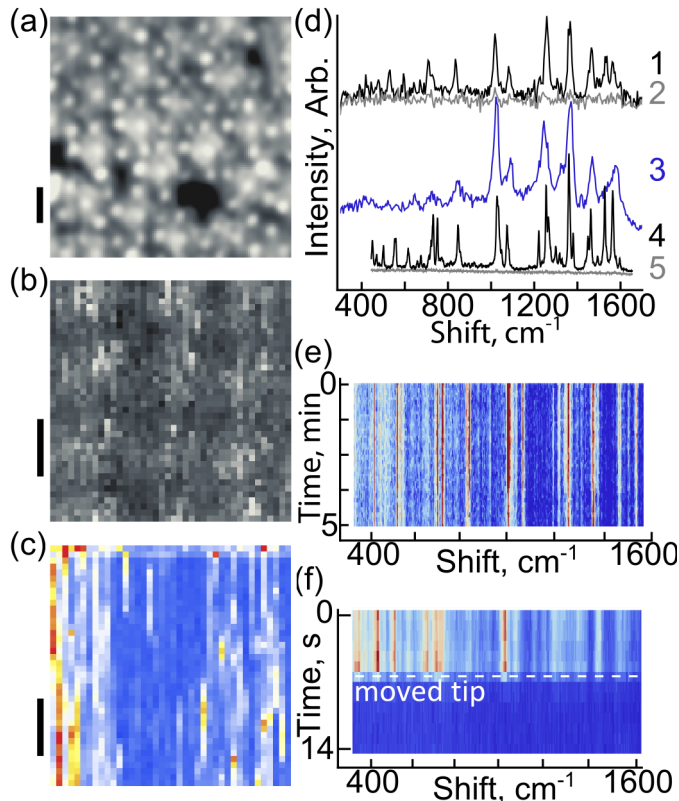


Figure 5.3: CO acts as a cavity spoiler. (a) Topography of CoTPP monolayer lattice at 80 K with resolved phenyl groups. Scale bar = 1 nm. (b) Degraded topography of CoTPP due to CO lattice gas on the surface. Scale bar = 1 nm. (c) Simultaneously taken Raman map with flashes as CO molecules pass. Each pixel is the integrated Raman intensity from 600 to 1650 cm^{-1} . Scale bar = 1 nm. (d) Extracted spectra from the map (c), 1 and 2, highlight these flashes. Acquisition time is 1 s. Spectra 4 and 5 are high resolution spectra taken at 80 K with a stationary tip engaged on the CoTTP surface and retracted 5 Å, respectively (10 s integration.). The peaks in both spectra 1 and 4 agree with the spectrum acquired at room temperature, 3 (1 s). (e) Stable spectra while the tip is stationary. (f) Immediate disappearance of Raman signal upon initiating a scan.

Upon introducing CO molecules, which are mobile on gold at 80 K but eventually bind to CoTPP[148], complete vibrational spectra of CoTPP emerge. This is illustrated in the simultaneously recorded images of Figure 5.3b,c. The STM image is now streaky, due to the CO gas. And the simultaneously recorded TERS data show no correlation with the

STM image or any spatial features. However, the bright streaks that appear sporadically during the scan carry the sharp and rather complete vibrational spectra of the cold molecule, as illustrated in Figure 5.3d. The CO activated spectra are stable when probed with a stationary tip. This is illustrated by the TERS trajectory presented in Fig. 5.3e, in which instrument resolution limited line widths of $\text{FWHM} = 6.7 \text{ cm}^{-1}$ can be seen, with fluctuations in center frequency of order 1 cm^{-1} . The large dynamic range of the spectra identifies over 30 vibrational lines of the molecule. Their direct lineage with the room temperature spectra is clarified by the overlay in Figure 5.3d, and their single molecule TERS nature is established by the retraction dependence. The spectrum disappears upon 5.7 \AA retraction of the tip (see traces in Figure 5.3d). The signal falls exponentially with a decay length of $\sim 5 \text{ \AA}$, significantly shorter than what was seen at room temperature. The spectra are remarkable by the absence of a background, which is characteristic of molecules lifted by the tip. Here, the effect is realized by the intercalated CO molecules. However, at 80 K, CO is only loosely attached to the junction since the activated spectra are lost as soon as the tip is scanned, as illustrated in the TERS trajectory of Figure 5.3f. Despite the high S:N of the activated spectra, we do not observe the characteristic CO vibrational line, which admittedly lies outside the cavity window. Here, it appears to act as a cavity spoiler that replaces the thermal noise in the ambient measurements.

TERS microscopy, albeit with a degraded vibrational spectrum, becomes possible once the CO gas subsides, due to uptake by CoTPP[148]. The simultaneously recorded STM and TERS images are shown in Figure 5.4a,b along with the degraded vibrational spectrum in Figure 5.4c (zoom-in of the spectrum is also shown in Fig. 3.7d). Remarkably, the contrast in the TERS image is inverted. The TERS intensity is larger when the tip traces the metal area between molecules. Despite the weak signal, spatially well-resolved images can be obtained by mapping out the Gaussian fit to the vibrational line at 1270 cm^{-1} , with an advantage analogous to that of super-resolution in fluorescence microscopy[154]. A given vibrational line now generates two maps, one of line shift and one of intensity, as shown for the smaller

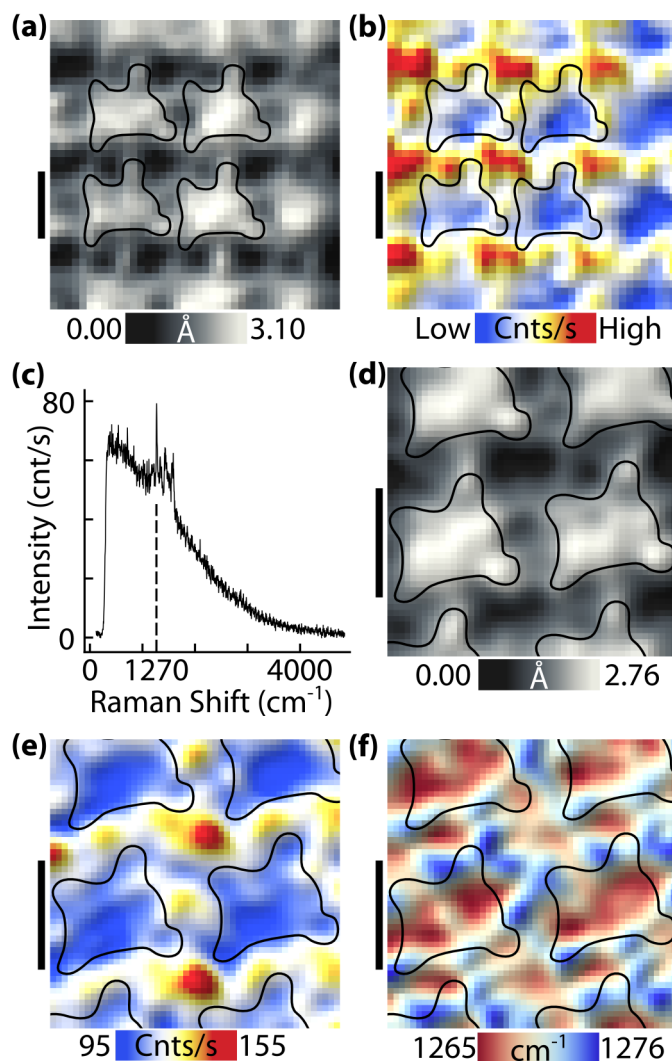


Figure 5.4: Submolecular chemical information revealed by TER-sm. The topography of a CoTPP lattice at 80 K (a) is anti-correlated with Raman image produced by integrating 1270 cm^{-1} mode intensity (b). (0.1 nA, 9.8 mV, 634 nm laser at $5 \mu\text{W}/\mu\text{m}^2$, 1 sec accumulation per pixel). (c) Degraded TERS spectrum extracted from the Raman map. (d) Zoomed-in topography of area (a). (e-f) Super-resolution TER-sm. The 1270 cm^{-1} mode is fitted by a Gaussian peak and the extracted intensity and frequency shift are mapped in (e) and (f), respectively. The high pyrroles of saddled CoTPPs are resolved in the frequency mapping. All scale bars = 1 nm.

area scan in Figure 5.4e,f (topography is shown in Figure 5.4d). The spatial resolution of the TERS image is impressive. The intensity map clearly shows that the signal is peaked in the intermolecular pockets where phenyl groups converge. The frequency map more clearly displays the internal structure of the molecule. It highlights the saddling distortion of the porphyrin macrocycle with the outline of the diagonal pyrroles that are raised up relative to

the molecular plane. This detail is less clear in the STM image, where saddling is inferred by the oval-shaped center of the molecule. Note, the vibrational frequency shift is due to the Stark effect. The shift is first order in dipolar transitions of odd (u) symmetry, $\Delta\nu = \mu E/\hbar$, and second order in strictly Raman active modes of even (g) symmetry, $\Delta\nu = \alpha E^2/2\hbar$. The observed range of the vibrational shift (10 cm^{-1}) identifies a polar transition, which scatters into the far field through the local field gradients. In these constant bias measurements ($V_S = 9.8 \text{ mV}$), we see the distinction between the polarization of the pyrroles that are in contact with the metal and those that are raised. In effect, through Stark tuning, super-resolved TER-sm maps out polarization, or the local workfunction, within a molecule, as in Kelvin-probe force microscopy with molecule terminated tips[155].

The governing principles of TER-sm are tested through measurements on isolated single molecules that are immobilized at 5 K on the Au(111) substrate. The manipulation sequence summarized in Figure 5.5 is informative. In the scanned area we see three molecules. When the tip is placed on one of the phenyl groups of CoTPP, with scanning mode parameters in current and bias, we only see the electronic Raman continuum of the tip, void of molecular lines (trace 1). Upon pressing on the phenyl ring, by decreasing the junction bias to 2 mV and increasing the junction current to 4 nA, a rather complete vibrational spectrum emerges (trace 2). The spectrum remains stationary as the tip is translated, indicating a molecule snagged by the tip. After measuring the retraction dependent sequence of spectra (traces 3-12), we repeat the same area scan (Fig. 5.5b). The distorted image of the remaining molecules reveals that the missing CoTPP molecule is firmly attached to the tip apex. Upon applying a voltage pulse, the molecule is dropped, and verified to be the intact CoTPP (Figure 5.5c). In this manipulation, the CoTPP TERS spectrum is replaced with the single vibrational line of CO at 2040 cm^{-1} (trace 13). Now the tip is terminated with a CO molecule, which explains its TER-visibility, and the much sharper STM image than in the case of the bare tip topography (compare Figure 5.5a and 5.5c). Several observations are noteworthy about the junction gap dependence of the spectra for the tip-side molecule. The

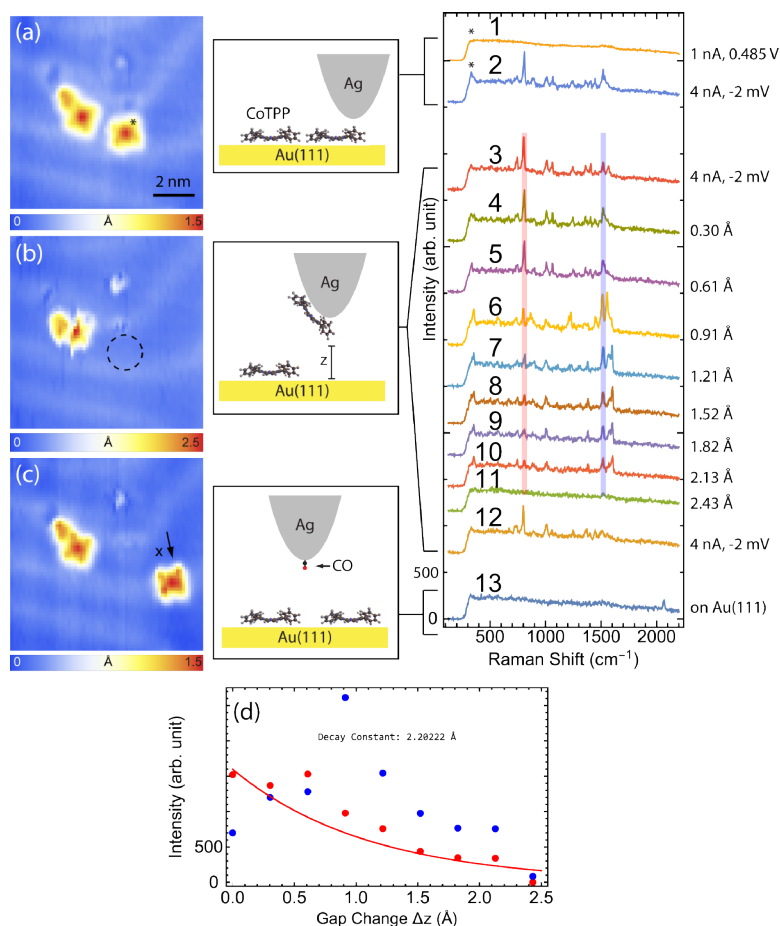


Figure 5.5: TERS by Picking up CoTPP at 5 K. The common set point for topographic images ($104 \times 104 \text{ \AA}^2$) is 0.1 nA and +0.485 V. (a) First image of the transfer sequence. The Ag tip is placed on a phenyl ring of a CoTPP molecule denoted by an asterisk (*). The TER spectrum appears upon approaching the molecule by changing the set point from 1 nA, +0.485 V to 4 nA, -2 mV as demonstrated at the beginning of the spectral sequence denoted by * as well. (b) Image scanned after picking up a CoTPP molecule. The molecule disappears from the position marked by a dashed circle. When the molecule is held at the tip apex, TER spectra are recorded as the tip is retracted incrementally and brought back to tunneling position. (c) Image taken after dropping the CoTPP back to the Au(111) surface by applying a -3 V pulse. The adsorbed porphyrin is accidentally exchanged with a CO molecule during the application of voltage pulse as demonstrated by the C-O stretch peak in the TER spectrum. Accordingly the resolution of image is enhanced due the CO molecular orbital termination. The landing position is displaced from the position where the pulse is applied (denoted by x), which shows the CoTPP was adsorbed slightly off the apex and possibly tilted. (d) Gap dependences of two vibrational peaks at 807 and 1517 cm^{-1} , respectively. The peak intensities are obtained by integrating over shaded windows in the spectral sequence. The exponential fit to the decay of 808 cm^{-1} peak intensity yields 2.2 Å in decay length. This figure was produced by Dr. Joonhee Lee and is used with his permission.

entire spectrum disappears upon 2.4 Å retraction, even though the molecule remains on the apex, as verified by closing the gap again. While the out-of-plane bending mode of the molecular frame at 807 cm⁻¹ mostly decays, the C-C stretching mode at 1517 cm⁻¹ increase in intensity during the first 1 Å retraction, both decay exponentially with a decay constant of ~1 Å. It is not clear whether the mode selective variation in intensity arises from distortions of the molecule or the change in local fields. Assuming a rigid attachment geometry, which would be expected at 5 K, the retraction identifies the variation in the cavity fields felt by the reporter. At these gap distances, the plasmon tunnels across the junction. As the gap is increased, the phototunneling current subsides exponentially to be exchanged by the field of the displacement current. As such, field gradient-activated modes can be expected to give way to field driven Raman lines. This nicely illustrates the Å scale control over the sculpted local fields, and the use of the molecular reporter to understand them.

5.4 Conclusions

The reported measurements were selected to underscore the promise of TER-sm as a chemist's ultimate microscope, with the clear suggestion that beyond imaging the method allows for atomistic manipulations. As a near field effect, TERS does not obey standard selection rules. The scattering can be dominated by gradients of the local field, as such the spectra reflect the molecular polarizability tensor and the vector fields experienced by it. This change in the selection rules help to explain the silence of cold molecules that lie flat on metallic surfaces. They can be activated by lifting, tilting, or poking with the tip, using large tunneling currents near zero-bias. They can also be activated by the introduction of thermal noise through a TERS-invisible 2D gas. This is rationalized by stretching the cavity analogy to perfect resonators, which cannot couple to the far field in the absence of an output coupler or quality spoilers.

The Å-scale spatial resolution, with exponential dependence on junction gap, mimics the

STM and suggests that the optical fields are confined by the tunneling plasmon. This goes against common models of TERS strictly driven by the displacement current. Since the electric field drops by inducing current, charge-transfer plasmons spoil the local field in a cavity, as in a leaky capacitor[156]. While this holds for an empty cavity, the situation is quite different when the target molecule bridges the tunneling junction[157]. Displacement versus tunneling current-induced TERS are analogous to physical versus chemical enhancement mechanisms in SERS[158]. A complete theory must account for both channels in defining the active cavities, which confine photons and electrons.

These results show that TERS can yield vibrational spectra of individual molecules with high S:N and hyperspectral imaging with Å-scale spatial resolution. Beside vibrational intensities, it contains significant information in vibrational shifts that can be extracted through spectral fits. This super-resolution yielded the internal structure of a molecule, which was not apparent in the STM image. Quite clearly, image quality and resolution will be directly related to the signal strength and acquisition speed, and significant improvement over the present can be expected through tip enhanced stimulated Raman spectroscopy, as already demonstrated in a related work[82].

Chapter 6

Imaging Potential Surfaces with 3-Å Resolution via Molecular-Probe Tip-Enhanced Raman Spectroscopy

6.1 Introduction

As discussed in the previous section, TER-sm does not obey standard selection rules due to the necessary local electric fields and field gradients. The resulting spectra can be very complex, containing a wealth of information about these fields as well as the orientation and chemistry of the molecule. Furthermore, while thermal motion at room temperature is sufficient to activate the strong in-plane vibrations of CoTPP that enable TER-sm imaging, these molecules become locked in-plane with the substrate at low temperatures (≤ 80 K), drastically reducing the TERS signal. To compensate for the low signals, the tip-sample gap must be substantially reduced, risking harm to the tip or inadvertently manipulating adsorbed molecules during scanning. While this direct interaction of the tip with the sample, and resultant complex TER-sm spectra, give an unique opportunity to explore nanoscale chemistry, it makes the technique a relatively complex analytical tool.

To simplify the technique while maintaining the Å-scale spatial resolution, TER-sm is used to monitor the stretching frequency of a carbon monoxide (CO) molecule absorbed onto the apex atom of the silver TERS antenna. This system (1) trades the complex and evolving spectra of larger in-plane molecules for the one-mode spectrum of a diatomic molecule (CO) and (2) enables TERS intensity at “safe” tip-sample gap distances since the induced dipole of the main stretch is forced to be aligned with the main axis of the TERS antenna.

CO-functionalized tips have been used in scanning probe microscopies, particularly in atomic force microscopy, to achieve unparalleled spatial resolution and to investigate CO-sample interactions[159–161]. This capability has allowed, for instance, the internal structural changes associated with a molecular reaction to be imaged [162, 163]. In these AFM measurements, shifts in the resonance frequency of the CO-terminated cantilever are used to measure the force felt by the cantilever. Chiang et.al. introduced an STM analog of this AFM technique by measuring the shift of the CO vibration frequency itself, particularly the hindered translational and rotational modes, using inelastic electron tunneling spectroscopy (IETS)[131]. The shifts in the CO frequency can map out the spatial variations in the local potential energy surface of the molecule. In a similar manner, TER-sm can be used to track changes in the much stiffer CO stretch frequency ($\sim 2070 \text{ cm}^{-1}$) as CO is brought to the surface and over other molecules, revealing information about the local potential energy surface with Å-scale resolution. In this new technique, the spatial resolution of CO-terminated STM is coupled with vibrational-resolution of optical spectroscopy.

6.2 Methods

Experiments were carried out at 5 K and 4×10^{-11} Torr using the previously described home-built cryogenic STM. An atomically flat Au(111) surface was prepared by cycles of Ne⁺ sputtering and annealing. Silver tips were prepared by electrochemical etching and ion sputtering (see Chapter 3). CoTPP, ZnEtio (Zinc Etioporphyrin), silver adatoms, and

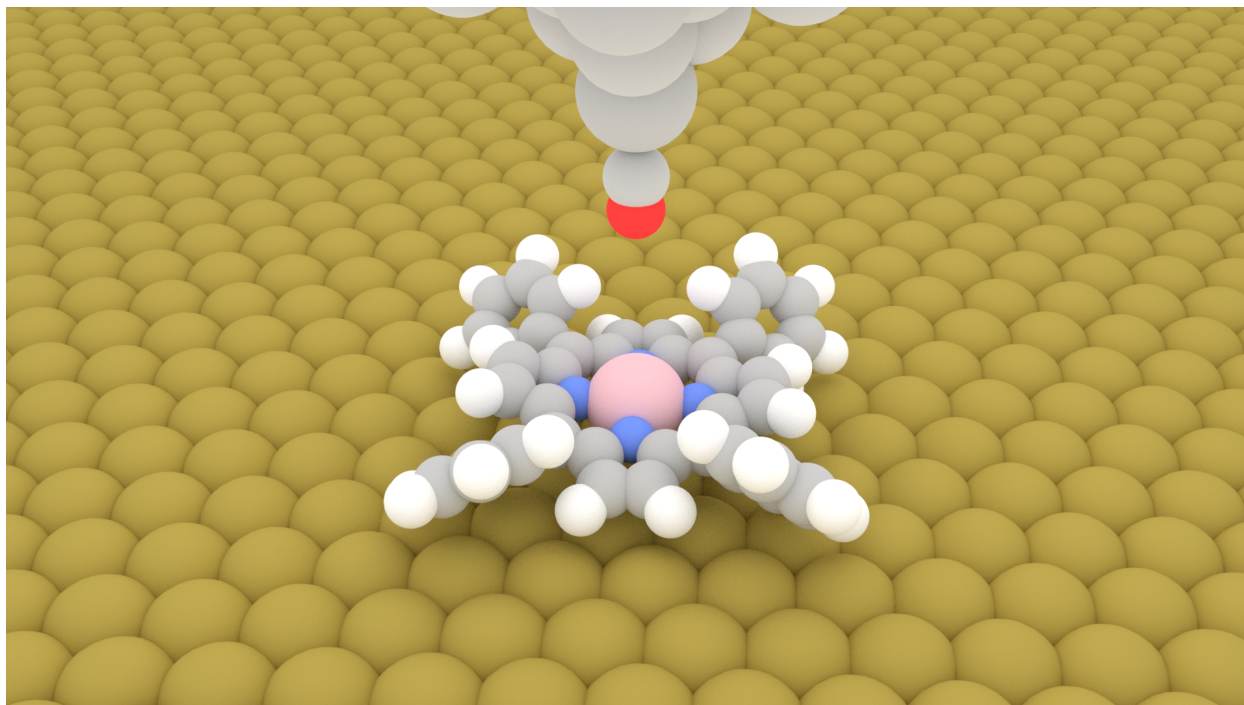


Figure 6.1: Illustration of CO Stark Shift Mapping. The silver STM tip is terminated by a single CO molecule. TERS is then used to record the CO's stretching frequency as the CO-tip is scanned over a CoTPP molecule on Au(111).

$\text{C}^{12}\text{O}^{18}$ were sequentially deposited onto the surface at 5 K (~ 0.25 ML). To produce the necessary CO-terminated silver tip, a CO molecule was transferred to the apex by established techniques[121] or by either scanning at a sample bias < 10 mV and tunneling current > 1 nA or by applying a 100 ms 10 V sample bias pulse. A CO molecule from the 2D lattice gas of mobile surface CO molecules spontaneously adsorbs onto the tip apex, resulting in high-resolution topographic images. An illustration of the setup is shown in Figure 6.1. To acquire the TERS spectrum of CO, 0.5 mW of 634 nm continuous wave diode laser light is introduced to the tip-sample junction at incident angle of 45° and is focused to a ~ 10 μm diameter spot. As described fully in Appendix A, a parabolic mirror collects and collimates light scattered from the junction. The collimated signal is then sent to an imaging spectrometer (Princeton Instruments SpectraPro 2300i, 100 μm slit width, grating = 300 g/mm, 1200 g/mm, or 1800 g/mm) with a liquid cooled CCD (-120 $^\circ\text{C}$, 20×20 μm pixel width). As described previously (see Chapter 3), the tip apex is further modified through voltage pulses to produce the

required enhancing plasmonic cavity.

6.3 TERS spectrum of CO-Tip

Once the necessary preparations have been made to the tip, the Raman spectrum of a single CO molecule can be recorded. The ability to observe such a signal stands as a testament to the field enhancement properties of the new FDSS-processed tips. In some instances, the integrated signal level, R , for a CO absorbed to silver tip can be as high as 2×10^3 counts/sec. Using a math similar to that found in Chapter 2,

$$R = E_F n N \eta d\Omega \frac{\delta\sigma}{\delta\Omega} \quad (6.1)$$

where $n = 1 \times 10^{21}$ photons $\text{cm}^{-2} \text{s}^{-1}$ is the photon (634 nm) flux at an intensity (I) of 6 $\mu\text{W} \mu\text{m}^2$, $N = 1$ is the number of molecules, $\eta = 0.01$ is the collection efficiency from a solid angle $d\Omega = 2.7$ sr, and $\delta\sigma/\delta\Omega = 3.3 \times 10^{-31} \text{ cm}^2 \text{ sr}^{-1}$ is the Raman cross section of CO, the required enhancement factor, E_F , becomes $\sim 10^{14}$. This hundred trillion fold enhancement in the Raman signal, if resulting purely from field enhancement, would imply that the local field is being enhanced by a factor of $g = 3000$. This gives a local field $E_L = 27.45g\sqrt{I} = 0.2$ V/nm.

On top of this large enhancement, the field experienced by the CO is highly confined. The intensity and frequency of the CO stretch mode, obtained from a Gaussian fit, is used to gauge this confinement. The peak's intensity falls exponentially with a decay length of only 3.1 Å as the CO-tip is retracted from the Au(111) surface (Fig. 6.2a). The short decay length suggests that the field may be confined to such spatial scales. The exponential character of the decay and its closeness to the de Broglie wavelength of a Fermi electron ($3.64 \text{ Å} = \lambda = h/mv$, where h is Plank's constant, m is the mass of the electron, and $v = 2 \times 10^6$ m/s) suggests a tunneling process is involved. Since the signal's intensity is directly related to the strength of junction plasmon, the exponential decay of the signal suggests that the plasmon

is tunneling across the junction.

In addition to the insight provided by the intensity, the frequency of the peak is also a useful probe of the nanoscale. During the previously described retraction, the frequency of the CO stretch blue-shifts 3 cm^{-1} with increasing gap distance (Fig. 6.2b). The attractive interaction between the CO and the Au(111) surface loosens the bond slightly. When the CO is pulled away from the surface, this interaction is reduced, leading to the stiffening of the bond.

As was shown with IETS[131, 164], CO probes the local potentials and forces. As CO is retracted from the substrate, the van der Waals force, electrostatic force, and electric field effects all change in magnitude. Given the varying distance dependences for each of these, their contributions to the local potential also vary with gap distance. Complicating matters further, changes in the magnitude of the electric field, from either the applied sample bias or from charges on the surface, can linearly shift the vibration frequency through the Vibrational Stark Effect (VSE). Extracting the exact contributions from each of these origins is an active area of research. Each effect can be independently fit to the observed frequency shift making mechanistic conclusions difficult. CO's nontrivial charge distribution adds an additional layer of complexity[161]. Similar retraction curves starting from positions on CoTPP and ZnEtio were also recorded. The asymptote the frequency approaches varies depending upon the position on the surface. If the interaction went to zero, all of the observed shifts would begin approaching a common "vacuum" value. Theoretical calculations investigating the origin of the high-resolution IETS images concluded that the tip-sample potential energy surface is determined mostly by electrostatic interactions at the "long range" distances probed during such retractions[164]. This long range interaction could also help explain why the asymptote varies with sample bias.

Furthermore, CO's ability to sense local forces is not limited to surface interactions. The shifting of its stretching frequency can give insight into the local electric field of the tip-sample junction through the VSE[165]. Using CO as a local probe, the internal electric

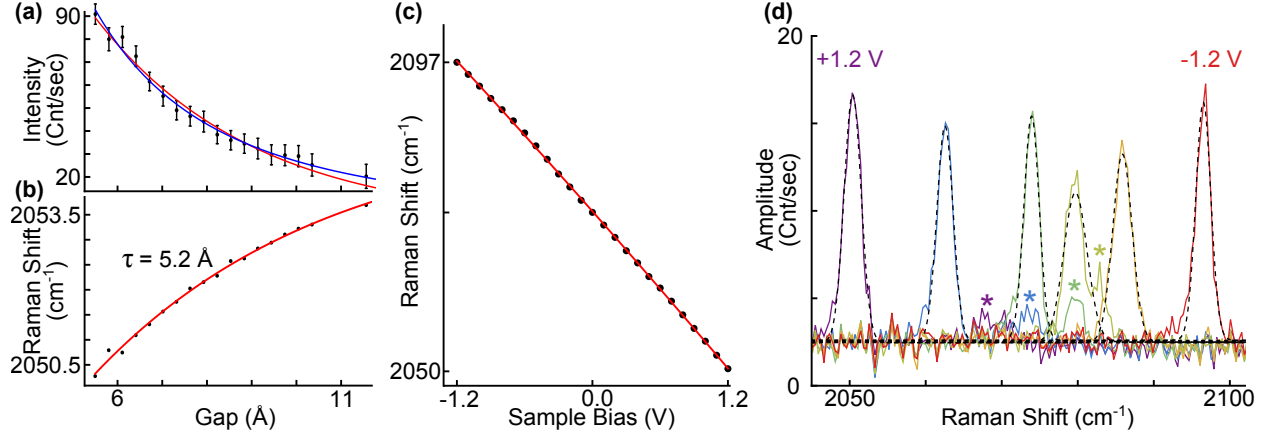


Figure 6.2: Gap and Bias dependence of CO stretch frequency probes the local potential. When the CO-tip is retracted from the bare Au(111) surface, (a) the integrated intensity of the Raman peak falls rapidly. This decay can be fit with an exponential ($\tau = 3.55 \pm 0.14$ Å, red) or a power law ($n = 2.07 \pm 0.06$, blue). (b) The frequency blue-shifts under this same retraction. With the CO-tip fixed at a gap distance (set at $V_S = +1.2$ V, $I_T = 0.1$ nA), the (c) frequency of the mode is recorded as the sample bias is ramped from +1.2 to -1.2 V, giving a linear shift. (d) Selected spectra and their fits are plotted together to highlight this dependence. Several spectra contain an additional, higher frequency peak (marked with asterisks). Each spectrum is the average of six 10 s accumulations taken with an incident 634 nm laser intensity of $5 \mu\text{W} \mu\text{m}^{-2}$. The error bars represent the standard deviation of the intensity and centroid parameters extracted from Gaussian fits.

fields in proteins have been studied[166, 167]. With our CO-tip held fixed above the Au(111) surface (height set at sample bias $V_S = +1.2$ V and setpoint tunneling current $I_T = 0.1$ nA), the VSE can be directly observed by changing the DC electric field in the tunneling gap through the ramping of V_S (Fig. 6.2c and d). Both the Stark tuning rate $\Delta\mu$ and the difference polarizability $\Delta\alpha$ can be extracted from a quadratic fit of the observed frequency shift $\nu(F)$ as a function of applied electric field F [168]

$$\nu(F) = \nu_0 + \Delta\mu F + \frac{1}{2}\Delta\alpha F^2 \quad (6.2)$$

where ν_0 is the vibration frequency at zero applied field. In our measurements, unfortunately, the exact applied DC field is unknown because there is a significant uncertainty in the exact

Location	ν'_0 (cm ⁻¹)	$\Delta\mu'$ (cm ⁻¹ V ⁻¹)	$\Delta\alpha'$ (cm ⁻¹ V ⁻²)
Au(111) surface	2074	-19.27	-0.7270
CoTPP, Co atom	2063	-20.45	-1.469
CoTPP, high pyrrole	2064	-20.13	-2.234
CoTPP, low pyrrole	2059	-20.16	-2.424
ZnEtio, Zn atom*	2079	-18.56	-2.314
ZnEtio, lobe*	2078	-17.46	-0.9620

Table 6.1: Summary of Bias ramps on various structures. *Bias ramp was performed with reformed CO-tip apex, causing a shift in the observed frequencies. They other ramps were done with the same stable CO-tip apex.

gap distance (5.5-7.0 Å). The measured parameters are, instead, a function of V_S :

$$\nu'(V_S) = \nu_0 + \Delta\mu'V_S + \frac{1}{2}\Delta\alpha'V_S^2 \quad (6.3)$$

At any rate, the CO-tip acts as a nanoscale molecular voltmeter. Table 6.1 summarizes the extracted parameters when the CO-tip is placed on a variety of structures on the surface. If the gap is assumed to be 5.5 Å, $\Delta\nu = -106$ cm⁻¹/(V/Å), which agrees well with the ~ 100 cm⁻¹/(V/Å) cited by previous experiments and calculations [168–171]. On the other hand, the observed and theoretical values[168] for $\Delta\alpha$ are wildly different: -11 to -37 cm⁻¹/(V/Å)² verses -0.865 cm⁻¹/(V/Å)², respectively.

Interestingly, an additional Raman peak is present in the bias ramp on Au(111) (Fig. 6.2d). It appears to have a slightly different Stark tuning rate as its position with respect to the main peak changes with sample bias, disappearing into the main peak at large negative biases (< -0.5 V). This second peak may be due to the low-energy bending mode of CO. Similar combinations have been seen in CO vibrational spectra[172] and its position gives insight into the bending potential.

An additional example of more complex spectra can be seen in Figure 6.3. While the clean, sharp topography verifies that the tip is terminated by a single CO molecule, the spectra contain multiple modes. Furthermore, the various mode exhibit a position-dependent shift. The individual modes shift slightly different amounts, suggesting how the low-lying

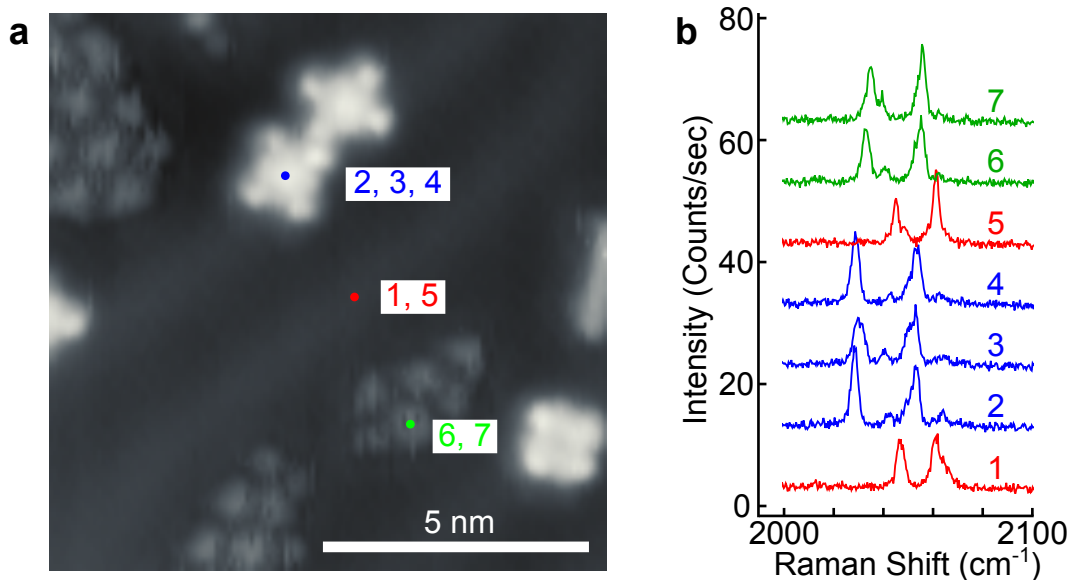


Figure 6.3: Spatially dependent frequency shift. (a) STM topography shows the various types of structures on the surface: the Au(111) surface (red, 1 and 5), CoTPP (blue, 2-4), and CO islands (green, 6 and 7). A ZnEtio molecule is also observed in the lower right. 0.1 nA , $V_s = 1.2 \text{ V}$. (b) The TERS spectra obtained at these various positions each contain 3-4 peaks. The shift of these modes reproducibly depend on where the tip is placed on the surface (constant current mode). The position-dependent shifts are different for each mode.

bending mode is interacting with the environment.

6.4 Imaging Potential Surfaces

As shown in Table 6.1, ν_0 shifts drastically as CO is moved from the surface to a molecule to even within that molecule. This exquisite sensitivity to the local potential is fully realized by tracking ν as CO is scanned over structures on the surface. Figures 6.4 and 6.5 show the variation of three parameters of the CO vibration as CO is scanned over CoTPP and ZnEtio in both constant current (CC) and constant height (CH) mode. The vibration's frequency shift ($\Delta\nu$), intensity, and full width at half maximum (FWHM) vary on sub-molecular length scales, transmitting a wealth of information about the molecule's inner structure. For instance, in Figure 6.4, two of the pyrrole groups (upper left, lower right) shift CO substantially more than the other two pyrroles (lower left, upper right). The topography

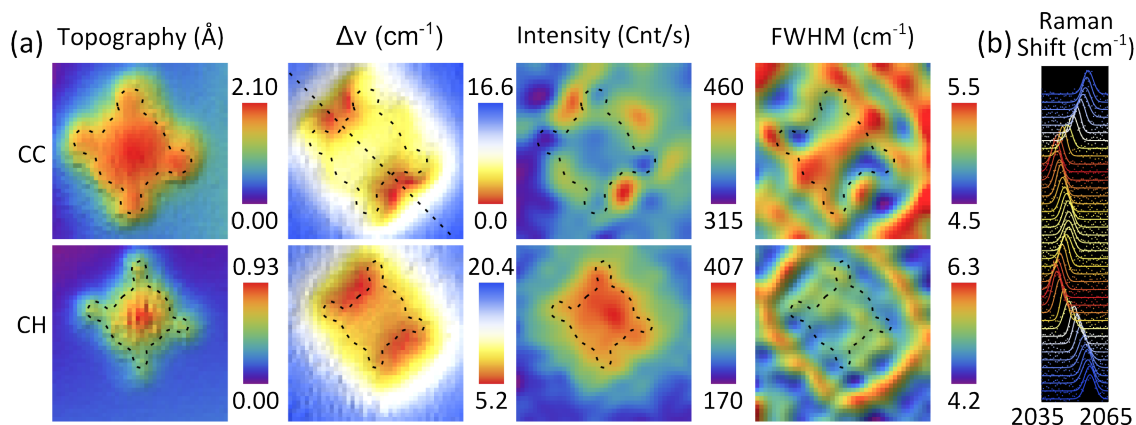


Figure 6.4: CO Stark Shift Mapping of CoTPP. (a) The topography and simultaneously taken CO Raman peak maps of CoTPP taken in constant current (CC, top row) and constant height (CH, bottom row) mode. Gaussian fits of the CO stretch peak are used to create the peak shift from 2040.9 cm⁻¹ ($\Delta\nu$), peak integrated intensity, and peak full width at half maximum (FWHM) maps. An outline of the topography of ZnEtio is shown on each map as a guide. The intensity and FWHM maps have been low-pass filtered for clarity. (b) The fits and raw spectra extracted from the diagonal line cut through the constant height $\Delta\nu$ map shows the extent of the shifting. Images are 22.7×22.7 Å and were at $V_S = +1.21$ V and $I_T = 0.1$ nA for CC mode. Spectra were acquired with a 1 s acquisition, 634 nm excitation, and 5 μW/ μm² average intensity.

shows slightly more density on the lower left and upper right pyrroles, indicating they are pointed slightly away from the sample surface. The opposite pyrroles are pointed slightly towards to surface, placing CoTPP in a saddle-shape conformation[148]. The outer carbon atoms of these low pyrroles may even be bonding, in some way, to the gold surface. At the intermolecular distances of 7 Å (5.5+diameter of O + 0.5 bond length of CO), electrostatic forces should dominate the shift, as such the frequency shift map becomes a map of the electrostatic potential surface. Its variation inside the molecule implies that the molecule is polarized. The molecule is positively charged by electron donation to the electronegative gold. The charge is largest at the anchor points (carbon atoms of the low pyrroles), and gradually changes from the low pyrroles to the high pyrroles. There has been one other such map of the molecular electrostatic potential, using CO-terminated tips and KPFM by Mohn et.al.[155]. Our CO VSE method is significantly more direct, faster and more powerful since signs of the charges are directly measured by the molecular voltmeter. Variations in the

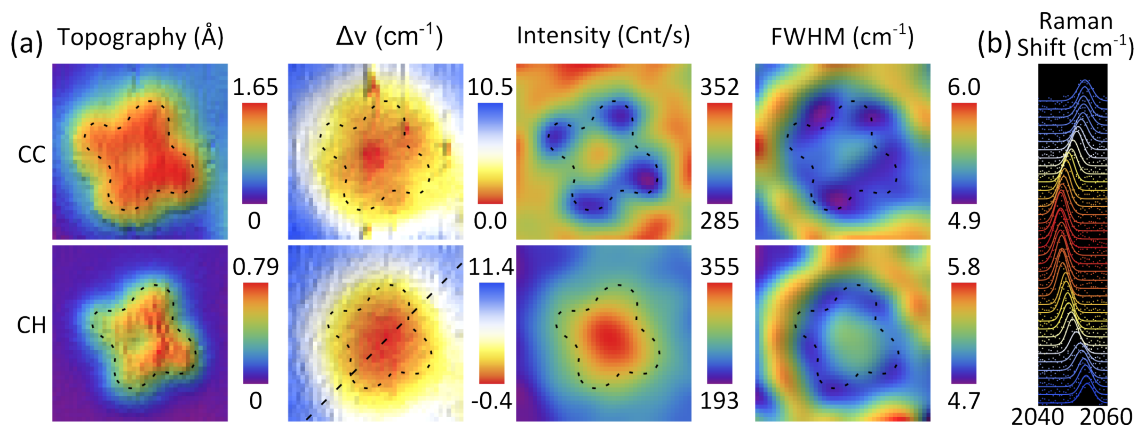


Figure 6.5: CO Stark Shift Mapping of ZnEtio on Au(111). (a) The topography and simultaneously taken CO Raman peak maps of ZnEtio taken in constant current (CC, top row) and constant height (CH, bottom row) mode. Gaussian fits of the CO stretch peak are used to create the peak shift from 2048.1 cm⁻¹ ($\Delta\nu$), peak integrated intensity, and peak full width at half maximum (FWHM) maps. An outline of the topography of ZnEtio is shown on each map as a guide. The intensity and FWHM maps have been low-pass filtered for clarity. (b) The fits and raw spectra extracted from the diagonal line cut through the constant height $\Delta\nu$ map shows the extent of the shifting. Images are 22.7×22.7 Å and were at $V_S = +1.21$ V and $I_T = 0.1$ nA for CC mode. Spectra were acquired with a 1 s acquisition, 634 nm excitation, and $5 \mu\text{W}/\mu\text{m}^2$ average intensity.

local potential are also observed on ZnEtio, though to a lesser extent (Fig. 6.5).

The peak's integrated intensity map also shows intriguing changes. On both molecules in CC mode, the Raman intensity varies, often dropping, across the molecule as the tip traces the constant current shell of the molecule's electron density. In CH mode however, the intensity increases substantially as the CO-tip scans over the molecule, resembling the topography. The increase of Raman intensity with increased tunneling current (decreasing gap distance) again suggests tunneling is involved in sub-nanometer TERS. The increase in the FWHM of the peak around the outside of the molecules is suggestive of imaging lateral potential gradients. Lateral forces could induce scattering on librational states, causing a subtle skewing of the peak lineshape. This skewing could lead to an increase in the fitted linewidth

The peak's integrated intensity map also shows intriguing changes. On both molecules in CC mode, the peak's intensity varies across the molecule as the tip traces the constant

current shell of the molecule’s electron density. In CH mode however, the intensity increases substantially as the CO-tip scans over the molecule, resembling the topography. The increase of Raman intensity with increased tunneling current (decreasing gap distance) again suggests tunneling is involved in sub-nanometer TERS. The increase in the FWHM of the peak around the outside of the molecules indicates that the lifetime of the vibration is shortening, suggesting these regions are dampening the vibration.

This technique demonstrates its versatility by also mapping out a silver adatom (Fig. 6.6). A linecut through this image shows its resolution is similar to that of the STM. The CO stretch frequency red-shifts 25 cm^{-1} as it moves over the silver atom. If this shifting is due solely to the local field or, in this case, voltage, the CO would be measuring a $+\sim 1.3 \text{ V}$ potential on the silver atom. In effect, we are measuring the local workfunction, and we find that it is lowered by 1.3 eV on the silver atom. The drop in workfunction is due to charge transfer from the Ag adatom to the gold, and using the VSE we can extract a partial charge of $+0.38$ on Ag. CO’s protruding cloud of negative charge[161] would be attracted to this charge, supporting this interpretation. This logic would suggest that CoTPP and ZnEtio are also positively charged. Inclusion of other forces in the interaction potential is likely required when interpreting these results.

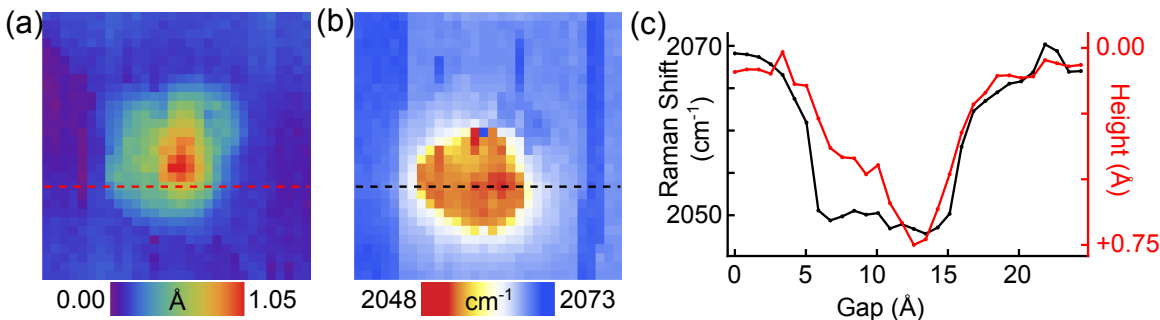


Figure 6.6: CO Stark Shift Map of Ag adatom. (a) The constant current topography of a single silver adatom ($V_S = +0.37 \text{ V}$, $I_T = 1.0 \text{ nA}$) and (b) simultaneously taken CO Stark shift map. (c) A linecut through both images shows that the spatial resolution of Stark shift mapping is on the same order as that of the STM topography. Spectra were acquired with a 1 s acquisition, 634 nm excitation, and $5 \mu\text{W}/\mu\text{m}^2$ average intensity.

6.5 Conclusion

A single CO molecule is used to probe local potentials with 3-Å spatial resolution by exploiting TERS. Not only does this approach break all current records for spatial resolution with optical near-field vibrational spectroscopy but does so without the extremely complex near-field spectra of larger molecules. The single stretch frequency of this diatomic molecule greatly simplifies the observation of the numerous perturbing interactions including van der Waals, electrostatic, electric field and field gradients, charge transfer, and bond formation and breaking. Though only CO-terminated tips are used in this work, tips could be fictionalized with other simple molecules like nitric oxide (NO), cyanide (CN), or copper(II) oxide (CuO). These new tips could directly explore interactions and chemistry with unprecedented sensitivity and resolution, expanding the horizons of this new approach. Furthermore, the measurements would guide our understanding of molecular interactions, improving the assumptions made by the current theories.

Bibliography

- [1] Lee, J.; Perdue, S. M.; Rodriguez Perez, A.; Apkarian, V. A. *ACS Nano* **2014**, *8*, 54–63.
- [2] Tallarida, N.; Rios, L.; Apkarian, V. A.; Lee, J. *Nano Letters* **2015**, *15*, 6386–6394.
- [3] Moore, G. *International Electron Devices Meeting* **1975**, 11–13.
- [4] Aviram, A.; Ratner, M. A. *Chemical Physics Letters* **1974**, *29*, 277.
- [5] Martel, R.; Schmidt, T.; Shea, H. R.; Hertel, T.; Avouris, P. *Applied Physics Letters* **1998**, *73*, 2447.
- [6] Aviram, A.; Joachim, C.; Pomerantz, M. *Chemical Physics Letters* **1988**, *146*, 490–495.
- [7] Donhauser, Z. J.; Mantooth, B. a.; Kelly, K. F.; Bumm, L. a.; Monnell, J. D.; Stapleton, J. J.; Price Jr, D. W.; Rawlett, a. M.; Allara, D. L.; Tour, J. M.; Weiss, P. S. *Science* **2001**, *292*, 2303–7.
- [8] Moresco, F.; Meyer, G.; Rieder, K.-H.; Tang, H.; Gourdon, A.; Joachim, C. *Physical Review Letters* **2001**, *86*, 672–675.
- [9] Huang, T.; Zhao, J.; Feng, M.; Popov, A. a.; Yang, S.; Dunsch, L.; Petek, H. *Nano Letters* **2011**, *11*, 5327–32.
- [10] Schirm, C.; Matt, M.; Pauly, F.; Cuevas, J. C.; Nielaba, P.; Scheer, E. *Nature Nanotechnology* **2013**, *8*, 645–8.
- [11] Kumagai, T.; Hanke, F.; Gawinkowski, S.; Sharp, J.; Kotsis, K.; Waluk, J.; Persson, M.; Grill, L. *Nature Chemistry* **2013**, *6*, 41–46.
- [12] Pop, E. *Nano Research* **2010**, *3*, 147–169.
- [13] Spence, J. *Materials Science and Engineering: R: Reports* **1999**, *26*, 1–49.
- [14] Griessl, S. J. H.; Lackinger, M.; Jamitzky, F.; Markert, T.; Hietschold, M.; Heckl, W. M. *The Journal of Physical Chemistry B* **2004**, *108*, 11556–11560.
- [15] Günther, S.; Dänhardt, S.; Ehrensperger, M. *ACS Nano* **2012**, *7*, 154–164.
- [16] Chen, C. J. *Introduction to Scanning Tunneling Microscopy*; Oxford University Press: New York, 2008; p 423.

- [17] Shank, C. V. *Applied Physics Letters* **1974**, *24*, 373.
- [18] Zewail, A. H. *The Journal of Physical Chemistry A* **2000**, *104*, 5660–5694.
- [19] Petek, H. *ACS Nano* **2014**, *8*, 5–13.
- [20] Wu, S. W.; Ogawa, N.; Ho, W. *Science* **2006**, *312*, 1362–5.
- [21] Berndt, R.; Gaisch, R.; Schneider, W.; Gimzewski, J.; Reihl, B.; Schlittler, R.; Tschudy, M. *Physical Review Letters* **1995**, *74*, 102–105.
- [22] Cocker, T. L.; Jelic, V.; Gupta, M.; Molesky, S. J.; Burgess, J. A. J.; Reyes, G. D. L.; Titova, L. V.; Tsui, Y. Y.; Freeman, M. R.; Hegmann, F. A. *Nature Photonics* **2013**, *7*, 620–625.
- [23] Jahng, J.; Fishman, D. A.; Park, S.; Nowak, D. B.; Morrison, W. A.; Wickramasinghe, H. K.; Potma, E. O. *Accounts of Chemical Research* **2015**, *48*, 2671–2679.
- [24] Jahng, J.; Brocious, J.; Fishman, D. A.; Yampolsky, S.; Nowak, D.; Huang, F.; Apkarian, V. A.; Wickramasinghe, H. K.; Potma, E. O. *Applied Physics Letters* **2015**, *106*.
- [25] Kravtsov, V.; Ulbricht, R.; Atkin, J. M.; Raschke, M. B. *Nature Nanotechnology* **2016**, *11*, 1–7.
- [26] Yampolsky, S.; Fishman, D. A.; Dey, S.; Hulkko, E.; Banik, M.; Potma, E. O.; Apkarian, V. A. *Nature Photonics* **2014**, *8*, 650–656.
- [27] Dazzi, A.; Prater, C. B. *Chemical Reviews* **2016**, *117*, 5146–5173.
- [28] Sonntag, M. D.; Klingsporn, J. M.; Zrimsek, A. B.; Sharma, B.; Ruvuna, L. K.; Van Duyne, R. P. *Chemical Society Reviews* **2014**, *43*, 1230–47.
- [29] Schlücker, S. *Angewandte Chemie - International Edition* **2014**, *53*, 4756–4795.
- [30] Pozzi, E. A.; Goubert, G.; Chiang, N.; Jiang, N.; Chapman, C. T.; McAnally, M. O.; Henry, A.-I.; Seideman, T.; Schatz, G. C.; Hersam, M. C.; Duyne, R. P. V. *Chemical Reviews* **2017**, *117*, 4961–4982.
- [31] Sonntag, M. D.; Klingsporn, J. M.; Garibay, L. K.; Roberts, J. M.; Dieringer, J. A.; Seideman, T.; Scheidt, K. a.; Jensen, L.; Schatz, G. C.; Van Duyne, R. P. *Journal of Physical Chemistry C* **2012**, *116*, 478–483.
- [32] Steidtner, J.; Pettinger, B. *Physical Review Letters* **2008**, *100*, 236101.
- [33] Zhang, R.; Zhang, Y.; Dong, Z. C.; Jiang, S.; Zhang, C.; Chen, L. G.; Zhang, L.; Liao, Y.; Aizpurua, J.; Luo, Y.; Yang, J. L.; Hou, J. G. *Nature* **2013**, *498*, 82–86.
- [34] Liao, M.; Jiang, S.; Hu, C.; Zhang, R.; Kuang, Y.; Zhu, J.; Zhang, Y.; Dong, Z. *Nano Letters* **2016**, *16*, 4040–4046.

- [35] Trautmann, S.; Aizpurua, J.; Götz, I.; Undisz, A.; Dellith, J.; Schneidewind, H.; Rettenmayr, M.; Deckert, V. *Nanoscale* **2017**, *9*, 391–401.
- [36] Liu, P.; Chulhai, D. V.; Jensen, L. *ACS Nano* **2017**, *11*, 5094–5102.
- [37] Chen, X.; Moore, J. E.; Zekarias, M.; Jensen, L. *Nature Communications* **2015**, *6*, 8921.
- [38] Lee, J.; Tallarida, N.; Rios, L.; Perdue, S. M.; Apkarian, V. A. *ACS Nano* **2014**, *8*, 6382–6389.
- [39] Gardiner, C. *Handbook of Stochastic Methods for Physics, Chemistry and the Natural Sciences*; Springer: Berlin, 1997.
- [40] Lee, J.; Perdue, S. M.; Perez, A. R.; El-Khoury, P. Z.; Honkala, K.; Apkarian, V. A. *The Journal of Physical Chemistry. A* **2013**, *117*, 11655–64.
- [41] Chen, F.; Hihath, J.; Huang, Z.; Li, X.; Tao, N. *Annual Review of Physical Chemistry* **2007**, *58*, 535–564.
- [42] Gouterman, M. *The Journal of Chemical Physics* **1972**, *56*, 4073.
- [43] McConnell, H. M. *The Journal of Chemical Physics* **1961**, *34*, 13.
- [44] Penfold, T.; Worth, G. *Chemical Physics* **2010**, *375*, 58–66.
- [45] Le Ru, E. C.; Etchegoin, P. G. *Annual Review of Physical Chemistry* **2012**, *63*, 65–87.
- [46] Kleinman, S. L.; Ringe, E.; Valley, N.; Wustholz, K. L.; Phillips, E.; Scheidt, K. A.; Schatz, G. C.; Van Duyne, R. P. *Journal of the American Chemical Society* **2011**, *133*, 4115–4122.
- [47] Blackie, E.; Le Ru, E. C.; Meyer, M.; Timmer, M.; Burkett, B.; Northcote, P.; Etchegoin, P. G. *Physical chemistry chemical physics : PCCP* **2008**, *10*, 4147–4153.
- [48] Moerner, W. E.; Fromm, D. P. *Review of Scientific Instruments* **2003**, *74*, 3597–3619.
- [49] Kneipp, K.; Wang, Y.; Kneipp, H.; Perelman, L. T.; Itzkan, I.; Dasari, R. R.; Feld, M. S. *Physical Review Letters* **1997**, *78*, 1667–1670.
- [50] Ootani, Y.; Satoh, K.; Nakayama, A.; Noro, T.; Taketsugu, T. *The Journal of Chemical Physics* **2009**, *131*, 194306.
- [51] Pederzoli, M.; Pittner, J.; Barbatti, M.; Lischka, H. *Journal of Physical Chemistry A* **2011**, *115*, 11136–11143.
- [52] Cantatore, V.; Granucci, G.; Persico, M. *Computational and Theoretical Chemistry* **2014**, *1040-1041*, 126–135.
- [53] Zimmerman, G.; Paik, U.-J.; Chow, L.-Y. *Journal of the American Chemical Society* **1958**, *80*, 3528–3531.

- [54] Hartley, G. S. *Journal of the Chemical Society* **1938**, 633–642.
- [55] Turansky, R.; Konopka, M.; Doltsinis, N. L.; Stich, I.; Marx, D. *Physical Chemistry Chemical Physics* **2010**, *12*, 13922.
- [56] Henzl, J.; Mehlhorn, M.; Gawronski, H.; Rieder, K. H.; Morgenstern, K. *Angewandte Chemie - International Edition* **2006**, *45*, 603–606.
- [57] Choi, B. Y.; Kahng, S. J.; Kim, S.; Kim, H. W. H.; Kim, H. W. H.; Song, Y. J.; Ihm, J.; Kuk, Y. *Physical Review Letters* **2006**, *96*, 1–4.
- [58] Duarte, L.; Fausto, R.; Reva, I. *Physical Chemistry Chemical Physics* **2014**, *16*, 16919.
- [59] Mahimwalla, Z.; Yager, K. G.; Mamiya, J. I.; Shishido, A.; Priimagi, A.; Barrett, C. J. *Polymer Bulletin* **2012**, *69*, 967–1006.
- [60] Tegeder, P. *Journal of Physics: Condensed Matter* **2012**, *24*, 394001.
- [61] Bandara, H. M. D.; Burdette, S. C. *Chemical Society Reviews* **2012**, *41*, 1809.
- [62] Plain, J.; Wiederrecht, G. P.; Gray, S. K.; Royer, P.; Bachelot, R. *The Journal of Physical Chemistry Letters* **2013**, *4*, 2124–2132.
- [63] Harabuchi, Y.; Ishii, M.; Nakayama, A.; Noro, T.; Taketsugu, T. *The Journal of Chemical Physics* **2013**, *138*, 064305.
- [64] Fujino, T.; Arzhantsev, S. Y.; Tahara, T. *The Journal of Physical Chemistry A* **2001**, *105*, 8123–8129.
- [65] Hoffman, D. P.; Ellis, S. R.; Mathies, R. A. *The Journal of Physical Chemistry A* **2013**, *117*, 11472–11478.
- [66] Quick, M.; Dobryakov, A. L.; Gerecke, M.; Richter, C.; Berndt, F.; Ioffe, I. N.; Granovsky, A. A.; Mahrwald, R.; Ernsting, N. P.; Kovalenko, S. A. *The Journal of Physical Chemistry B* **2014**, *118*, 8756–8771.
- [67] Dobryakov, A. L.; Quick, M.; Ioffe, I. N.; Granovsky, A. A.; Ernsting, N. P.; Kovalenko, S. A. *The Journal of Chemical Physics* **2014**, *140*, 184310.
- [68] Dokić, J.; Gothe, M.; Wirth, J.; Peters, M. V.; Schwarz, J.; Hecht, S.; Saalfrank, P. *The Journal of Physical Chemistry A* **2009**, *113*, 6763–6773.
- [69] Alemani, M.; Peters, M. V.; Hecht, S.; Rieder, K. H.; Moresco, F.; Grill, L. *Journal of the American Chemical Society* **2006**, *128*, 14446–14447.
- [70] Alemani, M.; Selvanathan, S.; Ample, F.; Peters, M. V.; Rieder, K. H.; Moresco, F.; Joachim, C.; Hecht, S.; Grill, L. *Journal of Physical Chemistry C* **2008**, *112*, 10509–10514.

- [71] Comstock, M. J.; Levy, N.; Kirakosian, A.; Cho, J.; Lauterwasser, F.; Harvey, J. H.; Strubbe, D. A.; Fréchet, J. M. J.; Trauner, D.; Louie, S. G.; Crommie, M. F. *Physical Review Letters* **2007**, *99*, 1–4.
- [72] Hagen, S.; Leyssner, F.; Nandi, D.; Wolf, M.; Tegeder, P. *Chemical Physics Letters* **2007**, *444*, 85–90.
- [73] Tegeder, P.; Hagen, S.; Leyssner, F.; Peters, M. V.; Hecht, S.; Klamroth, T.; Saalfrank, P.; Wolf, M. *Applied Physics A: Materials Science and Processing* **2007**, *88*, 465–472.
- [74] Wolf, M.; Tegeder, P. *Surface Science* **2009**, *603*, 1506–1517.
- [75] Floß, G.; Granucci, G.; Saalfrank, P. *Journal of Chemical Physics* **2012**, *137*.
- [76] Benassi, E.; Granucci, G.; Persico, M.; Corni, S. *The Journal of Physical Chemistry C* **2015**, *119*, 150224154037009.
- [77] Stuart, C. M.; Frontiera, R. R.; Mathies, R. A. *Journal of Physical Chemistry A* **2007**, *111*, 12072–12080.
- [78] Joshi, G. K.; Blodgett, K. N.; Muhoberac, B. B.; Johnson, M. A.; Smith, K. A.; Sardar, R. *Nano Letters* **2014**, *14*, 532–540.
- [79] Zheng, Y. B.; Payton, J. L.; Chung, C.-H. H.; Liu, R.; Cheunkar, S.; Pathem, B. K.; Yang, Y.; Jensen, L.; Weiss, P. S. *Nano Letters* **2011**, *11*, 3447–3452.
- [80] Mannsfeld, S. C. B.; Canzler, T. W.; Fritz, T.; Proehl, H.; Leo, K.; Stumpf, S.; Goretzki, G.; Gloe, K. *The Journal of Physical Chemistry B* **2002**, *106*, 2255–2260.
- [81] Picardi, G.; Chaigneau, M.; Ossikovski, R.; Licitra, C.; Delapierre, G. *Journal of Raman Spectroscopy* **2009**, *40*, 1407–1412.
- [82] Wickramasinghe, H. K.; Chaigneau, M.; Yasukuni, R.; Picardi, G.; Ossikovski, R. *ACS Nano* **2014**, *8*, 3421–3426.
- [83] Sasaki, S. S.; Perdue, S. M.; Perez, A. R.; Tallarida, N.; Majors, J. H.; Apkarian, V. A.; Lee, J. *Review of Scientific Instruments* **2013**, *84*, 096109.
- [84] Poirier, G. E.; Pylant, E. D. *Science* **1996**, *272*, 1145–1148.
- [85] Barth, J. V.; Brune, H.; Ertl, G.; Behm, R. J. *Physical Review B* **1990**, *42*, 9307–9318.
- [86] Kirakosian, A.; Comstock, M. J.; Cho, J.; Crommie, M. F. *Physical Review B - Condensed Matter and Materials Physics* **2005**, *71*, 1–4.
- [87] Maksymovych, P.; Sorescu, D. C.; Yates, J. T. *Physical Review Letters* **2006**, *97*, 1–4.
- [88] Cho, J.; Levy, N.; Kirakosian, A.; Comstock, M. J.; Lauterwasser, F.; Fréchet, J. M. J.; Crommie, M. F. *Journal of Chemical Physics* **2009**, *131*.

- [89] Comstock, M. J.; Levy, N.; Cho, J.; Berbil-Bautista, L.; Crommie, M. F.; Poulsen, D. a.; Fréchet, J. M. J.; Fréchet, J. M. J.; Fréchet, J. M. J. *Applied Physics Letters* **2008**, *92*, 24–27.
- [90] Banik, M.; El-Khoury, P. Z.; Nag, A.; Rodriguez-Perez, A.; Guarrotxena, N.; Bazan, G. C.; Apkarian, V. A. *ACS nano* **2012**, *6*, 10343–54.
- [91] Sonntag, M. D.; Chulhai, D.; Seideman, T.; Jensen, L.; Van Duyne, R. P. *Journal of the American Chemical Society* **2013**, *135*, 17187–17192.
- [92] Mirjani, F.; Thijssen, J. M.; Ratner, M. a. *The Journal of Physical Chemistry C* **2012**, *116*, 23120–23129.
- [93] Klingsporn, J. M.; Jiang, N.; Pozzi, E. A.; Sonntag, M. D.; Chulhai, D.; Seideman, T.; Jensen, L.; Hersam, M. C.; Van Duyne, R. P. *Journal of the American Chemical Society* **2014**, *136*, 3881–3887.
- [94] Noda, I.; Ozaki, Y. *Two-Dimensional Correlation Spectroscopy: Applications in Vibrational and Optical Spectroscopy*; John Wiley & Sons Ltd: Chichester, West Sussex, England, 2004.
- [95] Taylor, J. R. *An Introduction to Error Analysis: The Study of Uncertainties in Physical Measurements*, 2nd ed.; University Science Books: Sausalito, California, USA, 1997; pp 209–220.
- [96] McNellis, E. R.; Meyer, J.; Reuter, K. *Physical Review B - Condensed Matter and Materials Physics* **2009**, *80*, 1–10.
- [97] Shao, Y. et al. *Phys. Chem. Chem. Phys.* **2006**, *8*, 3172–3191.
- [98] Kevan, S. D.; Gaylord, R. H. *Physical Review B* **1987**, *36*, 5809–5818.
- [99] Li, J.; Schneider, W.; Berndt, R.; Bryant, O. *Physical review letters* **1998**, *81*, 4464–4467.
- [100] Hulbert, S. L.; Johnson, P. D.; Stoffel, N. G.; Smith, N. V. *Physical Review B* **1985**, *32*, 3451–3455.
- [101] Zaitsev, N. L.; Nechaev, I. A.; Echenique, P. M.; Chulkov, E. V. *Physical Review B - Condensed Matter and Materials Physics* **2012**, *85*, 1–8.
- [102] Bro, R.; Smilde, A. K. *Analytical Methods* **2014**, *6*, 2812.
- [103] Van Schrojenstein Lantman, E. M.; De Peinder, P.; Mank, A. J. G.; Weckhuysen, B. M. *ChemPhysChem* **2015**, *16*, 547–554.
- [104] Wood, B. R.; Bailo, E.; Khiavi, M. A.; Tilley, L.; Deed, S.; Deckert-Gaudig, T.; McNaughton, D.; Deckert, V. *Nano Letters* **2011**, *11*, 1868–1873.

- [105] Hagen, S.; Kate, P.; Leyssner, F.; Nandi, D.; Wolf, M.; Tegeder, P. *Journal of Chemical Physics* **2008**, *129*.
- [106] Riyad, Y. M.; Naumov, S.; Griebel, J.; Elsner, C.; Hermann, R.; Siefertmann, K. R.; Abel, B. *American Journal of Nano Research and Application* **2014**, *2*, 39–52.
- [107] Sasaki, S. S.; Zhang, Y.-n.; Dey, S.; Tallarida, N.; El-Khoury, P. Z.; Apkarian, V. A.; Wu, R. *The Journal of Physical Chemistry C* **2014**, *118*, 29287–29293.
- [108] Opilik, L.; Dogan, Ü.; Szczerbiński, J.; Zenobi, R. *Applied Physics Letters* **2015**, *107*, 091109.
- [109] Jeanmaire, D. L.; Van Duyne, R. P. *Journal of Electroanalytical Chemistry* **1977**, *84*, 1–20.
- [110] Majors, J. H. Nonlocal Plasmonic Field Emission of Electrons from Focusing by Sharp Probe Tips. PhD dissertation, University of California, Irvine, 2015.
- [111] Schmucker, S.; Kumar, N.; Abelson, J.; Daly, S.; Girolami, G.; Bischof, M.; Jaeger, D.; Reidy, R.; Gorman, B.; Alexander, J.; Ballard, J.; Randall, J.; Lyding, J. *Nature Communications* **2012**, *3*, 935.
- [112] Schiller, C.; Koomans, A. A.; van Rooy, T. L.; Sch?nenberger, C.; Elswijk, H. B. *Surface Science* **1995**, *339*, L925–L930.
- [113] Jackson, J. D. *Classical Electrodynamics*, 3rd ed.; John Wiley & Sons, Inc.: New York, NY, 1999.
- [114] Ferrari, A. C.; Robertson, J. *Philosophical Transactions of the Royal Society A* **2004**, *362*, 2477–2512.
- [115] Mills, D. L. *Physical Review B* **2002**, *65*, 125419.
- [116] Wu, S.; Mills, D. L. *Physical Review B* **2002**, *65*, 205420.
- [117] Chen, C.; Chu, P.; Bobisch, C. A.; Mills, D. L.; Ho, W. *Physical Review Letters* **2010**, *105*, 2–5.
- [118] Pettinger, B.; Domke, K. F.; Zhang, D.; Schuster, R.; Ertl, G. *Physical Review B - Condensed Matter and Materials Physics* **2007**, *76*, 1–4.
- [119] Rendell, R.; Scalapino, D.; Mühlischlegel, B. *Physical Review Letters* **1978**, *41*, 1746–1750.
- [120] Banik, M.; Rodriguez, K.; Hulkko, E.; Apkarian, V. A. *ACS Photonics* **2016**, *3*, 2482–2489.
- [121] Bartels, L.; Meyer, G.; Rieder, K.-H.; Velic, D.; Knoesel, E.; Hotzel, A.; Wolf, M.; Ertl, G. *Physical Review Letters* **1998**, *80*, 2004–2007.

- [122] Etchegoin, P. G.; Le Ru, E. C. *Physical chemistry chemical physics : PCCP* **2008**, *10*, 6079–6089.
- [123] Steidtner, J.; Pettinger, B. *Review of Scientific Instruments* **2007**, *78*, 103104.
- [124] Barbry, M.; Koval, P.; Marchesin, F.; Esteban, R.; Borisov, A. G.; Aizpurua, J.; Sánchez-Portal, D. *Nano Letters* **2015**, *15*, 3410–3419.
- [125] Benz, F.; Schmidt, M. K.; Dreismann, A.; Chikkaraddy, R.; Zhang, Y.; Demetriadou, A.; Carnegie, C.; Ohadi, H.; de Nijs, B.; Esteban, R.; Aizpurua, J.; Baumberg, J. J. *Science* **2016**, *354*, 726–729.
- [126] Hulteen, J. C.; Young, M. A.; Van Duyne, R. P. *Langmuir* **2006**, *22*, 10354–10364.
- [127] Yang, W.; Hulteen, J.; Schatz, G. C.; Van Duyne, R. P. *The Journal of Chemical Physics* **1996**, *104*, 4313–4323.
- [128] Kleinman, S. L.; Sharma, B.; Blaber, M. G.; Henry, A.-I.; Valley, N.; Freeman, R. G.; Natan, M. J.; Schatz, G. C.; Van Duyne, R. P. **2013**,
- [129] Frontiera, R. R.; Mathies, R. A. *Laser and Photonics Reviews* **2011**, *5*, 102–113.
- [130] Crampton, K. T.; Zeytunyan, A.; Fast, A. S.; Ladani, F. T.; Alfonso-Garcia, A.; Banik, M.; Yampolsky, S.; Fishman, D. A.; Potma, E. O.; Apkarian, V. A. *Journal of Physical Chemistry C* **2016**, *120*, 20943–20953.
- [131] Chiang, C.-l.; Xu, C.; Han, Z.; Ho, W. *Science* **2014**, *344*, 885–888.
- [132] El-Khoury, P. Z.; Honkala, K.; Hess, W. P. *Journal of Physical Chemistry A* **2014**, *118*, 8115–8123.
- [133] Chiang, N.; Jiang, N.; Chulhai, D. V.; Pozzi, E. A.; Hersam, M. C.; Jensen, L.; Seideman, T.; Van Duyne, R. P. *Nano Letters* **2015**, *15*, 4114–4120.
- [134] Jaynes, E.; Cummings, F. *Proceedings of the IEEE* **1963**, *51*, 89–109.
- [135] Novotny, L.; van Hulst, N. *Nature Photonics* **2011**, *5*, 83–90.
- [136] Alù, A.; Engheta, N. *Physical Review B - Condensed Matter and Materials Physics* **2008**, *78*, 1–6.
- [137] Nie, S.; Emory, S. R. *Science* **1997**, *275*, 1102–1106.
- [138] Kneipp, K.; Moskovits, M.; Kneipp, H. *Surface Enhanced Raman Scattering: Physics and Applications*; Springer Berlin Heidelberg, 2006.
- [139] Zhang, P.; Feist, J.; Rubio, A.; García-González, P.; García-Vidal, F. J. *Physical Review B - Condensed Matter and Materials Physics* **2014**, *90*, 1–5.
- [140] Pettinger, B.; Schambach, P.; Villagómez, C. J.; Scott, N. *Annual Review of Physical Chemistry* **2012**, *63*, 379–399.

- [141] Zrimsek, A. B.; Chiang, N.; Mattei, M.; Zaleski, S.; McAnally, M. O.; Chapman, C. T.; Henry, A.-I.; Schatz, G. C.; Van Duyne, R. P. *Chemical Reviews* **2017**, *117*, 7583–7613.
- [142] Jiang, N.; Kurouski, D.; Pozzi, E. A.; Chiang, N.; Hersam, M. C.; Van Duyne, R. P. *Chemical Physics Letters* **2016**, *659*, 16–24.
- [143] Chu, P.; Mills, D. L. *Physical Review B - Condensed Matter and Materials Physics* **2011**, *84*, 1–8.
- [144] Song, P.; Nordlander, P.; Gao, S. *Journal of Chemical Physics* **2011**, *134*.
- [145] Savage, K. J.; Hawkeye, M. M.; Esteban, R.; Borisov, A. G.; Aizpurua, J.; Baumberg, J. J. *Nature* **2012**, *491*, 574–577.
- [146] Giesecking, R. L.; Ratner, M. A.; Schatz, G. C. *ACS Symposium Series* **2016**, *1245*, 1–22.
- [147] Roelli, P.; Galland, C.; Piro, N.; Kippenberg, T. J. *Nature Nanotechnology* **2015**, *11*, 164–169.
- [148] Seufert, K.; Bocquet, M.-L.; Auwärter, W.; Weber-Bargioni, A.; Reichert, J.; Lorente, N.; Barth, J. V. *Nature Chemistry* **2011**, *3*, 114–9.
- [149] Domke, K. F.; Pettinger, B. *ChemPhysChem* **2009**, *10*, 1794–1798.
- [150] Stockman, M. I. *Physical Review Letters* **2004**, *93*, 137404.
- [151] Babadjanyan, A. J.; Margaryan, N. L.; Nerkararyan, K. V. *Journal of Applied Physics* **2000**, *87*, 3785–3788.
- [152] Aydin, M.; Akins, D. L. *Applications of Molecular Spectroscopy to Current Research in the Chemical and Biological Sciences*; InTech, 2016.
- [153] Chulhai, D. V.; Jensen, L. *The Journal of Physical Chemistry C* **2013**, *117*, 130911133503005.
- [154] Huang, B.; Bates, M.; Zhuang, X. *Annual Review of Biochemistry* **2009**, *78*, 993–1016.
- [155] Mohn, F.; Gross, L.; Moll, N.; Meyer, G. *Nature Nanotechnology* **2012**, *7*, 227–231.
- [156] Marinica, C.; Kazansky, A. K.; Nordlander, P.; Aizpurua, J.; Borisov, A. G. *Nano Letters* **2012**, *1*, 1–10.
- [157] El-Khoury, P. Z.; Hu, D.; Apkarian, V. A.; Hess, W. P. *Nano letters* **2013**, *13*, 1858–61.
- [158] Giesecking, R.; Ratner, M. A.; Schatz, G. C. *Faraday Discuss.* **2017**,
- [159] Gross, L.; Mohn, F.; Moll, N.; Liljeroth, P.; Meyer, G. *Science* **2009**, *325*, 1110–4.
- [160] Gross, L.; Mohn, F.; Moll, N.; Schuler, B.; Criado, A.; Guitian, E.; Pena, D.; Gourdon, A.; Meyer, G. *Science* **2012**, *337*, 1326–1329.

- [161] Ellner, M.; Pavliček, N.; Pou, P.; Schuler, B.; Moll, N.; Meyer, G.; Gross, L.; Pérez, R. *Nano Letters* **2016**, *16*, 1974–1980.
- [162] de Oteyza, D. G.; Gorman, P.; Chen, Y.-C.; Wickenburg, S.; Riss, A.; Mowbray, D. J.; Etkin, G.; Pedramrazi, Z.; Tsai, H.-Z.; Rubio, A.; Crommie, M. F.; Fischer, F. R. *Science* **2013**, *340*, 1434–1437.
- [163] Riss, A.; Paz, A. P.; Wickenburg, S.; Tsai, H.-Z.; De Oteyza, D. G.; Bradley, A. J.; Ugeda, M. M.; Gorman, P.; Jung, H. S.; Crommie, M. F.; Rubio, A.; Fischer, F. R. *Nature Chemistry* **2016**, *8*, 678–683.
- [164] Hapala, P.; Temirov, R.; Tautz, F. S.; Jelinek, P. *Physical Review Letters* **2014**, *113*, 226101.
- [165] Hush, N. S.; Reimers, J. R. *The Journal of Physical Chemistry* **1995**, *99*, 15798–15805.
- [166] Suydam, I. T.; Boxer, S. G. *Biochemistry* **2003**, *42*, 12050–12055.
- [167] Lehle, H.; Kriegel, J. M.; Nienhaus, K.; Deng, P.; Fengler, S.; Nienhaus, G. U. *Biophysical journal* **2005**, *88*, 1978–90.
- [168] Brewer, S. H.; Franzen, S. *The Journal of Chemical Physics* **2003**, *119*, 851–858.
- [169] Lambert, D. K. *Electrochimica Acta* **1996**, *41*, 623–630.
- [170] Lambert, D. K. *Physical Review Letters* **1983**, *50*, 2106–2109.
- [171] He, H. Y.; Pi, S. T.; Bai, Z. Q.; Banik, M.; Apkarian, V. A.; Wu, R. Q. *Journal of Physical Chemistry C* **2016**, *120*, 20914–20921.
- [172] Ewing, G. E.; Pimentel, G. C. *The Journal of Chemical Physics* **1961**, *35*, 925–930.
- [173] Brown, K. A.; Ho, W. *Review of Scientific Instruments* **1995**, *66*, 5371.

Appendix A

System Improvements

The following sections describe the various ways experiments and the equipment used in these experiments have been developed and improved. Improvements are continuously being made and further progress is expected over the course of my graduate career.

A.1 Parabolic Mirror Alignment

The homebuilt UHV cryogenic STM used for the various experiments is unique due to its inclusion of a piezo-controlled parabolic mirror. This mirror encircles the tip-sample junction and is used for the focusing and/or collection of light. The focus of this parabolic

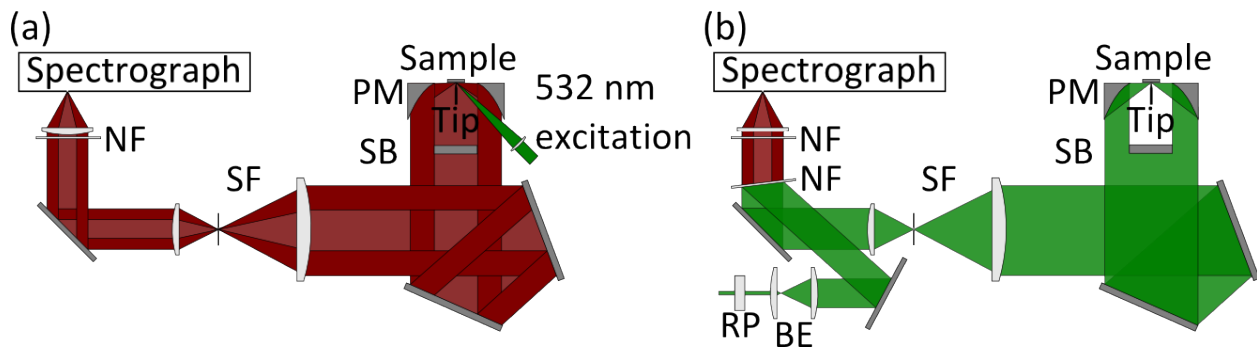


Figure A.1: Excitation geometries with the excitation laser shown in green and the Raman signal in red. (a) Excitation at 45° . (b) Excitation via the Parabolic Mirror. NF = 532 nm notch filter, SF = spatial filter with $100\ \mu\text{m}$ pinhole, SB = scanner base, PM = parabolic mirror, RP = radial polarizer, BE = beam expander.

mirror is positioned exactly at the junction of the STM, where the metallic tip meets the conductive sample, allowing light scattered from this region to be collected, collimated, and directed out of the main vacuum chamber. This scheme benefits from a relatively high collection efficiency, when compared to a standard 1" lens, and diffraction-limited, chromatic aberration-free focusing of light. This makes a parabolic mirror ideal for the focusing and collection of ultrafast laser pulses which undergo dispersion when passing through refractive optics. However, correctly aligning the parabolic mirror onto the STM tip apex is a complex process. To better understand the excitation and collection geometry, the optical setup (Fig. A.1) was simulated using Zemax OpticStudio™ 14.2.

A.1.1 Ray Tracing Simulation

The model of the collection line (Figures A.2 and A.3) contains the essential elements of the experimental detection line. Light, represented by blue ray lines, is emitted or is scattered from a sphere or spherical cone. Using the non-sequential ray tracing, rays either reflect off of the $\varnothing 1.384$ " parabolic mirror or are absorbed by the three-legged base of the scanner. The rays reflected off of the parabolic mirror are sent past the base of the scanner. The shadow cast by the base of the scanner produces the three-lobed image seen in Figures A.4 and A.5. After the scanner base, the rays travel ~ 1.8 m before entering a spatial filter (SF) consisting of a $\varnothing 2$ " achromatic doublet lens ($f = 75$ mm, Thorlabs AC508-075-A), a $100 \mu\text{m}$ pinhole, and a $\varnothing 1$ " achromatic double lens ($f = 30$ mm, Thorlabs AC254-030-A), giving a total magnification power of 0.4. The $\varnothing 0.55$ " image travels ~ 0.27 m before being focused onto a detector with a $\varnothing 1$ " achromatic doublet lens ($f = 100$ mm, Thorlabs AC254-100-A). The models of the parabolic mirror and the scanner base were created in Autodesk®Inventor®and imported into Zemax. The lenses were taken from ThorLabs' Zemax library.

	Object Type	Comment	Ref Object	Inside Of	X Position	Y Position	Z Position	Tilt About X	Tilt About Y	Tilt About Z	Material
1	Source Ray	5.08 is the focus	0	0	0.000	0.000	60.000	0.000	0.000	0.000	-
2	Cone		0	0	0.000	0.000	0.000	0.000	0.000	0.000	
3	Cylinder Volume	SAMPLE	0	0	0.000	0.000	-1.000E-003	0.000	0.000	0.000	
4	CAD Part: Autodesk Inventor®	ParabolicMirror2_mm.ipt	0	0	0.000	0.000	-5.080	270.000	-30.000	0.000	
5	CAD Part: Autodesk Inventor®	scanner_base_mm.ipt	0	0	0.000	0.000	40.000	270.000	0.000	0.000	
6	Detector Rectangle	after base	0	0	0.000	0.000	65.000	0.000	0.000	0.000	
7	Detector Rectangle	before spatial filter	0	0	0.000	0.000	1780.000	0.000	0.000	0.000	
8	Standard Lens	surfaces 2-3	0	0	0.000	0.000	1800.000	0.000	0.000	0.000	E-BAF11
9	Standard Lens	surfaces 3-4	8	0	0.000	0.000	20.000	0.000	0.000	0.000	N-SF11
10	Cylinder Pipe	pinhole, at 64mm	9	0	0.000	0.000	64.000 V	0.000	0.000	0.000	
11	Standard Lens	surfaces 5-6	9	0	0.000	0.000	99.500	180.000	0.000	0.000	N-BAF10
12	Standard Lens	surfaces 6-7	11	0	0.000	0.000	12.000	0.000	0.000	0.000	N-SF6HT
13	Standard Lens	surfaces 8-9	8	0	0.000	0.000	370.000	0.000	0.000	0.000	N-BK7
14	Standard Lens	surfaces 9-10	13	0	0.000	0.000	4.000	0.000	0.000	0.000	SF5
15	Detector Rectangle	after spatial filter	10	0	0.000	0.000	40.000	0.000	0.000	0.000	
16	Detector Rectangle	before final lens	14	0	0.000	0.000	-10.000	0.000	0.000	0.000	
17	Detector Rectangle	ccd	14	0	0.000	0.000	100.000	0.000	0.000	0.000	

Figure A.2: The component editor in Zemax OpticStudio 14.2 for the parabolic detection line.

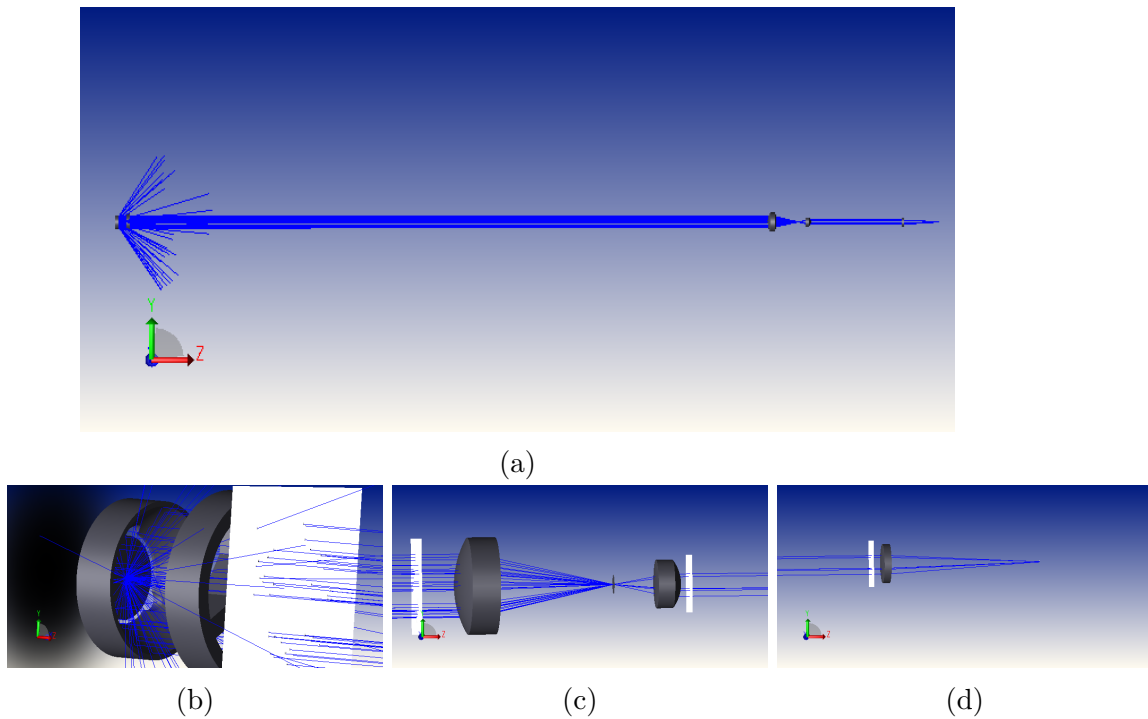


Figure A.3: Model of parabolic detection line. (a) View of the full model. (b) Scanner body, angle view. Point or volume ellipse source is placed at the focus of the parabolic mirror. (c) Spatial Filter and pinhole. (d) Final focusing lens. The white squares are detectors and blue lines represent calculated rays.

A.1.2 Impact of the source

Spherical Source

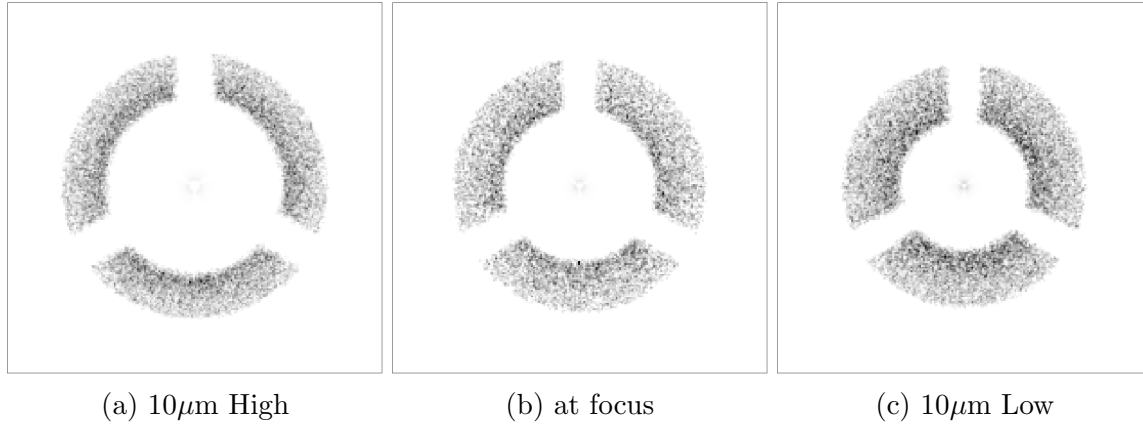


Figure A.4: The position of a spherical source (radius = $5\ \mu\text{m}$) on the detected image 1.78 m away. Moving the source higher brings the source closer to the sample. Moving the source lower brings the source down the shaft of the tip.

The size and shape of the image provides information about where the scattering source is with respect to the focus of the parabolic mirror. For instance, when the scattering source is positioned above (below) the focus of the parabolic mirror, the scattered image diverges (converges) (See Fig. A.4). The collapsing of the image suggests scattering from the tip shaft while the expanding of the image suggests scattering from the sample. In reality, we often can see mixing of these images, suggesting that both the tip shaft and sample are participating in the scattering.

As the radius, r , of the spherical source is increased (see Fig A.5), the lobes in the image grow and become blurry while the cutoff between lobes become more radial. This change in the angle of the edge of lobes is also seen in Fig A.4c.

Parabolic Excitation Geometry

Focusing onto the junction with the parabolic mirror rather than with a 1" lens at 45° normal to the sample surface allows excitation with a much shallower incidence angles (4 to 30°). Analysis of this geometry revealed that the resulting image now included both scattering

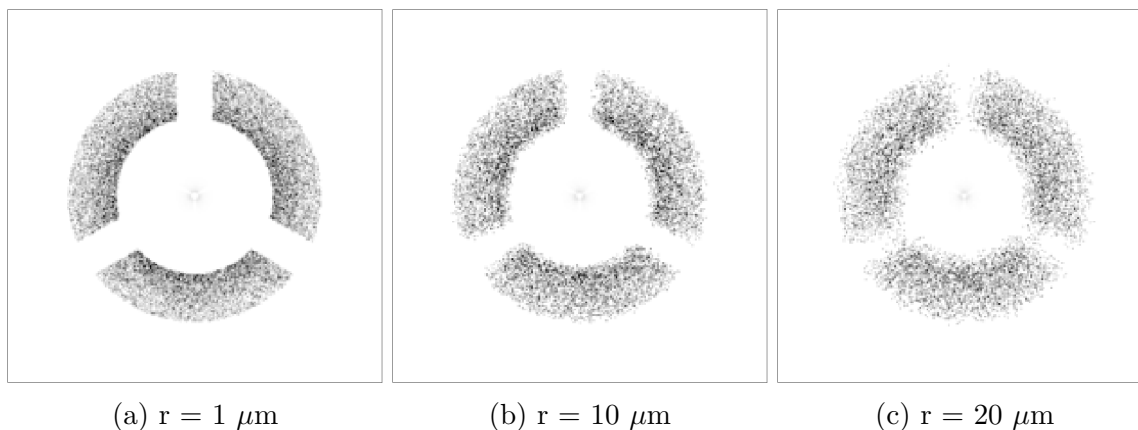


Figure A.5: The detected image 1.78 m away with various source sizes at the focus.

from the tip (modeled by a sphere) and reflections from the sample. The scattering from the tip gives the well-understood 3-lobed image (Fig. A.4) while reflection from the sample gives a 6-lobed image. The 6 lobes result from the beam passing by the base of the scanner twice, casting two shadows (Fig A.6). This 6-lobed image is readily observed in the experiment both before and after the spatial filter. However, after the signal passes through the notch filter, only the scattered 3-lobed image remains. This suggests that the sample itself produces no Raman shifted photons and that the observed broad Raman background is from the tip, as initially thought.

This alignment is very sensitive to errors in the beam propagation angle. If the excitation beam angle is too large, resulting from either poor collimation or alignment errors, the beam will not hit the tip apex. Instead, it will only reflect off of the sample, producing only the 6-lobed image.

A.1.3 Parabolic Alignment Tool

Aligning the parabolic mirror to the tip apex is critical for optimizing the collection of SM-TERS photons. However, the alignment process can at times be difficult and confusing. The parabolic alignment tool (Fig A.7) was created in Wolfram Mathematica®10.2 to help guide us in positioning the parabolic mirror. It simulates the electro-luminescence (EL)

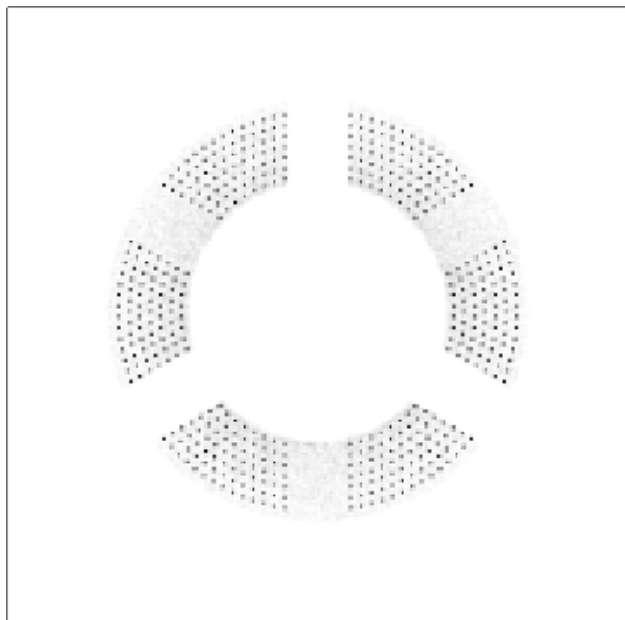


Figure A.6: Detected image before the spatial filter using parabolic excitation. The 6-lobe structure, consisting of highly ordered rays, is from reflections off of the sample. The diffuse 3-lobe background is from lambertian scattering off of the sphere, $r = 1 \mu\text{m}$.

image on the ccd plane. The tool includes 3 axis controls, allowing the user to simulate how the EL image will change when the mirror is translated in any given direction. When a mirror position is requested, the tool imports a previously save PNG image displaying a density plot of the simulated CCD image. These simulations, in turn, were produced using a slight variation of the previously described Zemax OpticStudioTM 14.2 model of the parabolic mirror detection line. Since the spatial filter is not used during parabolic mirror alignment, the spatial filter is omitted from the ray-tracing simulation.

A.2 Load-Lock System

Given the importance of the STM tip in TERS experiments and the uncertainty in how the tip geometry contributes to the TERS signal, it is critical to be able to continually test new tip geometries as our understanding of the TERS process improves. Furthermore, the properties of the molecule itself, such as its Raman scattering cross-section, dipole alignment, and coupling to the surface, are critical to obtaining spatially resolved TERS. The original design

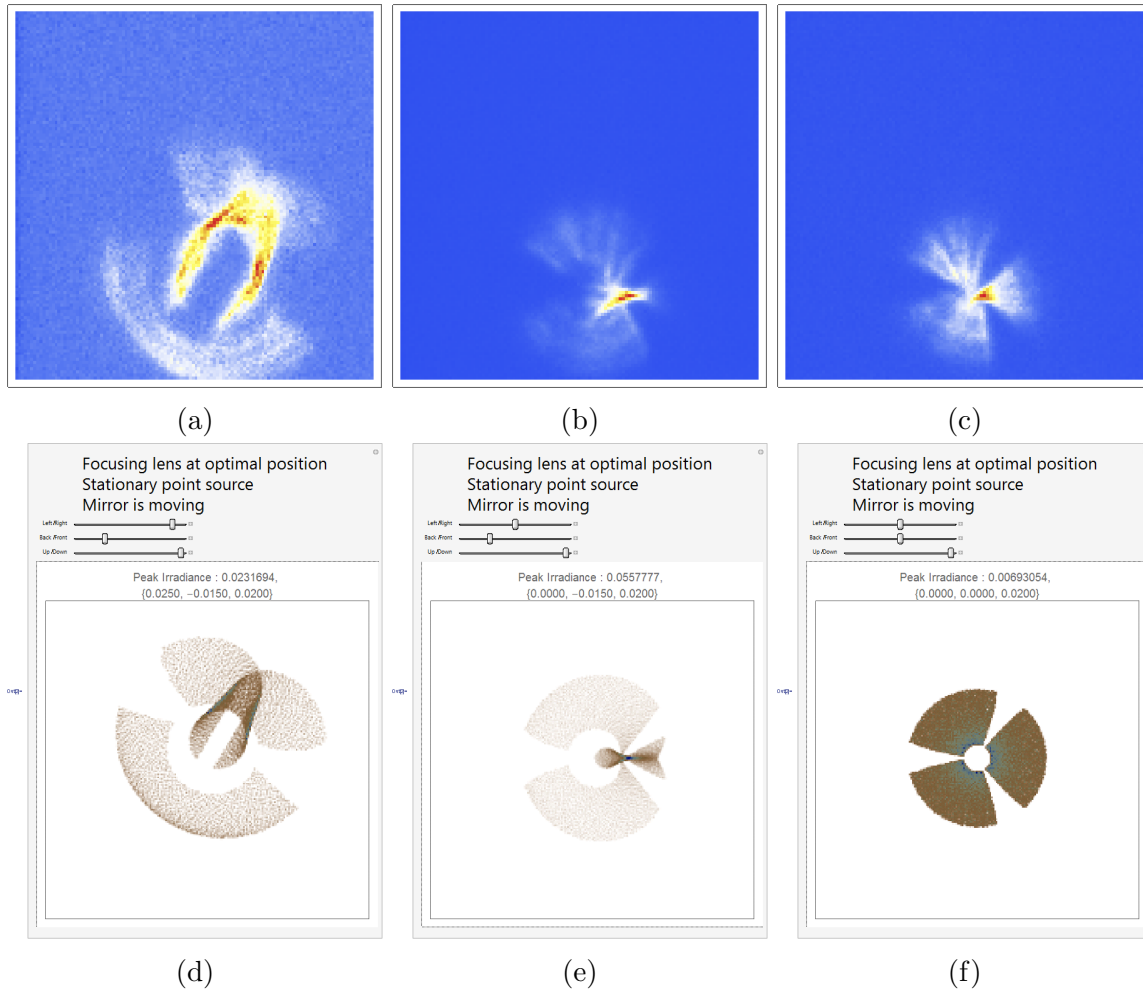


Figure A.7: Parabolic Alignment Tool aids in positioning the parabolic mirror. The experimentally observed images, (a)-(c), are recreated using the 3-axis control of the tool, (d)-(f).

of the home-built cryogenic UHV-STM allowed for the storage of 7 samples, 40 STM tips, and 2 molecular dosers. However, adding new tips to the chamber or a new molecule to the doser originally required bringing the chamber from 5×10^{-11} torr to atmosphere, resulting in long instrument down-times as well as unwanted stress to the chamber itself, especially to its various delicate filaments. In an effort to improve the flexibility and capabilities of our STM, a load-lock system has been added that enables the changing of tips, samples, and molecules with relative ease and minimal impact to the chamber.

In the original design, unused tips and samples were stored on a rotating carousel affixed to the inside face of a 6" CF flange via a mounting rod and screws. The new load-lock

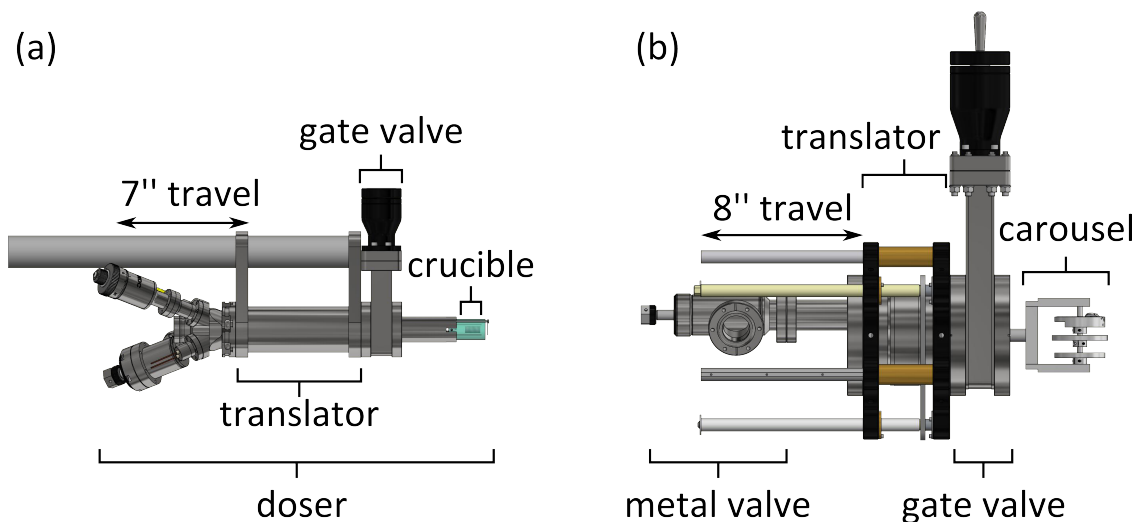


Figure A.8: Schematic of the tip/sample and doser loadlocks. (a) The molecular doser is placed on 2.75" manual single-axis translator with 7" of travel, attached to the chamber via a 2.75" gate valve. (b) A 6" gate valve and a 6" bellows-sealed linear translator with 8" of travel is placed between the chamber and the carousel's base flange. The rod connecting the carousel to the base flange is lengthened to compensate for the additional width of the compressed translator and gate valve.

worked off of this design by inserting a 6" gate valve and a 6" bellows-sealed linear translator (McAllistor BLT63) between the main chamber and the original 6" CF flange. The original flange is modified with a protruding 2.75" CF flange, allowing for the attachment of a 2.75" All-Metal angle valve and the mounting rod is lengthened to compensate for the additional length of the gate valve and compressed translator. To exchange samples and tips, the load-lock translator is fully extended to retract the carousel from the main chamber. The gate valve is then closed to isolate the carousel from the main chamber, allowing this isolated section to be brought up to ambient pressure by leaking dry nitrogen gas through the All-Metal angle valve. The carousel flange, with the stocked carousel, can then be removed from the chamber and its sample/tip supply restocked. The carousel flange can then be reattached and pumped out by the external pumping system (explained later). The pumping, baking, and degassing of the load-lock and external pumping system required to reach 9×10^{-10} torr takes approximately 5 days. Once the pressure reaches the desired level, the load-lock gate valve can be opened, followed quickly by the closing of the load-lock All-Metal angle valve.

The base pressure of the main chamber does rise to $\sim 1 \times 10^{-10}$ but can be lowered over time with the help of the main chamber's titanium sublimation pump (TSP) and ion pump.

To enable the quick exchange of molecules that can be dosed or evaporated onto our sample, a retractable and removable molecular doser (evaporator) is required. Due to the length of the fully compressed linear translator and gate valve, the doser originally would no longer extend fully into the main chamber. Although there exist commercially available retractable dosers (Kentax TCE-BS), all of its heating crucibles were slightly displaced from the flange's central axis. Due to the small opening in the scanner's shield for the passing of the molecular beam, an on-axis evaporator is required. Furthermore, a homebuilt doser would allow us to completely control its design and maintenance.

The design of the homebuilt doser was kept simple. A rotary feedthrough (for shutter control), a low-power feedthrough (for supplying the heating current), a k-type thermocouple feedthrough, a blank mini-flange, and an All-Metal Angle Valve were installed onto a 2.75" Flange Multiplexer (Kimball Physics MCF275-FlgMplxr-Cr1A5). Tungsten wire ($\varnothing 0.02$ ") is wrapped along the threads of an alumina crucible, which was previously cut and threaded with the help of members of the Wilson Ho Lab at UC Irvine following established procedures[173]. The wrapped crucible is suspended via the tungsten wire between two 2" long 0-80 tantalum threaded rods, which, in turn, were connected to alumina-insulated copper wires that lead to the low-power feedthrough. When current (< 4 Amps) is applied to this continuous connection, the tungsten wire heats the alumina crucible holding the ~ 50 mg of the molecule to be dosed. The tantalum/alumina assembly is supported by a small aluminum base, which, in turn, is supported by two 14" long 6-32 thread stainless steel rods that are screwed into an adapter plate on the bottom blank mini-flange. The crucible and its immediate support structure is enclosed within a custom built cylindrical tantalum shield (OD = 0.5") with a small 0.25" molecular beam exit hole. The rotary feedthrough rotates a long 2-56 threaded rod attached to a tantalum shutter. The k-type thermocouple is placed in contact with a small recess on the bottom of the crucible. The internal body of the doser

in enclosed within a stainless steel tube (OD = 0.625", ID = 0.505") to ensure the body's straightness. Exchanging the molecular doser is accomplished using the same protocol as the sample/tip exchange by using its own smaller gate valve and All-Metal valve.

A.2.1 Pumping Station and Tip Preparation

An external pumping system capable of attaining UHV is needed in order to use the load-lock. As discussed above, this pumping system must be able to reach at least 9×10^{-10} torr and must be portable. To reach this pressure, the station (Fig. A.9) is equipped with a scroll backing pump, a turbomolecular pump, a ion pump, and a titanium sublimation pump (TSP). To ensure the system is portable, the whole system is supported by an aluminum t-slotted frame terminated by a set of casters. Any remaining controllers are held in a separate 19" portable rack.

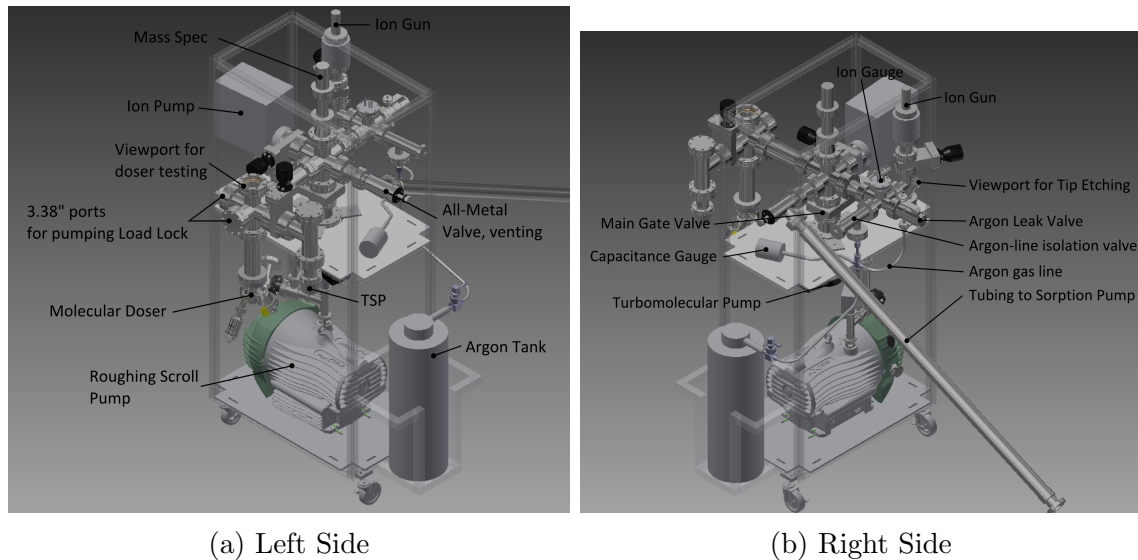


Figure A.9: The multipurpose Pumping Station is used for the testing of molecular dosing conditions or for pumping out the main chamber's load lock (a) as well as for the field-directed ion sharpening of metallic tips (b). The important components for these tasks are labeled.

The chamber is brought to UHV using standard vacuum techniques. To prepare the system for pumping, the main gate valve is closed. The scroll pump then pumps out the

section containing the turbo pump to < 50 mTorr. The turbo pump can then be safely started in preparation for opening the gate valve. However, before the gate valve can be opened, the chamber is first pumped down to 5 mTorr with a liquid nitrogen sorption pump through the chamber's All-Metal valve. Once 5 mTorr is reached, the All-Metal valve is closed and the main gate valve is quickly opened. The chamber pressure will soon drop to below 10^{-5} Torr, allowing for the use of the ion gauge. To reach 9×10^{-10} Torr, the chamber is wrapped with a combination of flexible silicone rubber heat tapes (BriskHeat BS0) affixed with heat-resistant tape and heat sheets (McMaster-Carr), all of which is covered with aluminum foil.